Polarization of Resonantly Scattered Lines in Active Galactic Nuclei

Thesis by

Hee-Won Lee

In Partial Fulfillment of the Requirements

for the Degree of

Doctor of Philosophy

California Institute of Technology

Pasadena, California

1995

(Submitted June 2, 1995)

To my parents

Acknowledgements

First, I would like to thank my parents for their love and continuing support. I think I have been under an invisible but tangible influence for pursuing the study of natural sciences from them. I also want to express my gratitude to my brother and sister. My brother, who now has a Ph.D. in mathematics, has always been around to provide whatever help he could give. We shared and enjoyed everything from discussing the most sophisticated theories of mathematics to trivial everyday experiences.

My life at Caltech would have been rather dull and boring without having so many Korean friends around like Yanglim. Unfortunately, they are too numerous to name individually. They helped to soothe my homesickness. Best of luck to them in their future pursuits, whatever they may be!

I would like to thank the people of TAPIR. They were always kind enough to provide assistance in every way. Even though it was not a long experience, they got me to find out how interesting a game volleyball is, and I hope our team will flourish in my absence.

It's probably conventional to leave the 'special' person to the end. Such a person is surely my advisor, Roger Blandford. I cannot express my full gratitude toward him with my poor English and I hope he understands, as he always does. I came to realize that it is not mere knowledge that makes a man a good scientist, and he demonstrated this point to me in ways that I will never forget. Hopefully, I will keep his lessons to heart.

Thanks to everyone whom I have forgotten to mention above, but have helped me out in my time at Caltech.

Abstract

Most Active Galactic Nuclei are characterized by prominent UV emission lines in their spectra, and the line photons are believed to be resonantly scattered many times before emerging along the line of sight. The polarization of these line photons, which is sensitive to the atomic physics, can be an important tool for investigating the scattering geometry and kinematics of the line-emitting region. The principle of resonance scatterings are discussed in order to elucidate the relation between the emergent polarization, the atomic transitions and the anisotropy of the radiation field. When the ratio of collision frequency to radiative excitation rate is much larger than 1, collisional mixing occurs and the ground state sublevels are equally populated. The opposite case is radiative mixing, where the anisotropic radiation field may induce uneven population in the ground state sublevels, leading to enhancement of polarization. A density matrix is introduced to deal with the photon polarization state and the level population of the ions.

A density matrix formalism based Monte Carlo approach is adopted and used to compute the polarization of emission lines emerging from anisotropic clouds or anisotropically expanding clouds. The effect of both spatial diffusion and geometric anisotropy on polarization is considered. It is shown that semi-forbidden C III] λ1909, which has a moderate optical depth ranging $1 - 10$ in the broad emission line region, can be polarized, whereas most permitted UV lines having large scattering optical depth are negligibly polarized.

The same code is modified to incorporate the Sobolev approximation and polarization of the broad absorption line troughs in broad absorption line quasars. Both bipolar flow and equatorial flow are examined. Up to 15 percent polarization in the absorption trough is obtained in the doublet transition J=1/2 $\rightarrow$ 1/2, 3/2 for an equatorial flow model, and from a bipolar flow model, a lower degree of polarization is obtained. A higher polarization is obtained for the singlet transition case J=0 $\rightarrow$ 1, which should be a good diagnostic to test whether the polarization is

caused by resonance scattering. Recent spectropolarimetry is briefly summarized, and observational ramifications are discussed.

Finally the conditions necessary to produce significant polarization from outflowing gas from quasars are studied. Multiplet transitions with radiative mixing are considered and compared to the polarization from a singlet transitions which produce the highest polarization. The steep rise in the polarized flux shortward of ~ 800Å observed in a radio quiet quasar PG 1630+377 is interpreted in terms of resonance line scattering.

Table of Contents

1

Introduction

Active galactic nuclei (AGNs) is a general term for describing extragalactic objects showing nonstellar (and nonthermal) continuum. Most of them also exhibit prominent UV emission lines in their spectra. The typical members of AGN include quasars and Seyfert galaxies. However, there are many other objects showing similar phenomena with different luminosity scales or in different spectral ranges. There has been a lot of work toward a unified model of AGNs, in which spectropolarimetry plays an important role. Polarization studies may be summarized as the investigation of anisotropy in the geometry or kinematics of a system. Therefore polarization measurements are regarded as important checks for testing the applicability of a model to a given system. This work is mainly devoted to the development of a formalism to compute the polarization of resonantly scattered line photons and its applications to the emission and absorption lines of AGN.

In the introduction, basic concepts concerning the AGN polarization are discussed. In Chapter 2, the basic atomic physics necessary for computing the polarization of resonantly scattered line photons, is discussed. This serves as the basis for the Monte Carlo computation of the polarization of the emergent photons from a system of anisotropic clouds, which constitutes the subject of the following chapter. In Chapter 4, the same numerical code is applied to quasar emission lines, and the Sobolev approximation is combined with this Monte Carlo approach to obtain the polarization of absorption line troughs of broad absorption line quasars by adopting simple kinematic models. The implication of this study on the unification of radio quiet quasars is discussed. Finally in Chapter 5, we interpret the steep rise of polarization blueward of Lyman limit observed in PG 1630+377 by a combination of resonantly scattered singlet lines including O V and N IV.

1.1 OBSERVATIONAL CLASSIFICATION OF AGN

As mentioned above, the term 'active galactic nuclei' generally applies to extragalactic objects which show nonstellar continuum in their spectra. AGNs include Seyfert galaxies, quasars, radio galaxies, low ionization nuclear emission region (LINER) galaxies, optically violent variables (OVVs) and BL Lac objects. They are classified into subclasses according to more detailed spectral properties. (*cf.* Netzer 1990)

Seyfert galaxies are the earliest observed AGNs (*cf.* Seyfert 1943) They are classified into two types according to the existence of broad emission lines in their spectra (*cf.* Khachikian & Weedman 1971, Osterbrock 1989). Seyfert 1 galaxies have broad permitted lines with full width at half maximum (FWHM) $\sim 5,000$km s^{-1} and narrow forbidden lines with FWHM $\sim$ 500km s^{-1}, whereas both the permitted and the forbidden emission lines of Seyfert 2 galaxies are narrow. Osterbrock (1989) suggested further classification of Seyfert galaxies into intermediate types such as 1.5, 1.8, 1.9 according to their H I profiles. Morphologically, Seyfert galaxies are spiral and constitute only a fraction of 1 per cent of all spiral galaxies. Seyfert galaxies are usually radio-quiet.

Radio galaxies, as the name suggests, emit a significant fraction of their total continuum energy in the radio band from two diametrically opposite lobes. Morphologically, they are elliptical and the similarity of their optical spectra to Seyfert galaxies allows classification into two types analogous to Seyfert galaxies. The radio galaxies with broad permitted lines and narrow forbidden lines are called broad line radio galaxies (BLRGs) and those showing only narrow permitted and forbidden lines are classified as narrow line radio galaxies (NLRGs).

Quasars are divided into two classes by their radio emission properties, *i. e.* , radio-loud and radio quiet quasars. The radio-loud quasars, comprising about 10 per cent of all known quasars, are further subdivided to core-dominated and lobe-dominated quasars. The radio emission for core-dominated quasars is dominated

by the component from the compact core which shows a flat spectrum whereas the lobe-dominated quasars have most of their radio emission from the two opposing lobes with steep spectrum. The radio quiet quasars exhibit more luminosity but similar optical spectra to those of Seyfert 1 galaxies. There is no known quasar which does not have broad lines analogous to Seyfert 2 galaxies. However, about 10 per cent of radio quiet quasars show broad absorption troughs in their highly ionized broad line components. These are called broad absorption line quasars (BALQs).

Optically violent variables and BL Lac objects form a subgroup of AGNs showing rapid variability and they are collectively called Blazars (Angel & Stockman 1980). For BL Lac objects, the continuum is featureless and shows high polarization. Sometimes starburst galaxies and ultraluminous IR galaxies can be included in the family of AGNs.

The spectral similarities between quasars, Seyfert galaxies and radio galaxies imply that they may not be intrinsically different objects but similar objects viewed in different directions. This observation led to a unification scheme of AGNs that classifies various objects by the aspect effect or luminosity difference (Lawrence 1987, Blandford 1990). Invoking the standard paradigm of a supermassive black hole with the accretion disk as the central engine of AGN, we may incorporate various phenomena regarding AGN into the unification scheme.

Spectropolarimetry of Seyfert 2 galaxy NGC 1068 by Antonucci & Miller (1985) showed that Seyfert 2 galaxies may have hidden Seyfert 1 type nuclei (See also Miller & Goodrich 1990). They showed that the polarized spectra of NGC 1068 show broad Balmer lines and Fe lines which are characteristic of Seyfert 1 galaxies. They also interpreted the polarized broad line component as a component scattered by hot electrons located above the central continuum source, where the continuum is blocked by a thick molecular torus.

Special relativistic Doppler boosting can provide a natural explanation of lack of emission lines of BL Lac objects, when the continuum dominates the emission

lines toward the moving direction. The different radio emission property between radio loud and radio quiet objects may be attributed to the different spin rates of the central black holes (Wilson & Colbert 1995).

1.2 PHYSICAL PROPERTIES OF AGN

The detailed investigation of the emission lines of AGNs reveals a large amount of information regarding the physical conditions and kinematics of the emission line region. As the emission lines are divided into broad and narrow lines, so are the emission line regions, *i. e.* , into broad line region (BLR) and narrow line region (NLR). The broad lines are composed of permitted lines and semi-forbidden lines like C III]λ1909. The existence of C III]λ1909 sets the upper bound of the electron density in the BLR to be $n_e \lesssim 10^{11}\,\mathrm{cm}^{-3}$ and the absence of broad forbidden lines gives the lower bound of $10^7\,\mathrm{cm}^{-3}$. The permitted lines include high ionization lines such as C IV λ1549, N V λ1240 and O VI λ1035, and low ionization lines include Mg II λ2798 and Fe II lines.

Because of the large velocity widths, the BLR must be located near the central engine of the AGN. The line luminosity changes usually lag behind the change in the continuum luminosity from several days to several months. Assuming that the line variation is caused by the continuum change, the location of the BLR can be constrained. The reverberation mapping, or the study of correlation between the continuum and the line variability, gives the approximate distances between the continuum source and the line emitting regions (Peterson *et al.* 1991, Peterson *et al.* 1993). The study shows that the BLR is located within 1 parsec from the central continuum source and that the emitting regions of highly ionized lines are usually closer than those corresponding to the low ionization lines. Furthermore, in many objects highly ionized lines are blueshifted with respect to low ionized lines (*e. g.* , Wilkes 1984). The BLR is believed to be stratified, with the high ionization region being closer to the central continuum source.

The kinematic structure of the emitting line region can be probed from a detailed investigation of the line profiles. Assuming that the broadening is purely due to the Doppler shift, the velocity widths of typical broad lines ~ 5000 km s^{-1} imply that the central black hole has a mass up to 10^9 $M_\odot$. There is also evidence that our own Galaxy has an inactive nucleus characterized by a black hole with mass $\sim 10^6$ $M_\odot$. Most of the broad lines have smooth profiles, implying that either the emitting gases form a continuous flow, or there are a large number of small emitting clouds filling the velocity space continuously. Some lines show asymmetric profiles and others show symmetric profiles. This suggests that gas motion in the BLR cannot be simply interpreted as outflow or inflow.

Emmering *et al.* (1992) calculated the line profiles from an ensemble of moving clouds driven by hydromagnetic winds to obtain the logarithmic profile consistent with observation. A recent study of the UV emission line profiles of a few low-redshift quasars from the Hubble Space Telescope shows that most lines have symmetric line profiles about the line center and that they are smooth. This implies that the purely radial outflow or inflow is implausible because they respectively lead to blue or red asymmetry respectively (Laor *et al.* 1994). Some quasars show blue asymmetry and others show red asymmetry and this may have a correlation with the luminosity of the quasar where more luminous ones show more red asymmetry. Gravitational redshift due to the central black hole is a possible explanation for this correlation (Corbin 1995).

The coexistence of both highly ionized and low ionized species implies that there exists an almost neutral region, that is optically thick to Ly α, which means that the column density can be higher than $10^{23}\,\mathrm{cm}^{-2}$. There is no apparent discontinuity around the Lyman limit, which is expected if the continuum source is completely covered by the line-emitting gas with optical depth $\tau(912\text{Å}) \gtrsim 1$. Hence the observed low ionization lines imply that the BLR consists of a large number of small clouds covering a fraction of $\lesssim 0.1$ of the continuum source. One

quasar *e. g.* , PG 1630+377 shows continuum drop around the Lyman limit, and this can be interpreted as the partial Lyman limit edge (See Tripp *et al.* 1994). The size of each cloud ranges from $10^{12} - 10^{16}$ cm assuming a column depth of $10^{23}\,\mathrm{cm}^{-2}$. The observed H$\beta$ luminosities of order 10^{43} ergs s^{-1} constrain the size of the total illuminated surface to be $\sim 10^{17}$ cm and hence the corresponding filling factor is $\sim 10^{-9}$ (*cf.* Mathews & Capriotti 1985).

However, this view is not without difficulty, in that the confinement mechanism and the origin of these clumpy clouds are not settled. Each cloud would expand on a sound-crossing time scale which is $t_{int} \sim 10^8$ s, where the crossing time of the BLR is $t_{cross} \sim 10^{11}$ s. This implies that unless there is an efficient way to produce a large number of clouds continuously, the clouds must be confined. If the confinement is achieved thermally, then an ambient medium with a lower density ($\hat{n} \sim 10^5\,\mathrm{cm}^{-3}$) and a higher temperature($\hat{T} \sim 10^9$ K) should be invoked (Krolik *et al.* 1981).

Magnetic field was suggested as another confining agent by Rees (1987). If the BLR is threaded ubiquitously by a magnetic field of $\gtrsim 0.1$ G, the confinement problem can be alleviated and this magnetic field may act as an accelerating agent of the line-emitting clouds (See also Emmering *et al.* 1992).

Recently, Murray *et al.* (1995) suggested another model of the BLR, in which broad emission lines originate from accretion disk winds that are accelerated radiatively. In their model, the broad absorption troughs are seen when the observer's line of sight is in the equatorial direction. This model does not require the existence of a large number of clumpy clouds and hence entails no confinement problems, and furthermore, it naturally explains the approximate ratio of the number of observed BALQs to that of non-BALQs. However, this model invokes a much larger ionization parameter than is usually assumed in the standard cloud model. The existence of O VII and O VIII edges in X-ray band observations of BALQs may constrain this model.

Similar analyses can yield information on the NLR. The existence of narrow forbidden lines implies that the typical density is $10^3 - 10^6\,\mathrm{cm}^{-3}$ and the distance from the continuum source is about 100 pc, which can be optically resolved in the case of nearby Seyfert galaxies.

1.3 POLARIZATION MECHANISMS

When the system provides a specific direction characterizing the underlying anisotropy, polarization may develop with respect to that direction. The anisotropy can be introduced by geometry, kinematics, or by an external field such as a magnetic field. Hence the polarization study can give an important insight into the detailed structure of the system. However, this is not always the case. For example, multiple scattering randomizes the scattered radiation field, which means that no measurable polarization is obtained when the relevant scattering optical depth is much greater than 1.

In AGN, the relevant processes generating polarization include electron scattering (Thomson scattering), scattering by dust, and resonance line scattering by ions. Electron scattering is characterized by the wavelength independent cross section (Thomson cross section), which ensures that the photon propagation can be well approximated by a random walk process (no diffusion in the frequency space). Furthermore, a single 90° scattering yields complete polarization. Thus, the observational signature for electron scattering is a constant degree of polarization covering a large spectral range with constant position angle.

A certain fraction of the IR spectra is believed to be caused by dust in quasars. It is also responsible for the reddening. The scattering by dust gives a wavelength dependent polarization . The detailed behavior is determined by the chemical composition, size, and the geometrical shape. The polarization from dust has been fairly intensively studied in the context of the interstellar medium, where alignment by magnetic field is important. However, the dust content in AGN is very poorly constrained. (Laor & Draine 1993)

Resonance line scattering is characterized by a strong dependency on wavelength and large cross section at the line center, as the name 'resonance' implies. It usually refers to the permitted bound-bound transition between the ground state and an excited state. In this case, the cross section is approximately given by the square of the wavelength at line center and the resonance width is equal to that of the natural line broadening associated with the spontaneous emission rate (Einstein A coefficient). Furthermore, unlike electron scattering, it depends upon the angular momentum quantum numbers associated with the ground state and the excited state. The usual rule is that higher quantum numbers lead to smaller values of degree of polarization, because the re-radiated field is the superposition of various transitions between larger number of sublevels which usually produces a more isotropic radiation field. In the case of single scattering, the transition $J=0 \rightarrow 1$ gives the same polarized scattered emission as that of the electron scattering. However, the transition $J=1/2 \rightarrow 3/2$ produces a degree of polarization of only 0.43 from a single perpendicular scattering and lower degrees of polarization are obtained from other transitions. This illustrates the important point that the atomic physics should be carefully treated when the resonance line polarization is involved. There are more complicating factors to be considered. Firstly, if the collision frequency is small compared with the radiative excitation rate and if the radiation field is anisotropic, then this may lead to an uneven population in the ground state sublevels. This is analogous to alignment of dust by an external agent such as a magnetic field, and hence the resultant polarization may be enhanced. Secondly, a typical atom has many excited states which may also be multiplets. Therefore, in order to determine the ground state sublevel population, a number of transitions should be considered.

In quantum mechanics, a system which can be specified only statistically is governed by a density operator and the system is said to be in a mixed state. The state of a photon is represented as its wave vector and the state of the polarization.

This motivates the use of density operators for computation of polarization of resonantly scattered line photons, since the scattering ions can be also specified by a density matrix representing the relative population of the ground state sublevels.

In Chaper 2, basic atomic physics is discussed to establish a formalism for the computation of polarization considering collisional mixing, radiative mixing and magnetic mixing, where the terms emphasize the relative importance of collision frequency, radiative excitation rate, and magnetic gyro-frequency respectively.

1.4 PHOTOIONIZATION MODEL

Quasar luminosities range from 10^{44} ergs s^{-1} to 10^{48} ergs s^{-1} with a typical luminosity being 10^{46} ergs s^{-1}. The nonstellar continuum of a typical quasar is usually approximated by a power law $f_\nu \propto \nu^\alpha$, where the power index α varies over frequency ranges (*cf.* Mathews & Ferland 1987). However, there is a conspicuously high luminosity in the optical to UV range, which constitutes a significant fraction of the total energy output. This is the famous "Big Blue Bump," which is believed to be the thermal component originating from the inner accretion disk around the massive black hole. Assuming that the efficiency of gravitational energy conversion is 0.1, a typical mass accretion rate of $\dot{M} \sim 1$ $M_\odot$/year is required to explain the quasar luminosity.

In the presence of a highly luminous ionizing UV continuum, a natural way to explain the emission lines is the photoionization model. In this model, an isolated small cloud with column depth of $N \sim 10^{23}$ cm^{-2} is exposed to the assumed incident ionizing UV continuum and the emission spectra are obtained by solving the thermal equilibrium and the statistical balance equations. One of the most important parameters is the ionization parameter U defined as the ratio of the incident ionizing photon density to the hydrogen density, *i. e.* ,

$$U \equiv \int_{\nu_0}^{\infty} \frac{L_\nu}{h\nu} d\nu / (4\pi r^2 c n_H),$$

where c is the speed of light, r is the distance from the continuum source, ν_0 is the frequency corresponding to the Lyman limit and the n_H is the hydrogen density. Typically, the ionization parameter U is chosen to be $10^{-2} - 1$.

For thermal equilibrium, heating and cooling should be considered. The important processes are the bound-free heating and cooling (or photoionization and recombination), collisional excitation and de-excitation, free-free heating and cooling, and Compton heating and cooling. Other processes include dielectronic recombination, three-body recombination, and charge exchange. (*cf.* Krolik & Kallman 1988)

Most permitted lines are optically thick ($\tau \sim 10^4 - 10^6$) in a standard BLR cloud, and in general the exact solution of the equation of radiative transfer is not available. One of the most popular approximation methods dealing with radiative transfer is the escape probability formalism. The escape probability is defined as the probability that a photon emerges at either surface of the given slab and is usually given as a function of the optical depth at the point (local escape probability). Using this escape probability p_{ij} the radiative transfer is reduced to that of optically thin case, where the equation takes much simpler form in which the Einstein coefficient A_{ij} is replaced by the effective Einstein coefficient $p_{ij}A_{ij}$. This approximation is especially good when most scatterings are local *i. e.* , there is little diffusion in real space and the escape is dominated by diffusion in the frequency space by large number of scatterings. This assumption is usually met when the optical depth of the given line is less than 10^4 or 3 Doppler widths. (*e. g.* , Netzer 1990).

In a standard line-emitting cloud in the BELR, the line photons are generated by collisional excitation followed by radiative de-excitation. The large cross section associated with resonance scattering gives the optical depth $\tau \sim 10^6$ for permitted lines(*e. g.* CIVλ1549) and $\tau \sim 1$ for semi-forbidden lines such as CIII]λ1909. Hence, if each individual cloud is aspherical and also the global distribution is anisotropic (*e. g.* jet-like or disk-like distribution), then the emergent

semi-forbidden photons can be polarized because of the optimum optical depth condition $\tau \sim 1$ (*e. g.* Cohen *et al.* 1995). A large velocity gradient expected in a violent environment near AGN can reduce the number of scattering required to escape the cloud. Furthermore, this velocity gradient naturally may introduce the direction of anisotropy, with respect to which parallel or perpendicular polarization can develop.

In Chapter 3, a Monte Carlo code is developed using the formalism described in Chapter 2, to compute the polarization of resonantly scattered line photons emerging from anisotropic clouds and clouds expanding with non-spherical velocity gradients, where the conditions are believed to be appropriate inside the BELR of AGN.

1.5 BROAD ABSORPTION LINE QUASARS

The broad absorption line quasars, which comprise about 10 per cent of radio quiet quasars, show deep absorption troughs in their highly ionized permitted emission lines, including C IV, Si IV, N V and O VI (*e. g.* Weymann *et al.* 1991, Turnshek, 1988). About 15 per cent of BALQs also show absorption troughs in low ionization lines such as Mg II, Al III (*e. g.* Voit *et al.* 1993). These low ionization BALQs have reddened spectra, and are found to be more numerous in IR-selected quasars than in optically selected quasars.

The absorption occurs to the blue side with velocity widths up to 0.1 c which implies that the material is accelerated radially outward. Hamann *et al.* (1993) investigated the geometry and kinematics of BALQs and concluded that the BAL regions have a small covering factor $f_{BALR} \lesssim 0.25$, and they also calculated the line profiles expected from conical wind and disk wind models. The emission property of BALQs is found to be almost identical to that of non-BALQs (See Turnshek *et al.* 1988 and Weymann *et al.* 1991). According to Turnshek *et al.* 1988, Ly α is relatively weak and heavily absorbed by N Vλ1240. This suggests that the BALR

lies outside or is cospatial with the BELR. The line flux ratio of N V to C IV is enhanced in the BALQs and this may be interpreted as the scattered component contribution to N V. Some BALQs show multiple troughs separated by the same velocity difference between Ly α and N V. This "line-locking" phenomenon can be explained by a sudden acceleration of N V ions by Doppler shifted Ly α photons going into resonance with them. The velocity boost induced by N V ions decreases the local optical depth of a given ion species at this velocity to leave a small feature in the broad absorption trough (*cf.* Arav *et al.* 1995). The line-locking also implies that radiative acceleration is important in the BALR.

Small covering factor and similar emission property to that of normal non-BALQs suggest that BALQs are not intrinsically different from non-BALQs, but that BALQs are the same population viewed in a special direction. The exact nature of the outflow is not clear, and it is still uncertain whether the outflow is bipolar (jet-like) or equatorial (disk-like wind). Many suggestions have been made to explain the BAL phenomena. Scoville & Norman (1995) proposed that BAL material has stellar origin, accelerated by continuum radiation. Accretion disk winds are invoked as a source for broad emission lines as well as the broad absorption lines by Murray *et al.* (1995). Radiatively driven wind may be responsible for the deep absorption troughs of BALQ's (Arav *et al.* 1994).

The detailed dynamic models of BALQs are not available at present. However, observational data constrain kinematic models of BALQs. The absorption troughs are smooth up to resolutions of $\Delta V \sim 10$ km s^{-1}, and hence the flow is either continuous up to 0.1c or it consists of a large number of small clouds filling up the velocity space (*e. g.* Barlow 1995).

It is natural to expect that resonance line scattering plays an important role in the BALR. Hence, the absorption troughs may be at least partially filled by resonantly scattered photons by the same ions from other lines of sight, and a measurable degree of polarization in the absorption trough is expected to develop.

Because of the strong wavelength dependency of the resonance scattering, the Sobolev method is appropriate when the scatters are moving with speed larger than the thermal speed (*e. g.* Sobolev 1947, Rybicki & Hummer 1978). The Sobolev method is summarized as finding a family of surfaces characterized by the velocity components along a specified direction and assessing the local optical depth at each point by the kinematics. The Sobolev optical depth is locally determined from the column depth between two neighboring surfaces where the velocity components differ on of order the thermal velocity. This approximation is often invoked for analysis of systems like moving stellar atmospheres or stellar winds.

In Chapter 4, the same Monte Carlo code used in the previous chapter is modified to incorporate the Sobolev approximation to compute the polarization of broad absorption troughs of BALQs. Furthermore, various local problems and multiplet transitions with radiative mixing are also discussed.

1.6 SPECTROPOLARIMETRY OF AGN

For a semi-infinite slab of scatterers where the light source is located deep inside, Chandrasekhar (1950) showed that the pure electron scattering produces 11.7 percent degree of polarization with the direction parallel to the plane for the photons emerging almost parallel to the plane. Hence, geometrically thin, but optically thick accretion disk leads us to conclude that high polarization up to 12 percent should be obtained dependent on the viewing angle (*e. g.* Rees 1975, Lightman & Shapiro 1975). However, many polarimetric observations show low polarization $\lesssim 1\%$(*e. g.* Stockman, Angel, & Miley 1979) contradicting this view. Furthermore some Seyfert 1 galaxies show low continuum polarization parallel to the radio axis (*e. g.* Antonucci 1993). Addition of the absorption opacity by ions to the purely electron scattering atmosphere reduces the polarization (*e. g.* Laor, Netzer, & Piran 1990). Magnetic field can also depolarize the radiation by rotating the plane of polarization because the index of refraction is dependent on the circular polarization state when the radiation propagates parallel to the magnetic field

(Faraday rotation). In radio-loud quasars with a one-sided jet, polarization asymmetry has been observed between the jet-side and the opposite side (Laing 1988, Garrington *et al.* 1988). More depolarization is seen in the opposite side than the jet-side and this is interpreted as the more Faraday rotation by foreground plasma external to the continuum source.

As mentioned in the previous section, Antonucci & Miller (1985) used spectropolarimetry to identify broad features similar to those found in Seyfert 1 type spectra in the polarized spectra of a Seyfert 2 galaxy NGC 1068. They attributed the scattering source to electrons located at high latitudes and assumed that a thick molecular torus may block the direct view of the broad line component. Subsequently, Miller & Goodrich (1990), using spectropolarimetry, showed that many Seyfert 2 galaxies share the same property as NGC 1068, providing a fairly convincing argument that Seyfert 2 galaxies are normal Seyfert 1 galaxies observed in the special direction. Their work stimulated the work on construction of the so-called unification scheme of AGNs, in which numerous phenomena of AGNs can be interpreted as the aspect effects, using a few parameters such as the mass of the central black hole, the accretion rate and angular momentum (*cf.* Blandford 1990, Lawrence 1987). According to this scheme, the bright sources analogous to Seyfert galaxies are radio-quiet quasars, of which about 10 percent are BALQs. A fraction ($\sim 0.1 - 0.3$) of Seyfert 1 galaxies show broad absorption troughs in their spectra, and these are not so deep as the counterparts of BALQs and the velocity widths are also small (*e. g.* Shull & Sachs 1993).

It is well known that some optically variable quasars show high polarization and some BALQ like PHL 5200 shows large polarization up to $\sim 12\%$ in the absorption trough (*e. g.* Stockman *et al.* 1981, Glenn *et al.* 1994, Cohen *et al.* 1995). Spectropolarimetry of a BALQ is extremely difficult because of a small number of photons in the absorption troughs. Therefore, large telescopes having a good photon-collecting capability are needed for obtaining spectropolarimetric data

with significant signal-to-noise ratio. The Keck telescope, the first (and currently only one) 10 m class telescope in the world, is the most suitable instrument for spectropolarimetry of faint objects.

Recent spectropolarimetry of BALQs PHL 5200, 0105-266, obtained by Cohen *et al.* (1995) reveals that the continuum is moderately polarized with a slightly increasing degree of polarization toward the blue side and constant position angle. On the other hand the prominent UV emission lines are not polarized, with possible exception of semi-forbidden carbon line in PHL 5200. However, in the absorption line troughs a high degree of polarization up to 12 per cent has been observed. In Chapter 4, observational ramifications concerning the BALQ spectropolarimetry are also discussed.

Another recent quasar spectropolarimetry has been performed on Hubble Space Telescope by Koratkar *et al.* 1995. They observed a few radio quiet quasars and found that one of them (PG 1630+377) shows a steep rise in the degree of polarization in the far UV $\lambda \lesssim 800\mathring{A}$. If resonance scattering is the source of polarization, the polarization should be sensitively dependent on the quantum numbers associated with the transition, and optical depth. In the final chapter, using photoionization assumption and considering the polarization behavior of multiplet transitions described in the previous chapter, the expected polarization is discussed.

REFERENCES

Angel, J. R. P., & Stockman, H. S. 1980. *Annu. Rev. Astron. Astrophys.*, **18**, 321.

Antonucci, R. R. 1993. *Annu. Rev. Astron. Astrophys.*, **31**, 473.

Antonucci, R. R. J., & Miller, J. S. 1985. *Ap. J.*, **297**, 621.

Arav, N., Li, Z. Y., & Begelman, M. C. 1994. *Ap. J.*, **432**, 62.

Blandford, R. D. 1990. *Active Galactic Nuclei*, Berlin: Springer-Verlag.

Emmering, R.T., Blandford, R.D., & Shlosman, I. 1992. *Ap. J.*, **385**, 460.

Garrington, S. T., Leahy, J. P., Conway, R. G., & Laing, R. A. 1988. *Nature*, **331**, 147.

Hamann, F., Korista, K. T., & Morris, S. L. 1993. *Ap. J.*, **415**, 541.

Mathews, W. G., & Capriotti, E. R. 1985. Astrophysics of Active Galaxies and Quasi-stellar Objects, Edited by J. S. Miller, University Science Books, Mill Valley.

Miller, J. S., & Goodrich, R. W. 1990. *Ap. J.*, **355**, 456.

Koratkar, A., Antonucci, R. R. J., Bushouse, H., & Kinney, A. 1995. *Ap. J. Lett.*, in press.

Koratkar, A., Antonucci, R. R. J., Goodrich, R. W, Bushouse, H., & Kinney, A. 1995. *Ap. J.*, in press.

Krolik, J. H. & Kallman, T. R. 1988. *Ap. J.*, **324**, 714.

Krolik, J. H., McKee, C. F., & Tarter, C. B. 1981. *Ap. J.*, **249**, 422.

Laing, R. A. 1988. *Nature*, **331**, 149.

Laor, A., Bahcall, J. N., Buell, T. J., & Schneider, D. P. 1994. *Ap. J.*, **420**, 110.

Laor, A., & Draine, B. T. 1993. *Ap. J.*, **402**, 441.

Lawrence, A., 1987. *Publ. Astr. Soc. Pacific*, **99**, 309.

Murray, N., Grossman, S. A., & Chiang, J. 1995. *Nature*, in press.

Netzer, H. 1990. *Active Galactic Nuclei*, Berlin: Springer-Verlag.

Khachikian, E. Y. & Weedman, D. W. 1974. *Ap. J.*, **192**, 581.

Osterbrock, D. E. 1989. Astrophysics of Gaseous Nebulae abd Active Galactic Nuclei, University Science Books, Mill Valley.

Peterson, B.M. *et al.* 1991. *Ap. J.*, **368**, 119.

Peterson, B.M. *et al.* 1994. *Ap. J.*, **425**, 622.

Rees, M.J. 1987. *MNRAS*, **228**, 47P.

Rybicki, G. B.,& Hummer, D. G. 1978. *Ap. J.*, **219**, 654.

Shull, J. M., & Sachs, E. R. 1993. *Ap. J.*, **416**, 536.

Seyfert, C. K. 1943. *Ap. J.*, **97**, 28.

Sobolev, V. V. 1947. Moving Envelopes of Stars (Leningrad: Leningrad State University)(English trans.: S. Gaposchkin [Cambridge: Harvard University Press, 1960].

Stockman, H. S., Angel, J. R. P.,& Hier, R. G. 1981. *Ap. J.*, **243**, 404.

Tripp, T. M., Bechtold, J., & Green, R. F. 1994. *Ap. J.*, **433**, 533.

Turnshek, D. A. 1988. in Space Telescope Sci. Inst. Symposium 2, QSO Absorption Lines: Probing the Universe,ed. S. C. Blades, D. A. Turnshek, & C. A. Norman (Cambridge: Cambridge Univ. Press), p.17.

Voit, G. M., Weymann, R. J., & Korista, K. T. 1993. *Ap. J.*, **413**, 95.

Weymann, R. J., Morris, S. L., Foltz, C. B.,& Hewett, P. C. 1991. *Ap. J.*, **373**, 23.

Wilkes, B. J. 1984. *MNRAS*, **207**, 73.

Wills, B. J., Wills, W. D., Breger, M., Antonucci, R. R. J., & Barvainis, R. 1992. *Ap. J.*, **398**, 454.

Wilson, A. S., & Colbert, E. J. M. 1995. *Ap. J.*, **438**, 62.

2

On the Polarization of Resonantly Scattered Emission Lines I. Emission and Absorption Coefficients in an Anisotropic Radiation Field

H. W. Lee, R. D. Blandford, Caltech, Pasadena, CA 91125.

L. Western, Aerospace Corporation.

Abstract

Source functions and absorption coefficients for polarized radiation in a given anisotropic radiation field are calculated for a variety of permitted electric dipole transitions in the L-S coupling limit. Collisional, radiative and magnetic mixing of the ground sublevels are all considered. The polarization of the self-consistent, emergent radiation field is computed, treating the radiative transfer using an anisotropic escape probability formalism. It is found that the radiative mixing can enhance the polarization for transitions with large angular momentum and degrees of polarization $\lesssim 10\%$ are obtained for small angular momentum transitions.

1. Introduction

Recent developments in spectropolarimetry have made possible the measurement of linear polarization of broad emission lines in Active Galactic Nuclei (AGN) with accuracies ~ 0.3 per cent (*e.g.* Goodrich 1991, Netzer 1990). Such measurements provide a possible probe of the hitherto uncertain distribution of emission (and absorption) line gas in phase space. This motivates calculations of the degree of linear polarization to be expected from simple source models involving an aggregation of discrete clouds. However somewhat unfamiliar physical principles are involved and it is the purpose of this paper to elucidate them.

Most of the spectral lines of interest involve ground state, electric dipole transitions in which a photon is created following an electron collisional excitation. This photon scatters many times off other ions within the same cloud until its Doppler shift is large enough to allow it to escape. Spatial transport within the cloud and scattering by other clouds is relatively unimportant in most simple cases. If the radiation field is isotropic, then polarization of the emergent radiation field should not develop. However, these clouds, which are popularly supposed to be moving with Mach numbers in excess of 1000, are likely to have significant internal velocity shear and this will cause photon escape to be anisotropic. Under these conditions, polarization, roughly proportional to the anisotropy in the radiation field, should be observed.

In section 2, we describe the atomic physics relevant to the computation of the degree of polarization from resonance line scattering. We calculate the absorption coefficient and source function for radiation with an arbitrary distribution in polarization and angle and a variety of permitted transitions. In this section, it is assumed that collisions populate the ground substates equally. In section 3, we relax this assumption and, instead, assume that radiative excitation is more frequent than collisional excitation, as indeed is likely to be the case for strong permitted lines in an AGN emission line cloud. We show that the ground sublevels will now be unequally populated in the steady state and that the polarising effect will mostly be enhanced. A further complicating effect involves magnetic field. If the electron cyclotron frequency significantly exceeds the radiative excitation rate, or for semi-forbidden lines the Einstein A coefficient, then either the ground or the excited state sublevels can be mixed so that they are effectively resolved into eigenstates of the magnetic perturbation operator. A field of no more than ~ 0.01 G may be all that is necessary for this effect to be important. Magnetic fields of larger strength have been invoked in some broad emission line region models (*e.g.* Emmering, Blandford & Shlosman 1992). This is discussed in section 4. In section 5 we apply our result to a calculation of the polarization of the escaping radiation assuming a frequency- and polarization- independent but angle-dependent escape

probability. This can be used in simple estimates of the magnitude of the emergent polarization. Our conclusions are briefly collected in section 6.

In Paper II, we shall use this formalism in Monte Carlo calculations of radiative transfer in model emission line clouds. These calculations do not assume complete frequency re-distribution as in section 5 of this paper. We shall also consider spatial transport under conditions of reduced optical depth appropriate to the semi-forbidden emission lines. In Paper III, we will then consider global models of AGN broad emission and absorption line clouds and compute the predicted degree of linear polarization from spatially unresolved observations

2. Emission and absorption coefficients - collisional mixing

Consider an ion described under the Russell-Saunders (L-S coupling) approximation. The ground state is characterized by combined spin S, orbital angular momentum L and total angular momentum J quantum numbers. In permitted, electric dipole transitions, the selection rules: $\Delta S = 0, \Delta L = 0, \pm 1, \Delta J = 0, \pm 1$, $(0 \rightarrow 0$ forbidden) operate. Let the subscript g denote the ground state and subscript e the excited state. The ground and excited states have $2J_{g,e}+1$ degenerate sublevels labeled by additional quantum numbers $M_{g,e} \equiv g, e$ varying between $-J_{g,e}$ and $J_{g,e}$. Transitions between sublevels of the ground and the excited states are limited by the selection rule $\Delta M = e - g = 0, \pm 1$, $(0 \rightarrow 0$ forbidden for $\Delta J = 0)$.

Using standard, time-dependent perturbation theory (*e.g.* Merzbacher 1961), it can be shown that a pulse of polarized radiation will induce a transition of the ion from an initial, pure ground state $|g>$ to an excited, final state expanded in terms of orthonormal eigenfunctions $|e>$ as $|e> c_e$, where the coefficient is

$$c_e = \frac{-i|e|}{\hbar} < e|\mathbf{x} \cdot \tilde{\mathbf{E}}|g >, \tag{2.1}$$

where $\tilde{\mathbf{E}} = \tilde{E}_q \mathbf{e}_q$ is the Fourier transform of the wave electric vector and $|e|$ is the electronic charge. (In this paper we sum implicitly over repeated indices unless

explicit summations are given.) The coefficient c_e is assumed to be much less than unity.

Without loss of generality, we choose a particular set of Cartesian coordinates (x, y, z) and expand the sublevels in eigenstates of J_z. We shall also use standard spherical polar coordinates (r, θ, ϕ). The electric vector is then conveniently expanded in an orthonormal basis with (ion) basis vectors $\mathbf{e}_q$:

$$\begin{aligned} \mathbf{e}_- &= 2^{-1/2}(\hat{\mathbf{x}} - i\hat{\mathbf{y}}) \\ \mathbf{e}_0 &= \hat{\mathbf{z}} \\ \mathbf{e}_+ &= 2^{-1/2}(-\hat{\mathbf{x}} - i\hat{\mathbf{y}}). \end{aligned} \tag{2.2}$$

However, for the ingoing and outgoing photon states we use a two component (photon) basis $\mathbf{e}_\alpha$, comprising $\mathbf{e}_{||}$ lying in the $\mathbf{n} - \hat{\mathbf{z}}$ plane, where $\mathbf{n}$ is the direction of wave propagation and $\mathbf{e}_\perp$ along the direction $\mathbf{n} \times \hat{\mathbf{z}}$. (See Fig. 1.)

We define a 2×3 matrix, $S_{\alpha q}$, to transform from the ion basis to the photon basis associated with a particular direction $\mathbf{n}$

$$\mathbf{e}_\alpha = S_{\alpha q}\mathbf{e}_q, \tag{2.3}$$

$$S_{\alpha q} = \begin{pmatrix} 2^{-1/2}\cos\theta e^{i\phi} & -\sin\theta & -2^{-1/2}\cos\theta e^{-i\phi} \\ 2^{-1/2}ie^{i\phi} & 0 & 2^{-1/2}ie^{-i\phi} \end{pmatrix}. \tag{2.4}$$

The spontaneous transition rate $d\dot{P}$ from the excited state $|e>$ to the ground state $|g>$ creating a photon in polarization $\mathbf{e}_\alpha$ propagating along a direction lying in $d\Omega$ can be written

$$d\dot{P} = A|M_{eg}(\mathbf{e}_\alpha)|^2 d\Omega, \tag{2.5}$$

where A is the total Einstein A coefficient from an excited state and $M_{eg}(\mathbf{e}_\alpha)$ is proportional to the matrix element for the transition. We can write

$$M_{eg}(\mathbf{e}_\alpha) = S_{\alpha q}R^q_{eg}, \tag{2.6}$$

where R^q_{eg} is a (normalized) Clebsch-Gordan coefficient for an angular momentum change of unity and $q = e - g = 0, \pm 1$ for an electric dipole transition. According

to the Wigner-Eckart theorem, the Einstein A coefficient depends just on J_g, J_e (*e.g.* Merzbacher 1961). The Clebsch-Gordan coefficients can be written in terms of the quantum numbers of the excited state

$$\sqrt{8\pi/3}R^1_{eg} \equiv < e|V_q|g > = \left[\frac{(J_e+e)(J_e+e-1)}{2J_e(2J_e-1)}\right]^{1/2}, \quad \Delta J = 1$$

$$\sqrt{8\pi/3}R^0_{eg} \equiv < e|V_q|g > = \left[\frac{2(J_e-e)(J_e+e)}{2J_e(2J_e-1)}\right]^{1/2}, \quad \Delta J = 1$$

$$\sqrt{8\pi/3}R^{-1}_{eg} \equiv < e|V_q|g > = \left[\frac{(J_e-e)(J_e-e-1)}{2J_e(2J_e-1)}\right]^{1/2}, \quad \Delta J = 1$$

$$\sqrt{8\pi/3}R^1_{eg} \equiv < e|V_q|g > = -\left[\frac{(J_e+e)(J_e-e+1)}{2J_e(J_e+1)}\right]^{1/2} \quad \Delta J = 0$$

$$\sqrt{8\pi/3}R^0_{eg} \equiv < e|V_q|g > = \frac{\sqrt{2}e}{[2J_e(J_e+1)]^{1/2}}, \quad \Delta J = 0$$

$$\sqrt{8\pi/3}R^{-1}_{eg} \equiv < e|V_q|g > = \left[\frac{(J_e-e)(J_e+e+1)}{2J_e(J_e+1)}\right]^{1/2}, \quad \Delta J = 0$$

$$\sqrt{8\pi/3}R^1_{eg} \equiv < e|V_q|g > = \left[\frac{(J_e-e+1)(J_e-e+2)}{2(J_e+1)(2J_e+3)}\right]^{1/2}, \quad \Delta J = -1$$

$$\sqrt{8\pi/3}R^0_{eg} \equiv < e|V_q|g > = -\left[\frac{2(J_e-e+1)(J_e+e+1)}{2(J_e+1)(2J_e+3)}\right]^{1/2}, \quad \Delta J = -1$$

$$\sqrt{8\pi/3}R^{-1}_{eg} \equiv < e|V_q|g > = \left[\frac{(J_e+e+1)(J_e+e+2)}{2(J_e+1)(2J_e+3)}\right]^{1/2}, \quad \Delta J = -1$$

where $q \equiv e - g = 0, \pm 1$ and $\Delta J \equiv J_e - J_g = 0, \pm 1$ (*e.g.* Condon & Shortley 1951). Note that these matrix elements are all real. These are normalized so that

$$\begin{aligned}\sum_{\alpha g}\int d\Omega |M_{eg}(\mathbf{e}_\alpha)|^2 &= \sum_{\alpha g} R^q_{eg}R^{*q'}_{e'g}\int d\Omega S_{\alpha q}S^*_{\alpha q'} \\ &= \frac{8\pi}{3}\sum_g R^q_{eg}R^{*q}_{eg} = 1.\end{aligned} \tag{2.7}$$

For generality, we should describe the ground and excited states using a density matrix. As long as the probability that a given ion is in an excited state is small, we can normalize the ground state density matrix by

$$\rho_{gg'} = \frac{c_g c^*_{g'}}{c_{g''}c^*_{g''}}. \tag{2.8}$$

We normalize the excited state to the ground state so that $c_e c_e^* \ll 1$ is the total probability that an ion is in an excited state.

Suppose that collisions equally populate the ground sublevels. We average over many ions to form the mean density matrix

$$\bar{\rho}_{gg'} = (2J_g + 1)^{-1}\delta_{gg'}. \tag{2.9}$$

We are interested in the rate of stimulated excitation from the ground level. Let the total intensity be $I_{\nu\Omega}$ and describe the polarization by another density matrix normalized so that

$$P_{\alpha\alpha'}(\theta,\phi) = \frac{\tilde{E}_\alpha \tilde{E}^*_{\alpha'}}{\tilde{E}_{\alpha''}\tilde{E}^*_{\alpha''}}. \tag{2.10}$$

Now we write

$$I_{\alpha\alpha'} = I_{\nu\Omega}P_{\alpha\alpha'}. \tag{2.11}$$

The photon occupation number in this state is

$$n = \frac{c^2 I_{\alpha\alpha'}}{h\nu^3}. \tag{2.12}$$

If we ignore the possibility of collisional de-excitation, then, after each excitation, there will be a spontaneous transition back to the ground state. (We also assume that the radiation field is sufficiently weak that stimulated emission can be ignored.) Using equation (2.1) we can derive an evolution equation for the rate of change of the excited state

$$\frac{d\bar{\rho}_{ee'}}{dt} = A\int M_{eg}(\mathbf{e}_\alpha)\rho_{gg'}M^*_{e'g'}(\mathbf{e}_{\alpha'})nd\Omega - A\rho_{ee'}. \tag{2.13}$$

Hence in a steady state

$$\rho_{ee'} = \frac{c^2}{h\nu^3}\int d\Omega I_{\alpha\alpha'}M_{eg}(\mathbf{e}_\alpha)\rho_{gg'}M_{g'e'}(\mathbf{e}_{\alpha'}), \tag{2.14}$$

where we use the notation $M_{ge} = M^*_{eg}$.

We define the effective absorption coefficient $\mu_{\alpha\alpha'}$ for radiation in polarization state $P_{\alpha\alpha'}$ by

$$\mu_{\alpha\alpha'} = n_i A \frac{c^2}{\nu^2} \phi_\nu M_{eg}(\mathbf{e}_\alpha) \rho_{gg'} M_{g'e}(\mathbf{e}_{\alpha'}) \tag{2.15}$$

where $\phi_\nu = \frac{\lambda}{n_i} \frac{dn_i}{dv_\parallel}$ is the normalized ion velocity profile (assumed isotropic), the $v_\parallel$ is the velocity component along the incident photon direction and n_i is the total ion density. Note that we sum over all excited states. This absorption coefficient is that for a specific frequency in the line.

Now let us specialize to the case where the radiation field is axisymmetric along the $z-$direction. We need only consider parallel and perpendicular polarization(*cf.* Fig. 1). We also assume complete frequency redistribution. In other words the probability of emission at a given frequency ν is independent of the frequency of the absorbed photon and also described by ϕ_ν. Then the emissivity $j_{\alpha\alpha'}$ per steradian is given by

$$j_{\alpha\alpha'} = n_i \phi_\nu A h\nu M_{ge}(\mathbf{e}_\alpha) \rho_{ee'} M_{e'g}(\mathbf{e}_{\alpha'}). \tag{2.16}$$

The equation of radiative transfer for the parallel component is then

$$\frac{dI_\parallel}{ds} = -\mu_\parallel I_\parallel + j_\parallel, \tag{2.17}$$

and similarly for the orthogonal polarization. It is more convenient to define a source function

$$\begin{aligned} S_{\parallel,\perp} &= \frac{j_{\parallel,\perp}}{\mu_{\parallel,\perp}} \\ &= \frac{h\nu^3}{c^2} \left[\frac{M_{ge}(\mathbf{e}_{\parallel,\perp}) \rho_{ee'} M_{e'g}(\mathbf{e}_{\parallel,\perp})}{M_{eg}(\mathbf{e}_{\parallel,\perp}) \rho_{gg'} M_{g'e}(\mathbf{e}_{\parallel,\perp})} \right]. \end{aligned} \tag{2.18}$$

There is a complication that must be considered when the incident radiation is arbitrarily polarized. A substance that is capable of efficient absorption must also be dispersive. This implies that photons propagating between collisions must be resolved into the eigenstates of propagation and there may be a phase difference introduced by the propagation. In this paper, we shall restrict attention to simple geometries where there will be no such "propagation coupling" between different polarization states.

We now assume a fixed radiation field. The simplest example is the case of the unidirectional radiation field represented by

$$I(\theta,\phi) \propto \delta(\mu - 1). \tag{2.19}$$

The key process is that when the beam propagates along the $z-$ axis, there can only be upward transitions with $\Delta M = \pm 1$. The direct substitution of equation (2.19) into equation (2.14) gives

$$\rho_{ee'} \propto \delta_{ee'}(J_e(J_e-1)+e^2), \quad \Delta J = 1 \tag{2.20a}$$

$$\rho_{ee'} \propto \delta_{ee'}(J_e(J_e+1)-e^2), \quad \Delta J = 0 \tag{2.20b}$$

$$\rho_{ee'} \propto \delta_{ee'}((J_e+1)(J_e+2)+e^2), \quad \Delta J = -1. \tag{2.20c}$$

The net polarization for emission at right angles, P_0, is given by

$$P_0 = \frac{j_{\parallel}(0) - j_{\perp}(0)}{j_{\parallel}(0) + j_{\perp}(0)}, \tag{2.21}$$

where $j_{\parallel,\perp}(0) = j_{\parallel,\perp}(\mu = 0, \phi)$. By combining the equations(2.20 a b c) and equation (2.16) and substituting them into equation (2.21) we obtain

$$P_0 = \frac{(J_e+1)(2J_e+3)}{(26J_e^2 - 15J_e - 1)}, \quad \Delta J = 1 \tag{2.22a}$$

$$P_0 = \frac{(2J_e-1)(2J_e+3)}{(12J_e^2 + 12J_e + 1)}, \quad \Delta J = 0 \tag{2.22b}$$

$$P_0 = \frac{J_e(2J_e-1)}{(26J_e^2 + 67J_e + 40)}, \quad \Delta J = -1. \tag{2.22c}$$

In Table 1 P_0 is shown for the cases $J_e = 1, 2, 3, 4, 5$, and ∞ for all the possible transitions $\Delta J = \pm 1, 0$. Note that a $0 \rightarrow 1$ transition with a beam pattern of classical electron scattering produces 100% polarization when viewed from a perpendicular direction.(*e.g.* Hamilton 1947, Webster 1986)

The polarization for emission at an arbitrary angle P_μ can be calculated by considering the intensity contributions for each polarization given by

$$\begin{aligned} \Delta I_{\perp} &\propto j_{\perp}(0) \\ \Delta I_{\parallel} &\propto j_{\parallel}(0)\sin^2\theta + j_{\perp}(0)\cos^2\theta, \end{aligned} \tag{2.23}$$

and

$$P_\mu = \frac{\Delta I_\parallel - \Delta I_\perp}{\Delta I_\parallel + \Delta I_\perp} = \frac{P_0 \sin^2\theta}{1 + P_0 \cos^2\theta} \quad . \tag{2.24}$$

An isotropic radiation field naturally produces no polarization as may be quickly demonstrated. The same is true for a $P_1(\mu)$ variation ($\mu = \cos\theta$). We therefore adopt a variation $I(\mu) \propto \mu^2$. Lower spherical harmonic components can be added to this without changing the polarized flux. We use the rate equations to solve for the density matrix of the excited state for a variety of transitions. We can then compute the absorption cross section and emissivity as a function of μ for the two polarization states. The results are shown in Fig. 2.

As the ground sublevels are equally populated, the absorption coefficient is independent of the polarization. The source function is unpolarized when the observer lies along the $z-$axis (symmetry axis). What is rather surprising is that the source function is undetectably small for transitions with $J_e = J_g - 1$. For most common resonance transitions with $\Delta J = 1$, the source function is strongly polarising. The maximum value of $S_\perp/S_\parallel$ is 2 for a $0 \rightarrow 1$ transition (*e.g.* CIIIλ977).

3. Emission and Absorption Coefficients- Radiative Mixing

When the collision rate is sufficiently low relative to the radiative excitation rate, it is no longer assured that the ground sublevels will be equally populated.(*e.g.* Varshalovich 1965)

The electron collision rate C is given by

$$C = n_e \int_0^\infty v\sigma f(v) dv \sim 6 \times 10^2\,\mathrm{s}^{-1}, \tag{3.1}$$

where $f(v)$ is the Maxwellian velocity distribution and n_e is the electron density, and σ is the collision cross section. Here, we use the relation $\sigma \sim 10^{-15}\Omega/\omega\,\mathrm{cm}^2$ valid at a typical temperature of 10^4K, where Ω is the effective collision strength

and ω is the statistical weight (*e.g.* Osterbrock 1989). For many broad lines the values of the effective collision strength are collected by Osterbrock & Wallace (1977), typical values being $1 - 20$ dependent on the ion species and the temperature. For order of magnitude calculations we adopt $\Omega/\omega \sim 1$.

The radiative excitation rate R is given by

$$\begin{aligned} R &= \int d\nu n_\nu \sigma_\nu c \\ &\sim \frac{\pi e^2}{mc} f_{abs} n_{\nu 0} c \\ &\sim (8.0 \times 10^8 \,\mathrm{cm^3\,s^{-2}}) f_{abs} n_{\nu 0}, \end{aligned} \tag{3.2}$$

where n_ν is the photon density per unit frequency range, ν_0 is the resonance frequency, σ_ν is the scattering cross section at frequency ν and f_{abs} is the oscillator strength associated with the photon absorption.

The ionization parameter U is defined as the ratio of the H-ionizing photon density n_γ to the free electron density n_e, *i.e.* ,

$$U \equiv \frac{n_\gamma}{n_e}. \tag{3.3}$$

Suppose that we have a power spectrum of photon density given by

$$n_\nu \propto \nu^{-\frac{3}{2}}. \tag{3.4}$$

Then

$$\begin{aligned} n_\gamma &= \int_{\nu_{\mathrm{Ryd}}}^{\infty} n_\nu(\nu_{\mathrm{Ryd}}) \left(\frac{\nu}{\nu_{\mathrm{Ryd}}}\right)^{-\frac{3}{2}} d\nu \\ &= 2 n_\nu(\nu_{\mathrm{Ryd}}) \nu_{\mathrm{Ryd}}. \end{aligned} \tag{3.5}$$

Hence

$$\begin{aligned} n_{\nu 0} = n_\nu(\nu_0) &= \frac{n_\gamma}{2\nu_{\mathrm{Ryd}}} \left(\frac{\nu_0}{\nu_{\mathrm{Ryd}}}\right)^{-\frac{3}{2}} \\ &= U n_e \frac{{\nu_{\mathrm{Ryd}}}^{\frac{1}{2}}}{{\nu_0}^{\frac{3}{2}}}. \end{aligned} \tag{3.6}$$

Hence the radiative excitation rate R is given in terms of U

$$R \sim 1.5 \times 10^4 f_{abs} U n_{e10} \nu_{15}^{-\frac{3}{2}}, \tag{3.7}$$

where $\nu_{15} = \nu_0/10^{15}\,\mathrm{s}^{-1}$ and finally

$$C/R \sim 4 \times 10^{-2} T_4^{\frac{1}{2}} U^{-1} \nu_{15}^{\frac{3}{2}} f_{abs}^{-1}. \tag{3.8}$$

Given the ionization parameter $U \sim 10^{-1}$, most permitted lines which have $f_{abs} \sim 1$ satisfy the radiative mixing condition $C/R \ll 1$. Many permitted lines are multiplets and they are not in general resolved in the broad line region of AGN where the typical velocity $\sim 10^4\,\mathrm{km\,s}^{-1}$ exceeds the width that separates the multiplets. We defer the detailed model calculations of the polarization of those lines to Paper III.

When the radiative excitations dominate, we can derive an evolution equation for the ground level, again ignoring stimulated emission. In a steady state

$$\begin{aligned} \frac{d\bar{\rho}_{gg'}}{dt} &= A \int d\Omega M_{ge}(\mathbf{e}_\alpha) \bar{\rho}_{ee'} M_{e'g'}(\mathbf{e}_\alpha) \\ &\quad - \frac{c^2 A}{h\nu^3} \int d\Omega I_{\alpha\alpha'} M_{eg}(\mathbf{e}_\alpha) \rho_{gg'} M_{g'e}(\mathbf{e}_{\alpha'}) \\ &= 0, \end{aligned} \tag{3.9}$$

where no summation is assumed on g and g' in the second term. This equation was combined with equation (2.14) and an iterative solution for $\rho_{gg'}$, $\rho_{ee'}$ was derived. Equations (2.15) (2.18) were then used to derive absorption coefficients and source functions for the radiative mixing case.

We have carried out this procedure for the same transitions investigated in the preceding section, adopting a similar radiation field. Our results are displayed in Figs 3,4. For transitions with angular momentum $J > 1$ the radiative mixing enhances the polarization. In Fig. 4, the absorption coefficients vary with μ, which contrasts with the result for collisional mixing where the absorption coefficients are isotropic and polarization-independent. With the beam-like radiation distribution the net effect of the radiative mixing is to overpopulate sublevels with higher $|g|$ for transitions of $\Delta J = 1$ and sublevels with lower $|g|$ for those of $\Delta J = 0, -1$. $\mu_\parallel/\mu_\perp$ is maximized for the transition $1 \rightarrow 0$ on account of the enhanced population in the $g = 0$ state. In the case $\Delta J = 1$ the emissivity ratio $j_\parallel/j_\perp$ is maximized

at large angular momentum because of the overpopulation in the $e = 0$ state. The absorption coefficient is almost independent of polarization and so the source function behaves like the emissivity. The radiative mixing has no effect on the transitions with $J_g \leq \frac{1}{2}$ and hence the same source functions and absorption coefficients which are isotropic as in the case of collisional mixing.

Fig. 5 shows that a notable change in the emissivity occurs for transitions associated with large angular momenta, but nevertheless the largest polarization is expected in the permitted lines for the transitions $1 \rightarrow 0$ or $1 \rightarrow 1$.

4. Emission and Absorption Coefficients - Magnetic Mixing

There is an additional complication which may be present in a broad emission line cloud in an AGN and this is magnetic field. Magnetic fields of strength $B \gtrsim 1$ G have been invoked in models by Rees(1987) and Emmering *et al.* (1992) in order to account for cloud confinement so that the magnetic stress is comparable with the gas pressure in the emission line clouds. The associated electron cyclotron frequencies $\nu_L \sim 3(B/1\mathrm{G})$ MHz can then exceed the radiative excitation rate so that the ground sublevels can be further re-populated. Magnetic mixing has no influence in the collision-dominated case as the ground sublevels are already equally populated and the Zeeman splitting energy is small compared with the Doppler line width. Magnetic mixing may also be relevant for the excited state density matrix for semi-forbidden transitions with Einstein A coefficients in the range $\sim 1 - 100$ Hz. We consider these two possibilities in turn.

Suppose that an individual ion is prepared in a ground state with a density matrix $\rho_{gg'}$. If the Hamiltonian is denoted H, the state will evolve according to

$$i\hbar \frac{d\rho_{gg'}}{dt} = [H, \rho_{gg'}] \tag{4.1}$$

(*e.g.* Merzbacher 1961). In other words, the condition for the density matrix to remain unchanged is that it commute with the Hamiltonian. Now the effect of a magnetic field will be to break the degeneracy of the ground sublevels. Expand

the density matrix in the basis eigenstates of the magnetic perturbation. The off diagonal elements of the density matrix will evolve and mix at a rate comparable with the Zeeman splitting frequency between the various states. If several periods of this relative precession can occur between excitations (*i.e.* $\nu_L \gg R$ where R is the radiative excitation rate), the off diagonal elements of the mean density matrix will average to zero. The diagonal elements will, by contrast, be unaffected. We therefore treat the strong magnetic mixing limit by expanding the radiation field in eigenstates referred to the magnetic field direction and ignoring all the off diagonal matrix elements $\rho_{gg'}$. Clearly, this makes no difference when the radiation field is axisymmetric with respect to the magnetic field. However, when this symmetry is broken, different source functions and absorption coefficients will result.

We give an illustrative problem in which the radiation field is unpolarized and has a P_2 angular distribution with respect to a symmetry direction oriented perpendicular to the magnetic field. The magnetically modified source functions and absorption cross sections are displayed in Figs. 6,7 respectively. We find that the polarization pattern is similar to the radiative mixing case for the transitions $\Delta J = 1$ only and the direction of the polarization is reversed in the case $\Delta J = -1$ compared to the case without magnetic field. The notable behavior occurs in the transitions $\Delta J = 0$, where the polarization direction changes as μ increases from 0 to 1. The magnetic field breaks the azimuthal symmetry and hence we should no longer expect that polarization is 0 at $\mu = 1$. In particular, the largest degree of polarization is seen at $\mu = 1$ in the transitions $\Delta J = -1$. As explained in the previous section, the transitions with $J_g \leq \frac{1}{2}$ again show the same result as we have obtained in the collisional mixing case without magnetic field.

For comparison we have also considered what happens to the same types of transition when the excited states are magnetically mixed by the same radiation field (*cf.* Fig. 8), while the ground states are collisionally mixed and have uniform occupancy. In this case, the degree of polarization is lower than that of collisional mixing case without magnetic field. The maximum polarization of the magnetic mixing case is 14% at $\mu = 1$ as opposed to 33% at $\mu = 0$ without magnetic mixing.

It is also notable that the polarization increases from zero as μ increases, which clearly shows that the azimuthal symmetry is broken by the magnetic field.

5. Anisotropic Escape Probability

In the examples we have considered so far, the radiation field is considered fixed and we have computed the source functions and absorption coefficients. As a final illustration we show how to compute the emergent polarization when we define an anisotropic, though polarization- and frequency-independent, escape probability. We suppose, for simplicity, that the line photons are *created* isotropically at a rate S_0 per steradian. (As we will describe in the following papers, more complex conditions can arise in the emission line clouds, although the principles are unaffected.) The radiation field will evolve in an escape timescale, which is typically much longer than the time it takes the ions to establish radiative equilibrium. The radiation field will relax to a steady state satisfying

$$(\lambda_{\alpha\alpha'} + \eta_{\alpha\alpha'})I_{\alpha\alpha'} = S_0\delta_{\alpha\alpha'} + j_{\alpha\alpha'} \tag{5.1}$$

subject to the photon conservation condition

$$\int d\Omega \eta_{\alpha\alpha'} I_{\alpha\alpha'} = \int d\Omega j_{\alpha\alpha'}. \tag{5.2}$$

We now suppose for illustration that the escape probability is anisotropic so that a photon emitted with a direction cosine μ with respect to the symmetry axis, has an escape probability (independent of polarization and location),

$$\lambda_{\alpha\alpha'}(\mu) = (1 + k\mu^2)^{-1}\delta_{\alpha\alpha'}, \tag{5.3}$$

where k is the anisotropy parameter. The effective optical depth is measured by one adjustable parameter which can be chosen to be the ratio

$$r = \int d\Omega(S_{0\|} + S_{0\perp}) / \int d\Omega(j_{\|} + j_{\perp}). \tag{5.4}$$

The emergent polarization along a given direction is then a function of k and r. Note that if we were to ignore the scattering, then a P_2 anisotropic radiation field would be established.

We have solved equation (5.1) iteratively, for the radiative mixing case, updating the ground state density matrix at each iteration. We find that ~ 30 iterations are sufficient to achieve convergence depending on r. The angular distribution of the degree of polarization of the escaping radiation

$$P(\mu) = \frac{I_{\|} - I_{\perp}}{I_{\|} + I_{\perp}} \tag{5.5}$$

is exhibited in Fig. 10 for $k = 5$, $r = 4$. A degree of polarization higher than 6% can be achieved for the transitions $J_g = 0 \rightarrow J_e = 1$, $J_g = 1 \rightarrow J_e = 1$ and $J_g = 1 \rightarrow J_e = 0$. For $\Delta J = 1$, there is a clear maximum in the polarization at $\mu = 0$. For $\Delta J = 0$, the polarization is roughly constant for $\mu \lesssim 0.5$ and for $\Delta J = -1$ maximum polarization is seen at $\mu \sim 0.4$. Again small J_g is conducive to high polarization. Similar results are found for $r > 1$. Although this example is artificial, it does demonstrate that a true estimate of the emergent polarization requires that we solve the complete radiative transfer equations.

6. Conclusion

In this paper we have analysed some of the physical effects that might be important in establishing the linear polarization of AGN emission lines. We have computed the polarization dependence of the emission and absorption coefficients in a variety of radiation fields. We have demonstrated that polarization requires there to be an anisotropic radiation field.

In estimating the magnitude of the polarization, we have essentially treated the photons in the Markov approximation. That is to say, we have computed the absorption and emission probabilities assuming that the radiation field is independent of the photon frequency, which, in turn depends upon the past history. This is essentially the hypothesis of complete re-distribution, which as we shall argue

in Paper II, is a poor approximation for polarization calculations as the escaping photons in the wings of the line are significantly more anisotropic than those in the core.

ACKNOWLEDGEMENTS

We thank M. Cohen, R. Emmering, R. Goodrich, J. Miller for helpful discussions. We are very grateful to G. M. Voit for his friendly comments and advice. Support under NASA grant NAGW2372 and NSF grant AST89-17765 is gratefully acknowledged.

REFERENCES

Condon,E.U., Shortley, G.H. 1951. *The Theory of Atomic Spectra*, Cambridge: Cambridge University Press.

Emmering, R.T., Blandford, R.D., Shlosman, I. 1992. *Ap. J.*, **385**, 460.

Goodrich, R.W. 1991. *Publ. Astr. Soc. Pacific*, **103**, 1314.

Hamilton, D.R. 1947. *Ap. J.*, **106**, 457.

Merzbacher, E. 1961. *Quantum Mechanics*, New York: Wiley.

Netzer, H. 1990. *Active Galactic Nuclei*, Berlin: Springer-Verlag.

Osterbrock, D.E. 1989. *Astrophysics of Gaseous Nebulae and Active Galactic Nuclei.*

Osterbrock, D.E., Wallace, R.K. 1977. *Astrophys. Lett.*, **19**, 11.

Rees, M.J. 1987. *MNRAS*, **228**, 47P.

Varshalovich, D.A. 1965. *Sov. Astr.* , **9**, 442.

Webster, A. 1986. *MNRAS*, **217**, 761.

Figure Captions

Figure 1 – The basis vectors of the photon states. $\mathbf{e}_{\|}$ lies in the $\mathbf{k}-\hat{\mathbf{z}}$ plane, where $\mathbf{k}$ is the wave vector of the photon and $\mathbf{e}_{\perp}$ is in the $\hat{\mathbf{x}}-\hat{\mathbf{y}}$ plane.

Figure 2 – The ratio of parallel and perpendicular source functions for collisional mixing case with an unpolarized radiation field $I_{\alpha\alpha'} \propto \mu^2\delta_{\alpha\alpha'}$. J_g is the total angular momentum of the ground state and $J_e = J_g + \Delta J$ is that of the excited state. As the ground sublevels are equally populated the absorption coefficient is independent of the polarization and so the source function behaves like the emissivity. Source functions for permitted values of J_g are plotted as long as the the curves are distinguishable. Different ground states are distinguished by line styles.

Figure 3 – The ratio of source functions for the radiative mixing case under conditions described for Fig 2.

Figure 4 – The ratio of the parallel component of the absorption coefficient $\mu_{\|}$ to the perpendicular component $\mu_{\perp}$ for the radiative mixing case with the same radiation field as Figure 2

Figure 5 – The ratio of emissivities for the radiative mixing case

Figure 6 – The ratio of source functions for the magnetic mixing case. The conditions are constrained to be the same as those described in Fig 2 with the addition of magnetic field along x-axis and the absorption and the emission coefficients are calculated as a function of $\mu = \cos\theta$ where θ is the angle between the $z-$ axis (symmetry axis) and the line of sight keeping $\phi = 0$. See Fig. 2. for identification of J_g.

Figure 7 – The ratio of absorption coefficients for the magnetic mixing case for different transitions. See Fig. 2. for identification of J_g.

Figure 8 – The ratio of source functions for the magnetic mixing case applied to semi-forbidden lines with the same conditions described in Fig. 6. See Fig. 2. for identification of J_g.

Figure 9 – The polarization-independent anisotropic escape probability adopted for the purpose of simple calculation suitable for the geometry of cylindrical clouds and given by the analytic formula $\lambda = 1/(1 + k\mu^2)$ with $k = 5$.

Figure 10 – The polarization from the anisotropic escape probability given in Fig 9. We choose the ratio of scattered photons to the created photons $r = \int d\Omega(j_{\|} + j_{\perp})/\int d\Omega(S_{0\|} + S_{0\perp}) = 4$ and the polarization P is given by $P = (I_{\|} - I_{\perp})/(I_{\|} + I_{\perp})$. See Fig. 2. for identification of J_g.

TABLE 1 Polarization scattered perpendicular to a beam of radiation

$\Delta J \backslash J_e$	0	$\frac{1}{2}$	1	$\frac{3}{2}$	2	$\frac{5}{2}$	3	$J_e = \infty$
1	–	–	1.000	0.429	0.288	0.226	0.191	0.077
0	–	0	0.200	0.261	0.288	0.302	0.310	0.333
-1	0	0	0.008	0.015	0.022	0.027	0.032	0.077

$\Delta J = J_e - J_g$

The polarization for unidirectional radiation distribution in the collisional mixing case.

No electric dipole transitions are allowed for $J_e = 0$ for $\Delta J = 0, 1$.

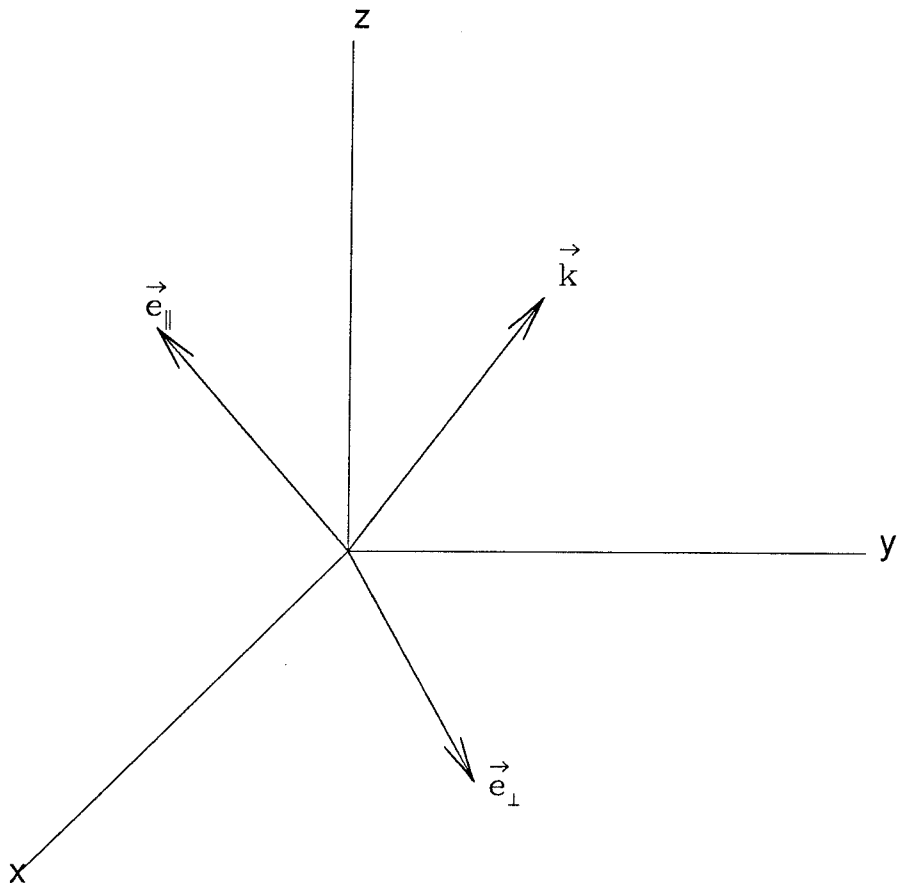

Figure 1

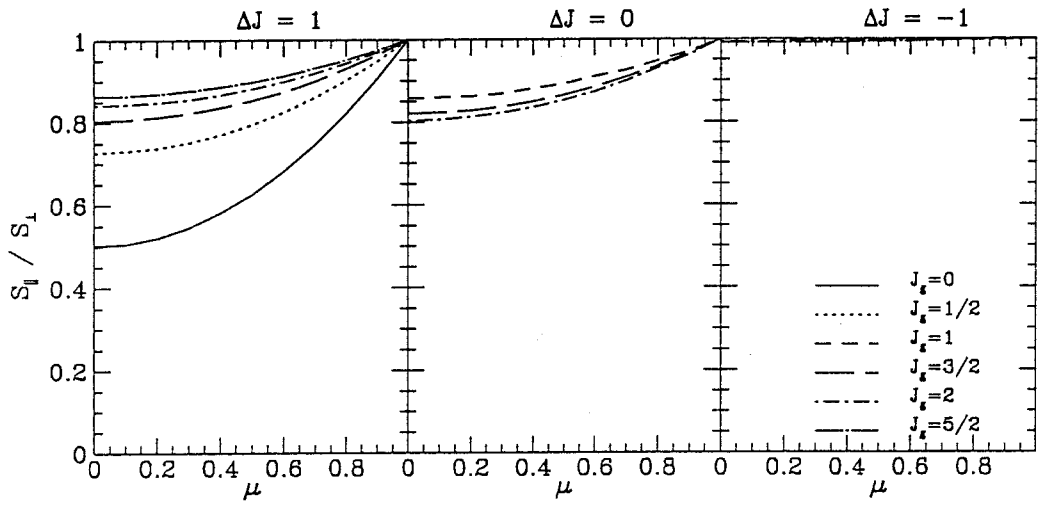

Figure 2

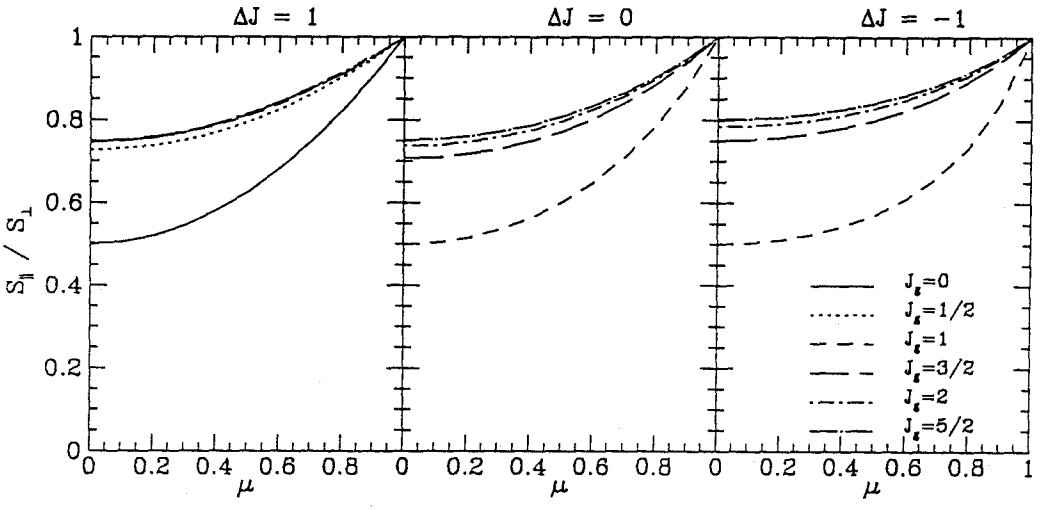

Figure 3

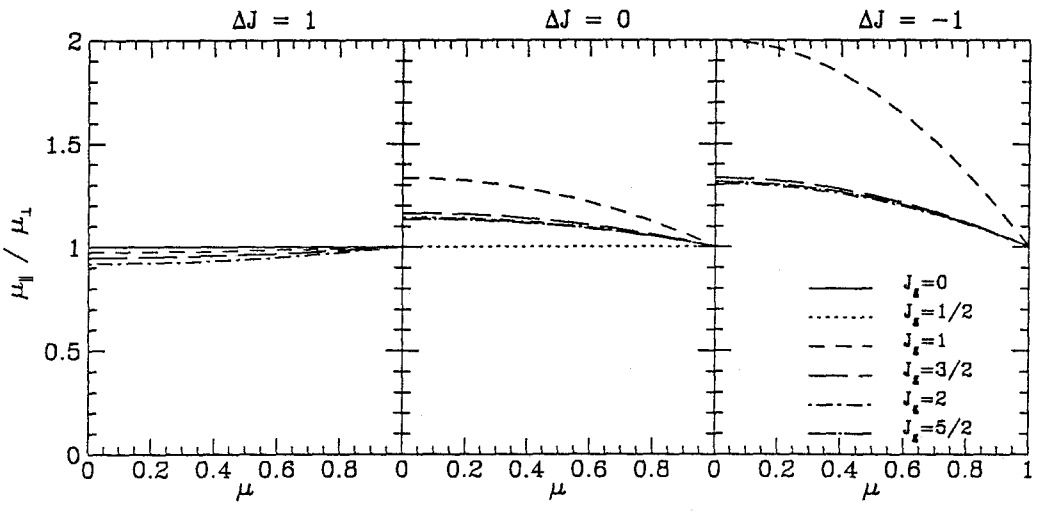

Figure 4

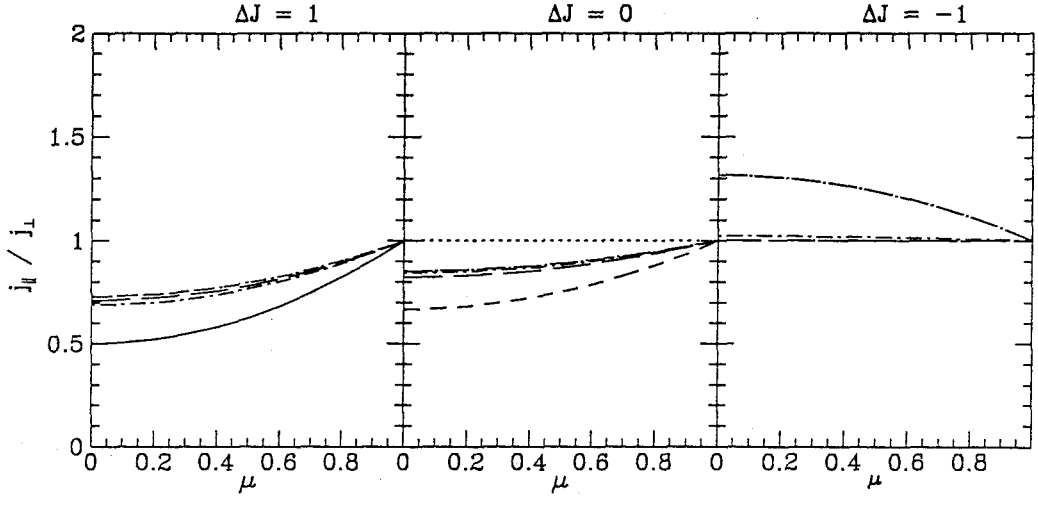

Figure 5

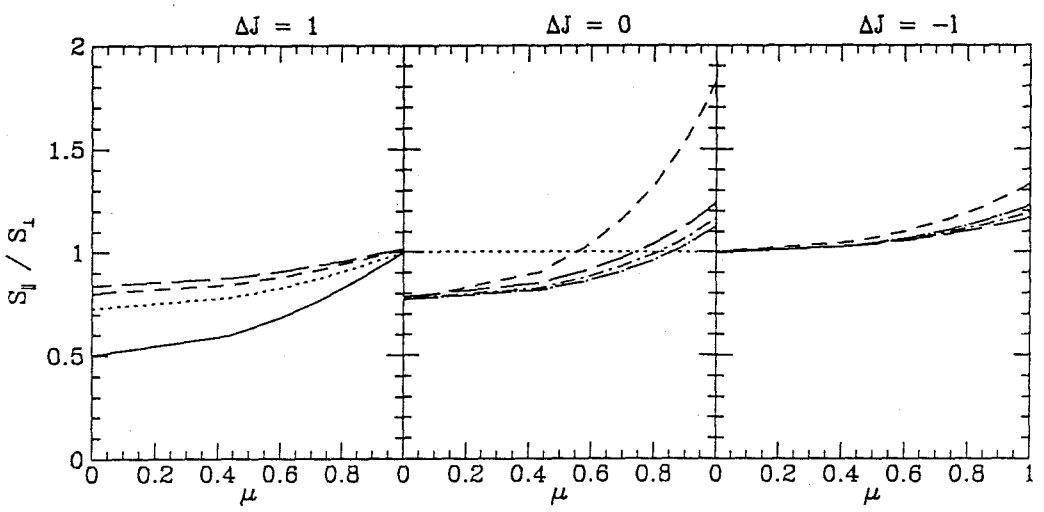

Figure 6

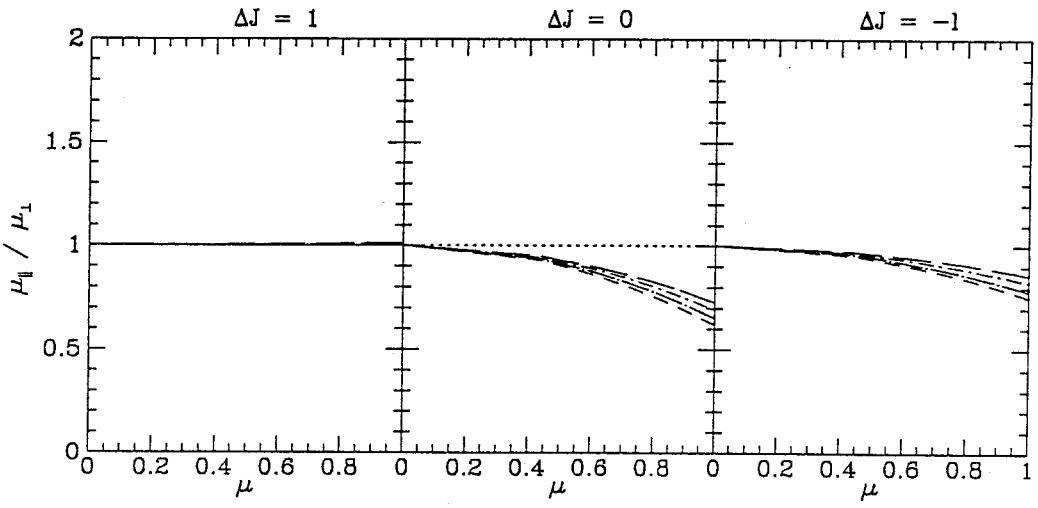
ΔJ = 1
ΔJ = 0
ΔJ = −1
$\mu_{\parallel} / \mu_{\perp}$
2
1.5
1
0.5
0
0 0.2 0.4 0.6 0.8 0 0.2 0.4 0.6 0.8 0 0.2 0.4 0.6 0.8 1
μ
μ
μ

Figure 7

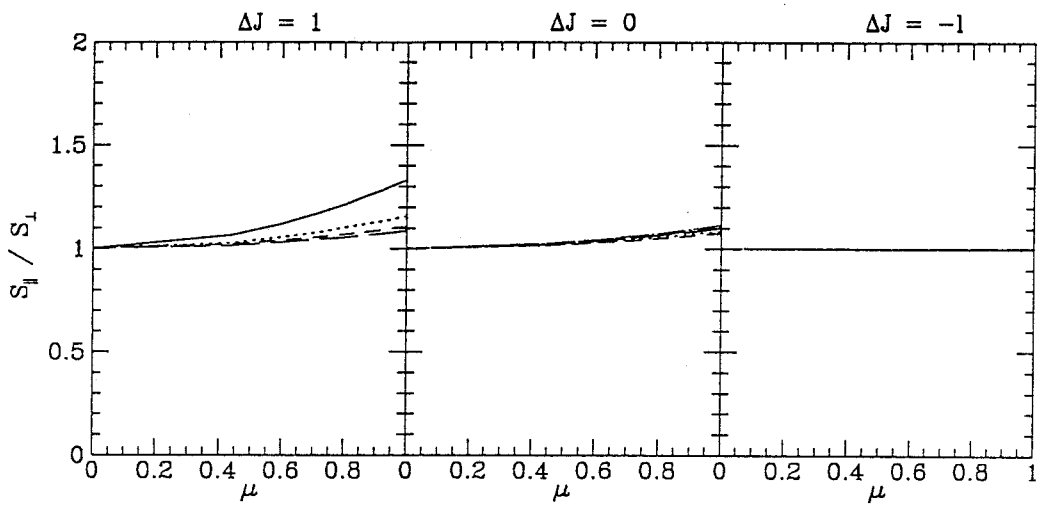
ΔJ = 1
ΔJ = 0
ΔJ = −1
$S_{\parallel} / S_{\perp}$
2
1.5
1
0.5
0
0 0.2 0.4 0.6 0.8
0 0.2 0.4 0.6 0.8
0 0.2 0.4 0.6 0.8 1
μ
μ
μ

Figure 8

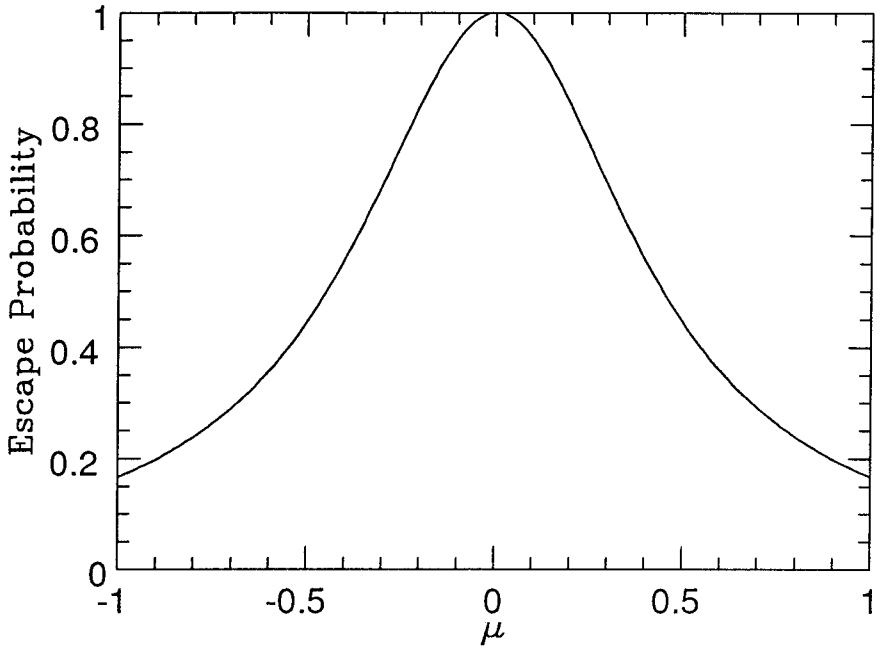

Figure 9

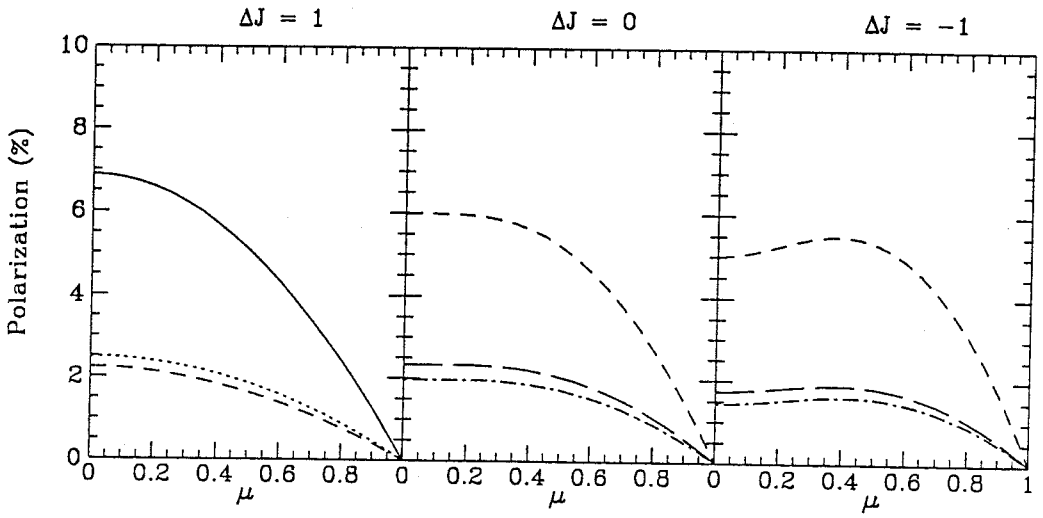
ΔJ = 1
ΔJ = 0
ΔJ = −1
Polarization (%)
10
8
6
4
2
0
0 0.2 0.4 0.6 0.8
0 0.2 0.4 0.6 0.8
0 0.2 0.4 0.6 0.8 1
μ
μ
μ

Figure 10

3

On the Polarization of Resonantly Scattered Emission Lines II. Polarized Emission From Anisotropically Expanding Clouds

H. W. Lee, Caltech, Pasadena, CA 91125.

ABSTRACT

The linear polarization of broad emission lines from anisotropically expanding clouds in active galactic nuclei is calculated using a Monte Carlo method. Both semi-forbidden and permitted lines are considered. We investigate the effect of spatial transport and geometric anisotropy on polarization. It is found that the maximum polarization of 8 percent is obtained from a single stationary oblate cloud and 4 percent from a stationary prolate cloud when the optical depth τ is ~ 1 with large axis ratios, and this condition may be satisfied by some semi-forbidden lines which have the optical depth $\tau \sim 1-10$ (*e. g.* CIII]λ1909). Similar results are obtained from expanding clouds depending on the optical depths and kinematic conditions. The numerical integration over a disk-like configuration of emission clouds shows 4 percent or lower polarization compared to a single cloud or equivalently a jet-like distribution.

1. Introduction

In Paper I of this series we discussed collisional mixing and radiative mixing with and without magnetic field and calculated the polarization from anisotropic radiation field assuming complete redistribution and using the escape probability formalism. We consider the polarization of broad emission lines from active galactic nuclei (AGN).

The broad emission line region (BELR) of AGN is believed to be located within ~ 1 pc of the continuum source and to be composed of clouds with density n_e in the range $\sim 10^8 - 10^{11}\,\mathrm{cm}^{-3}$, sizes $l \sim 10^{12} - 10^{14}\,\mathrm{cm}$ and small filling factors $f \sim 10^{-8}$ (*e. g.* Netzer 1990). The analysis using photoionization models shows that a consistent cloud model of the BELR can be given with high ionization parameter defined by the ratio of the density of hydrogen ionizing photons to the free electron density $U \sim 0.3$ (*e. g.* Peterson 1991). According to the usual classification of AGNs, typical broad lines have Full Width at Half Maximum (FWHM) $\sim 5,000\,\mathrm{km\,s}^{-1}$ and Full Width at Zero Intensity (FWZI) $\sim 20,000\,\mathrm{km\,s}^{-1}$. The line profiles are diagnostics of the complicated velocity fields of the clouds. However, it is still not agreed whether the cloud motions are best described as infall, outflow, orbital motion or random motion.

The time required for sound to cross a cloud is much smaller than the cloud crossing time of the BELR, which implies that the line-emitting clouds must be confined. One possible confining agent is the ram pressure of an optically thin intercloud medium of density less than $10^5\,\mathrm{cm}^{-3}$. Another possibility is magnetic confinement (*e. g.* Rees 1987, Emmering, Blandford & Shlosman 1992).

Polarization observations of spectral lines can also be a good probe of the BELR. It is believed that line photons are emitted by de-excitation following either collisional excitation or recombination. Photons associated with common resonance transitions typically scatter many times before emerging from a cloud. The velocity difference expected between clouds is generally assumed to be large enough to ensure that scattering in more than one cloud does not occur often. The scattering optical depth of a single cloud depends on its size, abundance, oscillator strength, and internal velocity gradients. The emission lines emerging from a single cloud can be polarized if the cloud is either non-spherical or expands anisotropically. In this paper we compute the degree of polarization for specific emission lines expected for some simple models.

In section 2, we describe the atomic physics relevant to the calculation of the degree of polarization from resonance line scattering. In section 3, we present

the result from numerical data of the polarization from a single stationary cloud in the BELR and in section 4, the numerical results from clouds expanding both homologously and nonhomologously are discussed. We then integrate over an axisymmetric ensemble of clouds in section 5 to compute the average polarization. Our results are briefly summarized and the observational prospects are discussed in section 6

In Paper III of this series we will discuss specific application of our results to AGN.

2. Emission Line Polarization

The appropriate tool to use to compute the polarization due to random scatterings by atoms that are not in a pure state is the density matrix. In this section we calculate the expected polarization distribution of resonance line photons being scattered by a single ion or atom(*e. g.* Paper I).

It will be assumed initially that the excitation rate R is much smaller than the collision rate C so that the ground substates are equally populated. We are only concerned with E1 (Electric dipole) transitions which are characterized by the selection rules

$$\begin{aligned} &\Delta S = 0 \\ &\Delta L = 0, \quad \pm 1 \\ &\Delta J = 0, \quad \pm 1 \quad (\text{except} \quad J_e = J_g = 0), \end{aligned} \tag{2.1}$$

where J_e and J_g are the excited and the ground state angular momentum of the ion. According to the Wigner-Eckart theorem (*e. g.* Merzbacher 1961), the transition matrix elements are proportional to Clebsch-Gordan coefficients for addition of angular momentum by one in the case of E1 transition. The tensor operators of rank 1 are defined by

$$\begin{aligned} V^{\pm} &= \mp \frac{1}{2^{\frac{1}{2}}}(x \pm iy) = r\left(\frac{4\pi}{3}\right)^{\frac{1}{2}} Y_1^{\pm 1} \\ V^0 &= z = r\left(\frac{4\pi}{3}\right)^{\frac{1}{2}} Y_1^0. \end{aligned} \tag{2.2}$$

Then the transition matrix elements are

$$< J_e M_e|V^q|J_g m_g >= \frac{1}{2J_g+1} < e|V_q|g >< n_e J_e \parallel V \parallel n_g J_g >, \tag{2.3}$$

where $< e|V_q|g > \equiv < J_g 1 M_g q|J_e M_e > = < 1 J_g J_e M_e|J_g 1 M_g q >$ are Clebsch-Gordan coefficients whose values are given in Paper I (also *e. g.* Condon & Shortley 1951) and the term $< n_e J_e \parallel V \parallel n_g J_g >$ is a reduced matrix element which depends only on the radial part of the entire wavefunction, and hence can be regarded as a proportionality constant.

As in Paper I we choose $\mathbf{e}_\perp \equiv \mathbf{e}_1$ in the x-y plane and $\mathbf{e}_\parallel \equiv \mathbf{e}_2$ in the $\mathbf{k}-\mathbf{z}$ plane for a photon with wavevector $\mathbf{k}$ as the basis states of the two linear polarizations. (See Fig.1.) The density matrix for an ensemble of unpolarized photons is

$$\rho = \begin{pmatrix} 0.5 & 0 \\ 0 & 0.5 \end{pmatrix}. \tag{2.4}$$

In general the imaginary part of the off-diagonal density matrix elements represent circular polarization. However, in this model left- and right-handedness are indistinguishable so that we have

$$\mathrm{Im}(\rho_{12}) = \mathrm{Im}(\rho_{21}) = 0. \tag{2.5}$$

With the assumption of equal population of ground substates the probability of re-emission of a single photon into $d\Omega$ for E1 transition is

$$\begin{aligned} P(\mu,\phi)d\Omega &\propto \sum_j \sum_{j'} \Big| \sum_i < b_j|\mathbf{e}^{in}\cdot\mathbf{r}|a_i >< a_i|\mathbf{e}^{out}\cdot\mathbf{r}|b_{j'} > \Big|^2 d\Omega \\ &\propto \sum_{gg'} \Big| \sum_e M_{eg}(\mathbf{e}^{in}) M_{g'e}(\mathbf{e}^{out}) \Big|^2 d\Omega, \end{aligned} \tag{2.6}$$

where a_i and b_j refer to the upper level substate and the lower level substate respectively and $\mathbf{e}^{in}$ and $\mathbf{e}^{out}$ represent the incoming polarization and the outgoing polarization respectively and the matrix elements $M_{ge}(\mathbf{e}_\alpha)$ are defined as follows;

$$\begin{aligned} M_{eg}(\mathbf{e}_\alpha) &\equiv < a_i|\mathbf{e}_\alpha\cdot\mathbf{r}|b_j > \\ M_{ge}(\mathbf{e}_\alpha) &\equiv M^*_{eg}. \end{aligned} \tag{2.7}$$

Considering an ensemble of incoming photons represented by the density operator ρ, the re-emission probability becomes

$$P(\mathbf{k}_{out}) \propto \sum_{\alpha\alpha'} \sum_{\beta} \sum_{ee'} \sum_{gg'} M_{g'e}(\mathbf{e}_{\beta}^{out}) M_{eg}(\mathbf{e}_{\alpha}) \rho_{\alpha\alpha'} M_{ge'}(\mathbf{e}_{\alpha'}) M_{e'g'}(\mathbf{e}_{\beta}^{out}). \quad (2.8)$$

To incorporate this formalism into numerical calculations we have to compute the density matrix of the scattered photon, which is given by

$$\rho_{\beta\beta'} \propto \sum_{\alpha\alpha'} \sum_{ee'} \sum_{gg'} M_{g'e}(\mathbf{e}_{\beta}) M_{eg}(\mathbf{e}_{\alpha}) \rho_{\alpha\alpha'} M_{ge'}(\mathbf{e}_{\alpha'}) M_{e'g'}(\mathbf{e}_{\beta'}), \quad (2.9)$$

subject to the normalization condition

$$\rho_{11} + \rho_{22} = 1. \quad (2.10)$$

If we write explicitly the re-emission probability for the transition from J_g=0 to J_e=1, the result is given by

$$P(\mu, \phi) \propto 1 + 2\cos^2\theta[\rho_{11}\cos^2\phi + \rho_{22}\sin^2\phi] + 4\rho_{12}\cos\phi\ \sin\phi \quad (2.11)$$

which is consistent with the Rayleigh phase function, when $P(\mu, \phi)$ is averaged for the azimuthal angle ϕ,

$$P_{\text{Rayleigh}}(\mu, \phi) = 3(1 + \cos^2\theta)/8. \quad (2.12)$$

(*e. g.* Chandrasekhar 1960)

Radiative mixing will occur if the collision frequency is much smaller than the radiative excitation rate (*e. g.* Varshalovich, 1965). It does not follow any more that the ground substates are equally populated when the atoms are subject to anisotropic incoming radiation (*e. g.* Paper I). When radiative mixing is introduced, the re-emission probability given in Eq.(2.8) becomes

$$P(\mathbf{k}_{out}) \propto \sum_{\alpha\alpha'\beta} \sum_{ee'} \sum_{gg'g''} M_{g'e}(\mathbf{e}_{\beta}) M_{eg}(\mathbf{e}_{\alpha}) \rho_{\alpha\alpha'} \rho_{jj'} M_{ge'}(\mathbf{e}_{\alpha'}) M_{e'g''}(\mathbf{e}_{\beta}) \quad (2.13)$$

and the density matrix elements of the scattered photon is given by

$$\rho_{\beta\beta'} \propto \sum_{\alpha\alpha'}\sum_{ee'}\sum_{gg'g''} M_{g'e}(\mathbf{e}_\beta)M_{eg}(\mathbf{e}_\alpha)\rho_{\alpha\alpha'}\rho_{gg'}M_{ge'}(\mathbf{e}_{\alpha'})M_{e'g''}(\mathbf{e}_{\beta'}) \qquad (2.14)$$

subject to the normalization condition given in Eq.(2.10). Here, the density matrix elements $\rho_{gg'}$ and $\rho_{ee'}$ associated with the ground and the excited substate populations are given by the simultaneous solutions of the following equations;

$$\rho_{ee'} \propto \sum_{\alpha\alpha' gg'} \int d\Omega I_{\alpha\alpha'} M_{eg}(\mathbf{e}_\alpha)\rho_{gg'}M_{g'e'}(\mathbf{e}_{\alpha'}) \qquad (2.15)$$

$$\sum_{ee'\alpha} \int d\Omega M_{ge}(\mathbf{e}_\alpha)\rho_{ee'}M_{e'g'}(\mathbf{e}_\alpha) \propto \sum_{e\alpha\alpha'} \int d\Omega I_{\alpha\alpha'} M_{eg}(\mathbf{e}_\alpha)\rho_{gg'}M_{g'e}(\mathbf{e}_{\alpha'}) \qquad (2.16)$$

with the normalization conditions $\sum_g \rho_{gg} = 1$ and $\sum_e \rho_{ee} = 1$, where $I_{\alpha\alpha'} \equiv I_{\nu\Omega}\rho_{\alpha\alpha'}$, $I_{\nu\Omega}$ being the intensity. In general the condition for radiative mixing is usually satisfied by permitted lines with $J_g \geq 1$ and for semi-forbidden lines collisional mixing applies. (*e. g.* Paper I)

3. Polarization from Stationary Clouds

We consider initially two prominent emission lines $CIII]\lambda1909$ and $CIV\lambda1549$ and compute the expected degree of polarization for different optical depths and kinematics. We assume that the velocity distribution of the ions is Maxwellian and hence the line profile is given by the Doppler profile function. The optical depth at line center τ_0 of a cloud is given by

$$\tau_0 = \frac{\pi e^2}{m_e c} f_i \frac{c}{\nu_0 v_{th}} \phi(0) N_i, \qquad (3.1)$$

where ν_0 is the frequency at line center, N_i is the ion column density, f_i is the oscillator strength and $\phi(x) = \frac{1}{\sqrt{2\pi}} \exp(-x^2/2)$ is the Doppler profile function expressed in terms of fractional frequency shift

$$x = \frac{(\nu - \nu_0)}{\nu_0} \frac{c}{v_{th}}. \qquad (3.2)$$

This is numerically

$$\tau_0 = 1.16 \times 10^{-14} \lambda_0 \sqrt{A/T} f_i N_i, \tag{3.3}$$

where λ_0 is the line center wavelength in Å, T in K, and A is the atomic weight for the atom(*e. g.* Rybicki & Lightman 1979). With the values of electron density $n_e = 10^{10}\,\mathrm{cm}^{-3}$ and the temperature $T = 10^4\,\mathrm{K}$ the typical optical depth of a cloud is $\tau_0 \sim 10$ for $CIII]\lambda1909$ at line center and $\tau_0 \sim 10^6$ for $CIV\lambda1549$ assuming a cloud has typical dimension $l \sim 10^{13}\,\mathrm{cm}$ and the cosmic abundance. The table 1 shows the optical depth at line center for several prominent broad lines in AGN (*e. g.* Netzer 1990). Clouds are parametrized by the optical depth at line center along the symmetry axis τ_c and the axis ratio $r = \tau_c/\tau_a$ where τ_a is the optical depth at line center along the equatorial direction.

The line photons originate from collisional excitation from the ground state. And we assume that the densities of both the electron and the ions are constant inside a cloud, so that the photons are generated uniformly throughout the cloud. The emergent polarization is calculated using a Monte Carlo simulation by tracing photons scattering at random subject to the above cross sections until they escape the cloud and computing the density matrix. Since we are dealing with resonance line scattering, we ignore the natural line broadening so that the velocity component of the emitting ion along the photon propagation direction should equal that of the absorbing ion.

In order to keep track of a photon in the simulation, it is necessary to have the velocity component v of the emitting ion along the wave vector and the distance d before being scattered by another ion. It is noted that the ion velocity v is regarded as the fractional frequency shift x defined in Eq.(3.2) in units of the thermal velocity v_{th}. Since it is assumed that the ion velocity is governed by a Maxwellian distribution

$$P_M(v) = \frac{1}{\sqrt{2\pi}} \exp\left(-v^2/2\right), \tag{3.4}$$

the cumulative probability from $-\infty$ to v is given by

$$\begin{aligned} P_c(v) &= \int_{-\infty}^{v} \frac{1}{\sqrt{2\pi}} e^{-\frac{1}{2}v'^2} dv' \\ &= \frac{1}{2} + \mathrm{erf}(v/\sqrt{2}). \end{aligned} \tag{3.5}$$

Hence by generating a random number P_{ran} ranging 0 and 1 and identifying it as $P_c(v)$, the ion velocity v is obtained by inverting Eq.(3.5), *i. e.* ,

$$v = \sqrt{2}\,\mathrm{erf}^{-1}\left(P_{ran} - \frac{1}{2}\right), \tag{3.6}$$

where the inverse error function is calculated numerically. Hence the optical depth τ_ν is

$$\tau_\nu = \tau_0 \exp(-v^2/2). \tag{3.7}$$

On the other hand, the probability of the photon traveling no more than an optical depth τ_ν is given by

$$P_d(\tau_\nu) = 1 - \exp(-\tau_\nu). \tag{3.8}$$

Hence another random number P'_{ran} also ranging 0 and 1 gives the optical depth τ_ν the photon travels by

$$\tau_\nu = -\ln(1 - P'_{ran}). \tag{3.9}$$

Therefore by combining Eq.(3.7), and Eq.(3.9) the distance d the photon travels before being scattered is given in units of the line center optical depth τ_0 by

$$d = -\ln(1 - P'_{ran})\ \exp(v^2/2). \tag{3.10}$$

Noting that $1 - P'_{ran}$ has the same distribution as P'_{ran}, Eq.(3.10) can be rewritten as

$$d = -\ln P'_{ran}\ \exp(v^2/2). \tag{3.11}$$

We make use of the subroutine 'RAN2' provided by Press *et al.* (1992) to generate random numbers P_{ran} between 0 and 1.

If $d \leq \tau_b$, where τ_b is the line center optical depth to the boundary of the cloud in the photon propagation direction, the photon is regarded as scattered after

traveling a distance d and there we determine the new direction $\hat{\mathbf{k}}_r$ using Eq.(2.13) by rejection method and use Eq.(2.14) to compute the density matrix associated with the re-emitted photon. The frequency of the new photon is determined from the resonance condition and the Maxwellian distribution of the ions with an assumption that the photon momentum is negligible in the scattering process. The velocity of the re-emitting ion is then

$$\mathbf{v}_r = v_i^{\parallel}(\hat{\mathbf{k}}_r \cdot \hat{\mathbf{k}}_i)\hat{\mathbf{k}}_i + v_{ran}(\hat{\mathbf{k}}_\perp \cdot \hat{\mathbf{k}}_r)\hat{\mathbf{k}}_\perp \tag{3.12}$$

where $\hat{\mathbf{k}}_i$ is the propagation direction of the incoming photon, $\hat{\mathbf{k}}_\perp$ is the unit vector lying in the scattering plane perpendicular to $\hat{\mathbf{k}}_i$ given by $\hat{\mathbf{k}}_\perp = \frac{\hat{\mathbf{k}}_r - (\hat{\mathbf{k}}_r \cdot \hat{\mathbf{k}}_i)\hat{\mathbf{k}}_i}{|\hat{\mathbf{k}}_r \times \hat{\mathbf{k}}_i|}$ and v_{ran} is obtained by the same procedure as the step described by Eq.(3.4). With these new values of the wave vector, the position, and density matrix the whole procedure is repeated until the photon escapes the cloud.

If $d > \tau_b$, then the emergent photons are collected in bins of $\Delta\mu \equiv \Delta \cos\theta = 0.1$ where θ is the angle between the symmetry axis of the cloud and the line of sight. The typical number N of photons generated in this numerical calculation for each cloud is 800,000. The standard deviation σ of the polarization of photons in the $\Delta M = 0.1$ mesh is calculated for each simulation and is found to be proportional to $1/\sqrt{N}$ with the typical value of 2.0×10^{-3} when $N \sim 800,000$.

The code has been checked by computing the polarization expected from a region with the anisotropic escape probability

$$\lambda_{\alpha\alpha'} = (1 + k\mu^2)^{-1}\delta_{\alpha\alpha'}, \tag{3.13}$$

and comparing the results with those given in Paper I when $k = 5$. The result is shown in Fig. 2 for the transitions $J_g = 0 \rightarrow J_e = 1$, $J_g = 1 \rightarrow J_e = 0$, and $J_g = 1 \rightarrow J_e = 0$ which are the 3 transitions giving the highest degree of polarization. Note that $\Delta J \equiv J_e - J_g$ in the figure and that the transitions $\Delta J = 0, -1$ are radiative mixing case. The numerical data from the Monte Carlo calculation are shown with 1-σ error bars and the continuous lines are the analytical results from Paper I. The agreement between the two calculations is very good within 1-σ.

Fig. 3 shows the polarization as a function of $\mu = \cos\theta$ from a single cloud with $\tau_a = 10$ and $\tau_c = 1$ for the transitions $J_g = 0 \rightarrow J_e = 1$ and $J_g = \frac{1}{2} \rightarrow J_e = \frac{3}{2}$. By symmetry no polarization is expected at $\mu = 0$ which is well illustrated in the figure for both transitions, and can be also a measure of accuracy of this numerical simulation. The fitting curve is given by

$$f(\mu) = \frac{p_0(1-\mu)}{1-0.67\mu}, \tag{3.14}$$

where p_0 is the maximum polarization for photons emerging perpendicularly to the symmetry axis dependent on the transitions and the geometry of clouds. We note that with the same geometry the ratio of p_0 for the transition $J_g = \frac{1}{2} \rightarrow J_e = \frac{3}{2}$ to that for $J_g = 0 \rightarrow J_e = 1$ is 0.38. As shown in Paper I, it is a general behavior that the highest polarization is obtained in the transitions with the smallest angular momenta. Throughout this section the discussion will be concentrated on the polarization behavior for the transition $J_g = 0 \rightarrow J_e = 1$ only.

For both prolate and oblate spheroidal clouds with the ratio $r = 2$ (for prolate spheroids) and $r = 0.5$ (for oblate spheroids), the polarization p_0 of photons emerging perpendicularly to the symmetry axis is shown in Figs.4 a,b for various optical depths. In the case of the prolate (oblate) spheroids with low optical depths the electric vectors tend to become perpendicular (parallel) to the scattering plane so that we have polarization perpendicular (parallel) to z-axis. The polarization p_0 can be approximated by

$$p_0 = \frac{0.4\ (1-r)^2\tau_0}{(1-r)(\tau_0+1.1)^2+2r}, \tag{3.15}$$

for oblate spheroids ($r \leq 1$) and

$$p_0 = \frac{0.4\ (r-1)^2\tau_0}{r(r-1)(\tau_0+1.8)^2+2r}, \tag{3.16}$$

for prolate spheroids ($r \geq 1$), where τ_0 is the optical depth along the semi-minor axis in both cases. As $r \rightarrow 0$ the maximum polarization of ~ 8 percent at $\tau_0 \sim 1.1$ is obtained and in the opposite limit $r \rightarrow \infty$ it is ~ 5 percent at $\tau_0 \sim 1.8$.

Considering that the CIII zone is smaller than the whole cloud, the optical depth of CIII]λ1909 given in Table 1 can be an overestimate and the condition for the maximum polarization may be met in some AGN.

It is found that for both prolate and oblate spheroidal clouds the largest polarization is obtained when the semi-minor axis has the optical depth ~ 1, which implies that the mean number of scatterings of a photon before escaping the scattering region is approximately 1. The reason for the polarization vanishing in the limit $\tau \to \infty$ is that the photons escape the cloud preferentially by diffusing in frequency rather than in space. That is to say, a photon inside the cloud scatters locally until it is emitted sufficiently far into the wings of the line that the cloud becomes transparent. The emergent polarization would be expected to reflect that variation in intensity across a mean free path in the middle of the cloud rather than at its surface. This accounts for the scaling $P \propto \tau^{-1}$ as $\tau \to \infty$. From this argument it is expected that the polarization of most permitted lines including CIVλ1549 with the optical depth $\tau_0 \gtrsim 10^5$ will be negligible.

Fig.5 shows the polarization from oblate clouds for fixed semimajor axis and various semimajor axes. A maximum polarization of $\sim 8\%$ is attained with extreme ratio $r = \frac{\tau_c}{\tau_a} \lesssim 0.1$ and small semi-minor axis around $\tau_c \sim 1$, which is the same conclusion that the mean scattering number is about 1 as before. If the semi-minor axis $\tau_c \gtrsim 6$ then the polarization from a single stationary cloud is less than 4% for any value of r. Hence the polarization is a sensitive function of the semi-minor axis up to $\tau \sim 6$ when the ratio $r = \tau_c/\tau_a \leq 0.1$.

The finite slab geometry is regarded as the limit of oblate spheroids where the ratio $r = \frac{\tau_c}{\tau_a} \to 0$ and maximum 8% of polarization is obtained with $\tau_c \sim 1$ and no polarization with $\tau_c \gtrsim 10$. For this finite slab geometry classical result is available in the case of electron scattering and has been checked as a test of the code. The code modified for electron scattering reproduced the same result with those obtained by Phillips & Mészáros (1986) using the Feautrier method and iteration scheme applied to finite slab geometry and semi-infinite slab. Comparing with the polarization expected from electron scattering, we see that the behavior at the

low optical depth $\tau_c \lesssim 3$ is similar but at large optical depth $\tau_c \gtrsim 6$ the result from electron scattering shows maximum 11.7% which is highly contrasted with the null result from resonance line scattering (*e. g.* Angel 1969, Chandrasekhar 1946, Phillips & Mészáros 1986). Furthermore in the electron scattering case the direction of polarization is reversed as the thickness of slab increases from zero to infinity, whereas the polarization from resonantly scattered photons does not show such behavior. The different behavior at the large optical depth case $\tau_c \gtrsim 6$ is explained by the high frequency shift of photons in the case of resonance line scattering which makes the region effectively optically thin.

4. Expanding Clouds

We know that clouds move with speed $V \sim 10,000\,\mathrm{km\,s^{-1}}$ and Mach number $M \sim 1000$ with respect to their internal sound speeds. They must be both accelerated and confined, and however this is accomplished (through a combination of thermal, radiative and magnetic stress), it is quite likely that there would be internal velocity gradients within discrete clouds. The model adopted in this section is that each cloud has a linear velocity gradient. Both homologous and nonhomologous expansion is considered. Two additional parameters are introduced in addition to the two parameters (τ_c, r) that characterize a stationary cloud. We choose these to be Δv_c and Δv_a, where $\Delta v_{c,a}$ is the relative velocity of the cloud surface along the symmetry, equatorial directions with respect to the center of the cloud divided by the thermal velocity. The clouds are treated as isothermal and the density of ions is assumed to be constant under expansion both with shear and without shear.

Introducing velocity gradients to the spheroidal region the velocity of an ion becomes

$$\mathbf{v}(x,y,z) = \mathbf{v}_{ran} + \mathbf{v}_b(x,y,z) \tag{4.1}$$

where $\mathbf{v}_{ran}$ has the 3-dimensional Maxwellian distribution and $\mathbf{v}_b(x,y,z) = \frac{dv_x}{dx} x\hat{x} +$

$\frac{dv_y}{dy} y\hat{y} + \frac{dv_z}{dz} z\hat{z}$ is the bulk velocity field. Hence Eq.(3.7) becomes

$$\tau_\nu = \int_{(x_i,y_i,z_i)}^{(x_r,y_r,z_r)} ds \exp\{-[v_i - v_k(x,y,z)]^2/2\}, \tag{4.2}$$

where $v_k(x,y,z) = \hat{k}_1 \frac{dv_x}{dx} x + \hat{k}_2 \frac{dv_y}{dy} y + \hat{k}_3 \frac{dv_z}{dz} z$ and s measures the distance from the position (x_i, y_i, z_i) of the emitting ion to the the position (x_r, y_r, z_r) of the absorbing ion. If we assume that the velocity gradients are constant, then the photon traveling distance d is given by

$$\begin{aligned} d &= \int_{(x_i,y_i,z_i)}^{(x_r,y_r,z_r)} ds \\ &= \frac{1}{B}\left[A - \sqrt{2}\,\mathrm{erf}^{-1}\left\{\mathrm{erf}\left(\frac{A}{\sqrt{2}}\right) - \frac{\sqrt{2}B\tau_\nu}{\sqrt{\pi}}\right\}\right], \end{aligned} \tag{4.3}$$

where $A = v_i - v_k(x_i, y_i, z_i)$ and $B = \hat{k}_1^2 \frac{dv_x}{dx} + \hat{k}_2^2 \frac{dv_y}{dy} + \hat{k}_3^2 \frac{dv_z}{dz}$. The Eq.(4.3) reduces to Eq.(3.11) in the limit $B \to 0$, when the system becomes stationary. We choose the range of the internal velocity differences $\Delta v = v_{\text{edge}} - v_{\text{center}}$ to be from 1 to τ_0. We can also consider contracting clouds by setting $dv_i/dx_i < 0$ for $i = x, y, z$, and the same polarization is obtained as in the case, where the clouds are expanding. The mean free path is $\lambda \sim l/\tau_0$ and hence the distance a photon traveled by random walk process after $\sim \tau_0$ scatterings is $\sim \lambda {\tau_0}^{\frac{1}{2}}$. Therefore the expansion must be included when

$$\Delta v/{\tau_0}^{\frac{1}{2}} \geq v_{th}. \tag{4.4}$$

4.1 Isotropic, Shear-free Expansion of Spheroidal Clouds

By the isotropic, shear-free expansion we mean all the internal velocity differences are equal

$$\Delta v_c = \Delta v_a. \tag{4.5}$$

Figs.6 a,b show the degree of polarization from both prolate and oblate spheroidal clouds expanding isotropically as a function of velocity difference Δv. The polarization is taken as negative when the electric vector is perpendicular to the $z-$axis

(the symmetry axis), and the positive polarization indicates that the electric vector lies in the plane spanned by the wave vector $\mathbf{k}$ and $z-$axis. The polarization increases until the mean number of scatterings is reduced to ~ 1. For $\tau_c = 20$, $\tau_a = 10$ the maximum polarization is $\sim 3\%$ when $\Delta v = 12 v_{th}$. The maximum polarization of $\sim 4\%$ also occurs at $\Delta v = 12 v_{th}$ in the case of oblate clouds with $\tau_a = 20$, $\tau_c = 10$. These maximum values are coincident with those obtained in the stationary clouds with the same axis ratio. As $\Delta v \to \infty$ the polarization decreases, which is expected from the optically thin limit of stationary clouds. Therefore there exists a velocity difference Δv which produces the maximum polarization. We find that this does not exceed 10%, the maximum polarization we obtained in the case of stationary clouds.

We also consider the polarization from clouds with optical depth $\tau \gtrsim 10^5$ suffering supersonic expansion, the result being shown in Fig.6b. The Monte Carlo calculation is not an efficient method for this case unless the internal velocity difference $\Delta v \gtrsim 1000$, when the mean number of scatterings is reduced to ~ 100. A polarization in excess of 3% is shown only when $\Delta v \gtrsim 10^4$, which is unrealistically large for the velocity difference inside an expanding cloud. It is not clear whether the polarization goes to zero in the limit $\Delta v \to 0$. However, from the limiting behavior of stationary clouds in the previous section, we may conclude that there is no polarization from the slowly expanding clouds with $\tau \gtrsim 10^2$.

4.2 Anisotropic Expansion of Spherical Clouds

The anisotropic velocity fields introduce into a spherical cloud the natural specific direction with respect to which some linear polarization is expected. Two different spherical clouds are chosen, namely $\tau_0 = 10$ and $\tau_0 = 10^5$, where the ratio of the internal velocity differences $r_v \equiv \Delta v_x / \Delta v_z$ is either 2 or 0.5. (We assume that there is azimuthal symmetry that $\Delta v_x = \Delta v_y$ for simplicity.) Figs.7 show the numerical result as a function of Δv_x and Δv_z. We use the same sign convention. The decrease in the mean number of scatterings before escaping the cloud shows the dominant role of reduction of effective optical depth played by the velocity

gradients. Hence we have a negative polarization for $r_v \equiv \Delta v_z/\Delta v_x = 2$, which is the same polarization direction as we obtained from a stationary oblate spheroid.

The degree of polarization increases upto $\sim 3\%$ as the internal velocity difference Δv approaches τ_0 from zero (or equivalently until the mean number of scatterings is reduced to ~ 1), τ_0 being the line center optical depth of a spherical cloud in both spherical clouds. However, again it should be emphasized that the internal velocity differences must be unrealistically large to get appreciable polarization in the case of the spherical clouds with the optical depth $\tau_0 \sim 10^5$.

It is also found that the flux distribution as a function of $\mu = \cos\theta$ is different where θ is the angle between the symmetry axis and the line of sight. The flux distribution is almost constant in the case of the sphere with lower optical depth $\tau_0 \sim 10$, whereas 2 times more photons escape along the direction of the largest Δv in the case of sphere of $\tau_0 \sim 10^5$ when $\Delta v \gtrsim \tau_0/10$.

4.3 Nonhomologous Expansion

It is possible to make various models of clouds expanding nonhomologously. The simplest example can be the expanding clouds having the same velocity gradients ($\frac{dv_x}{dx} = \frac{dv_y}{dy} = \frac{dv_z}{dz}$) with anisotropic geometry such as prolate or oblate spheroids. Fig.8a shows the degree of polarization from a single prolate spheroid with $\tau_a = 5$ and $\tau_c = 20$ expanding nonhomologously satisfying the above condition. Since the velocity gradients $\frac{dv_i}{dx_i}, i = x, y, z$ are chosen to be equal, the internal velocity difference along z-axis is larger than that along other directions $\Delta v_z > \Delta v_x = \Delta v_y$. Therefore the effect of reducing the optical depth by velocity gradients is dominant along the z direction and hence the polarization is reduced compared with the stationary cloud with the same geometry. We see almost linear relations between the number of scatterings, the degree of polarization and internal velocity difference.

In Fig.8b we show another example for optically thick clouds with $\tau_c = 10^5$ and $\tau_a = 2\tau_c$. Here we adopt the velocity field so that $\Delta v_a = 4\Delta v_c$ and hence the effective optical depth is much smaller in the equatorial direction than in the

polar direction giving more polarization as Δv increases. Hence the direction of the polarization is the same as in the case of a stationary prolate cloud, which we took as negative in the previous discussion of expanding spherical clouds. As in the previous subsections, the notable polarization shows up when $\Delta v \sim 10^4$ corresponding to the scattering number of ~ 40, and around $\Delta v = 3 \times 10^4$ there is a maximum polarization of 3% with the scattering number of ~ 1.

5. Disk-like Distribution of Emission Clouds

So far we have considered the expected polarization from a single cloud in the BELR. The global distribution of line emitting clouds in the BELR is still not known. Various models of the BELR are suggested including spherical, disk-like and jet-like distribution. No polarization is expected from spherical distribution because there is no preferred direction. the degree of polarization from a jet-like distribution is equal to that from a single cloud with the simple assumption that each cloud composing the jet has the same geometry and dynamical conditions. In this section we consider the polarization from the disk-like distribution.

Figs.9 a,b show the polarization from a disk-like distribution of stationary spheroidal clouds with the symmetry axis arranged to point the center of the disk as a function of μ, the cosine of the angle between the normal vector of the disk and the line of sight. The fitting curve is given by Eq.(3.14) with $p_0 = 0.015$ for both disks. It is remarkable that the two disk-like distributions show the same polarization dependence on μ whereas the component clouds have different polarization behaviors. The fitting is not good at lower μ because of the numerical integration of the data which includes the statistical noise from Monte Carlo simulations.

The maximum polarization with the same axis ratio is shown in Figs.10 a,b as a function of various optical depths of component clouds. The data are fitted by Eqs.(3.15, 3.16) with different peak values. Compared with the single cloud case (or equivalently jet-like distribution case) the polarization from the disk-like distribution is lower. When the component clouds are oblate (see Fig.10 a), the maximum polarization in the disk-like distribution is the half of that in the single

cloud (or equivalently in the jet-like distribution), and on the other hand when the disk is composed of prolate clouds the ratio is 0.63.

In the disk-like distribution the maximum polarization from oblate clouds is almost the same as that from prolate clouds, whereas the result is quite different in the jet-like distribution case, the polarization from oblate clouds being greater than that from prolate ones. It is noted that both Fig. 10 a,b can be fitted by either curve nicely. This point is clear when we consider the polarization as in Figs 9 a,b, where the behavior is similar as a function of μ. can be fitted nicely. This difference between the two distributions is due to the fact that the emergent line photons from a single prolate spheroid have different flux distribution as a function of μ from those from an oblate one, that is, in the case of a single prolate cloud we have twice as many photons in the equatorial direction than in the polar direction and from an oblate cloud the opposite is true. Hence in the disk of oblate clouds a smaller number of photons with higher polarization give almost the same degree of linear polarization as we have from more photons with lower polarization from the disk of prolate clouds.

6. Discussion

The results obtained in the previous sections can be summarized as follows:

1. The dominant factor for maximum polarization is the mean number of scatterings before emerging from a cloud if the anisotropy conditions are fixed by other parameters such as geometry or kinematics, because scatterings isotropize the radiation field. The largest polarization condition is found to be $n \sim 1$ where n is the mean number of scatterings, and is of order the line center optical depth τ_0 when the cloud is stationary.

2. The maximum polarization from a single stationary oblate cloud is about twice as large as that from a prolate one with the same axis ratio. In the extreme case ($r \to 0$ finite slab case) the largest polarization is ~ 8 percent when the thickness of the slab is $\tau_0 \sim 2$ and for infinite cylinder case ($r \to \infty$) it is ~ 4 percent when the radius of the cylinder is $\tau_0 \sim 2$. These conditions for a large polarization can

be satisfied by some semi-forbidden lines (*e. g.* CIII]λ1909) from AGN. As the optical depth $\tau_0 \to \infty$, the polarization $P \propto \tau_0^{-1}$. Hence most permitted lines such as CIVλ 1549 having the optical depth $\gtrsim 10^5$ will not be polarized enough for measurement.

3. The effect of spatial transport is important only when the internal velocity difference is large compared to the thermal velocity in the optically thick case given in Eq(4.4). Hence for the permitted lines in the BELR for which the optical depth $\tau_0 \sim 10^6$ the polarization is expected to be very small unless the clouds are suffering supersonic expansion with $\Delta v \gtrsim 1000 v_{th}$. For the semi-forbidden lines with moderate optical depth $\tau_0 \sim 10$ spatial transport should be considered to calculate the polarization. Various models can be constructed for expanding clouds, including homologous and nonhomologous models.

4. The polarization from a disk-like distribution is smaller than from a jet-like distribution in general. In particular the polarization from a disk-like distribution of stationary prolate clouds is the same as that from a disk of stationary oblate clouds with the same axis ratio. This behavior can be explained by the difference of flux distribution from a single spheroidal cloud.

As we discussed in Paper I, a small magnetic field of $\gtrsim 0.01$G can specify the direction we can identify as the quantization axis different from the symmetry axis of the clouds, and therefore the behavior of the polarization as a function of the angle between the line of sight and the symmetry axis is altered notably still giving almost the same maximum polarization as in the case without magnetic field. In this paper we omit the magnetic case without loss of much generality emphasizing that the magnetic field can be incorporated without much difficulty which is equivalent to a new choice of the quantization axis.

The emerging resonance line photons from the region of line center optical depth $\tau_0 \geq 10^4$ are usually frequency-shifted through random walk process in the frequency space before escaping the region and hence it is believed that the scattering is local. The typical τ_0 is of order 10^6 for permitted lines in the BELR so that most emerging photons are in the wings of the Doppler profile. The diffusion

in frequency space distinguishes the behavior of the polarization of resonantly scattered photons from the polarization behavior of photons scattered by free electrons, which was studied by Chandrasekhar in the case of semi-infinite slab.

ACKNOWLEDGEMENTS

This research was motivated by the work of L. Western, and I am very grateful to him. I am also very grateful to R. D. Blandford for his helpful discussion and advice. I wish to thank G. M. Voit and R. Emmering for their useful discussion and comments. I thank M. Cohen and R. Goodrich for useful discussions.

REFERENCES

Angel, J.R.P. 1969. *Ap. J.*, **158**, 219.

Chandrasekhar, S. 1946. *Ap. J.*, **103**, 351.

Chandrasekhar, S. 1960. Radiative Transfer (New York: Dover Publications).

Emmering, R.T., Blandford, R.D., & Shlosman, I. 1992. *Ap. J.*, **385**, 460.

Netzer, H. 1990. *Active Galactic Nuclei*, Berlin: Springer-Verlag.

Osterbrock, D.E. & Wallace, R.K. 1977. *Astrophys. Lett.*, **19**, 11.

Peterson, B.M. *et al.* 1991. *Ap. J.*, **368**, 119.

Phillips, K.C. & Mészáros, P. 1986. *Ap. J.*, **310**, 284.

Press, W. *et al.* 1992. Numerical Recipes in Fortran (Cambridge [England]: Cambridge University Press).

Rees, M.J. 1987. *MNRAS*, **228**, 47P.

Rybicki, G.B. & Lightman, A.P. 1979. Radiative Processes in Astrophysics (Wiley-Interscience).

Sakurai, J.J. 1985. Modern Quantum Mechanics (The Benjamin/Cummings).

Varshalovich, D.A. 1965. *Sov. Astr.* , **9**, 442.

FIGURE CAPTIONS

Figure 1 – The basis vectors of the two linear polarizations. $\mathbf{k}$ is the wave vector and the polarization is measured along $\mathbf{e}_1$ in the $x-y$ plane and and $\mathbf{e}_2$ in the plane spanned by $\mathbf{k}$ and $\mathbf{z}$.

Figure 2 – Polarization from the anisotropic escape probability $\lambda_{\alpha\alpha'}(\mu) = (1 + k\mu^2)^{-1}\delta_{\alpha\alpha'}$ with $k = 5$. The continuous lines are the solutions obtained in Paper I by numerical iteration (*e. g.* Fig. 10 of Paper I). The data from the Monte Carlo calculations are shown by crosses with 1-σ error bars. The transitions represented in the figure are $J_g = 0 \rightarrow J_e = 1$, $J_g = 1 \rightarrow J_e = 1$, and $J_g = 1 \rightarrow J_e = 0$. ($\Delta J \equiv J_e - J_g$)

Figure 3 – The polarization from a single stationary cloud with $\tau_a = 10$ and $\tau_c = 1$ as a function of $\mu = \cos\theta$ for the transitions $J_g = 0 \rightarrow J_e = 1$ and $J_g = \frac{1}{2} \rightarrow J_e = \frac{3}{2}$. The fitting curve is given by $f(\mu) = \frac{p_0(1-\mu)}{1-0.67\mu}$, where $p_0 = 0.084$ for $J_g = 0 \rightarrow J_e = 1$ and $p_0 = 0.035$ for $J_g = \frac{1}{2} \rightarrow J_e = \frac{3}{2}$. The data are fitted by $f(\mu) = \frac{p_0(1-\mu)}{1-0.67\mu}$ with $p_0 = 0.084$ and $p_0 = 0.031$.

Figures 4a,b – The polarization from a single stationary cloud with the fixed ratio $r = \tau_c/\tau_a = 2$ (prolate clouds) as a function of line center optical depth τ_a along the semi-minor axis (the upper diagram a) and with $r = 0.5$ (oblate clouds) as a function of the optical depth τ_c along the semi-minor axis (the lower diagram b). The data was fitted by $p_0 = 0.4\tau_0/2(\tau_0 + 1.8)^2 + 4$ for prolate clouds and $p_0 = 0.1\tau_0/0.5(\tau_0+1.1)^2+1$ for oblate clouds. The electric vector is perpendicular to the symmetry axis for prolate clouds and is in the plane spanned by the wave vector $\mathbf{k}$ and $\mathbf{z}$ for oblate clouds.

Figure 5 – The maximum polarization from oblate clouds with fixed semi-major axis $\tau_a = 10$ and various semi-minor axes τ_c from 0.2 to 10. The largest polarization is obtained in the limit $r = \tau_c/\tau_a \rightarrow 0$ with $\tau_c \sim 1$ (*i. e.* the extreme axis ratio with the constraint that the mean number of scatterings ~ 1).

Figures 6a,b,c – The polarization and the mean number of scatterings from prolate spheroids expanding in a shear-free way. The optical depths are chosen to be $\tau_a = 10^5$ and $\tau_c = 2 \times 10^5$ and the internal velocity difference Δv_a ranges from 10^3 to 10^5. The polarization is shown by squares with $1 - \sigma$ error bar and the mean number of scatterings is represented by open circles.

Figures 7a,b,c,d – The polarization and the mean number of scatterings from an anisotropically expanding spherical cloud as a function of internal velocity difference. The line center optical depth of the spheroid is $\tau_0 = 10$ for the lower panels and $\tau_0 = 10^5$ for the upper panels. The negative polarization corresponds to the electric vector perpendicular to the symmetry axis ($z-$axis). The kinematic condition is given by the fixed ratio $r_v \equiv \Delta v_z / \Delta v_x = 2$ or $r_v = 0.5$. The horizontal axis is given by $\Delta v_0 \equiv \max(\Delta v_z, \Delta v_x)$. For $r_v = 2$ we have positive polarization shown as open squares with 1-σ error bars in both upper and lower panels, and for $r_v = 0.5$ the polarization is negative.

Figures 8a,b – The polarization and the mean number of scatterings from a non-homologously expanding cloud. In the lower diagram the geometry is given by $\tau_a = 5$, $\tau_c = 4\tau_a$, and the kinematic conditions are $\frac{dv_x}{dx} = \frac{dv_y}{dy} = \frac{dv_z}{dz}$.

Figures 9 a,b – The polarization from a disk-like distribution with the symmetry axis of each stationary spheroidal cloud aligned to point the center of the disk as a function of inclination angle. Th upper panel is the polarization from a disk consisting of prolate stationary clouds with $\tau_c = 4$ and $\tau_a = 2$, and the lower panel shows the polarization from a disk-like distribution of oblate clouds with $\tau_c = 2$ and $\tau_a = 4$. The fitting curve is the same for both the upper and the lower panels given by $f(\mu) = \frac{p_0(1-\mu)}{1-0.67\mu}$ with $p_0 = 0.015$.

Figures 10a,b – The maximum polarization from a disk-like distribution of prolate (the upper diagram) and oblate (the lower diagram) clouds as a function of the line center optical depth τ_0 along the semi-minor axis of component clouds.

TABLE 1 The line center optical depth of some broad emission lines

Line	f^a	N_i^b	τ_o^c
CIVλ1549	0.38	3.7×10^{-4}	8.8×10^{6}
CIIλ1400	1.0	3.7×10^{-4}	2.3×10^{7}
CIII]λ1909	1.6×10^{-7}	3.7×10^{-4}	4.5×10^{0}
MgIIλ2795	1.25	3.3×10^{-5}	6.6×10^{6}
OVIλ1035	0.26	6.8×10^{-4}	8.5×10^{6}
NVλ1240	0.31	1.2×10^{-4}	2.0×10^{6}

[a] Oscillator strength

[b] Abundance by number (*e. g.* Netzer 1990)

[c] Optical depth at line center

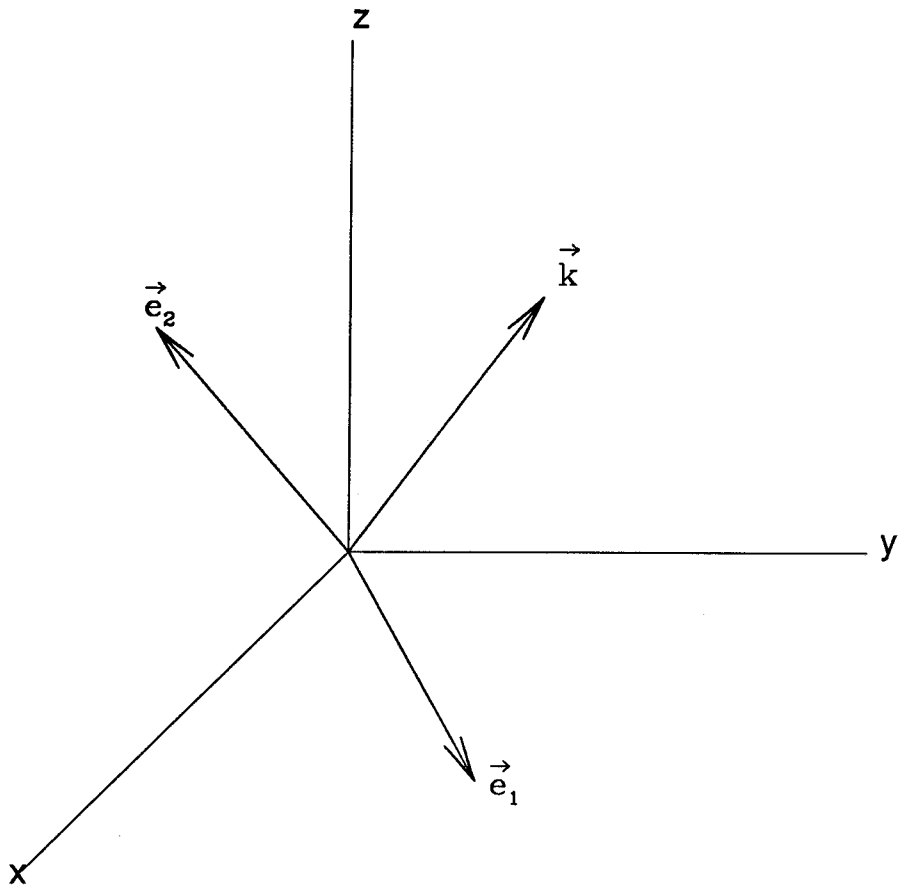

Figure 1

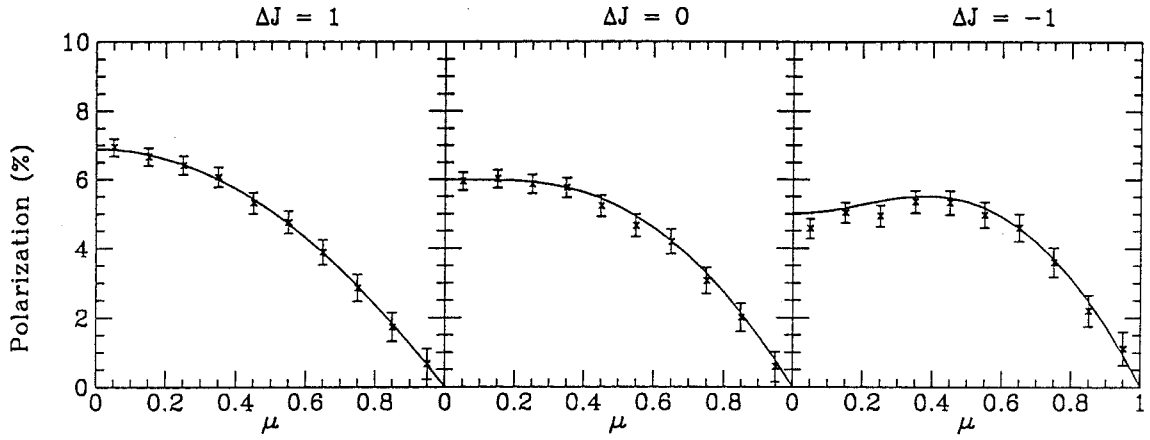

Figure 2

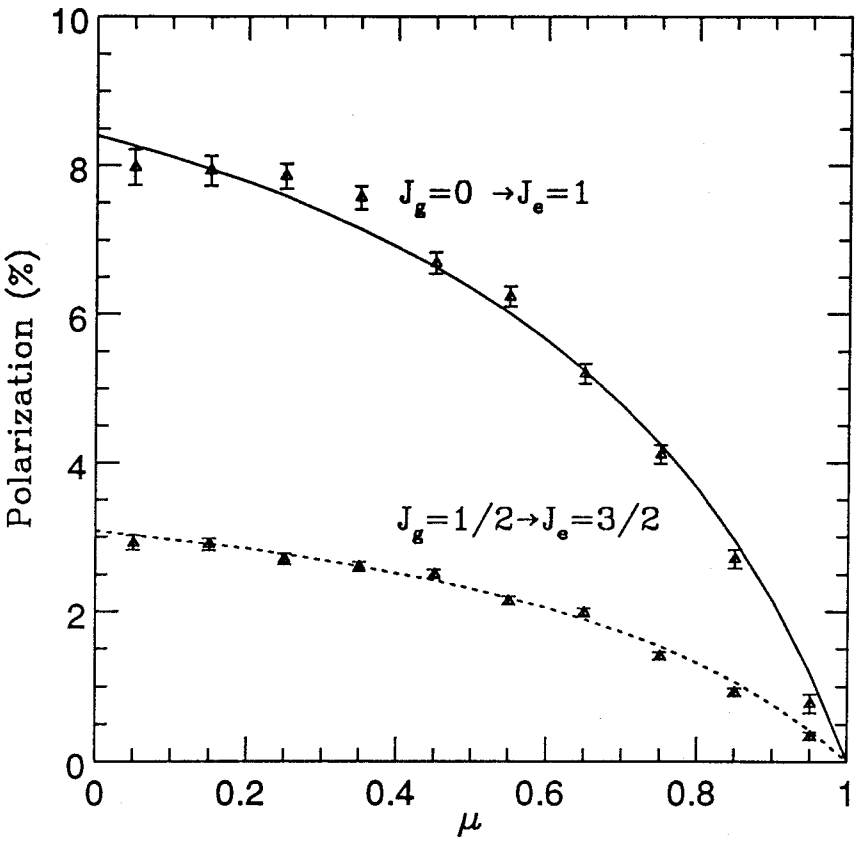

Figure 3

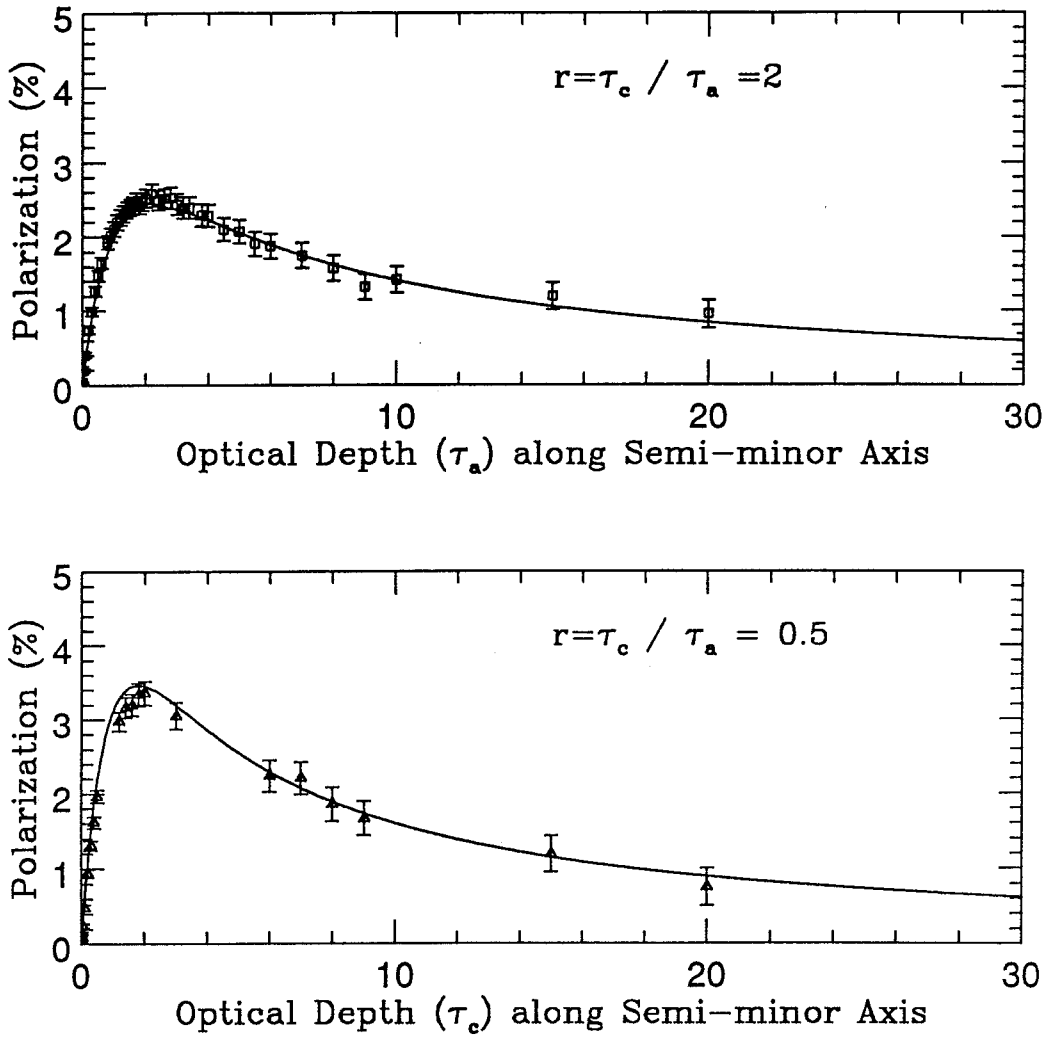
r=τc / τa =2
Polarization (%)
Optical Depth (τa) along Semi−minor Axis
r=τc / τa = 0.5
Polarization (%)
Optical Depth (τc) along Semi−minor Axis

Figure 4

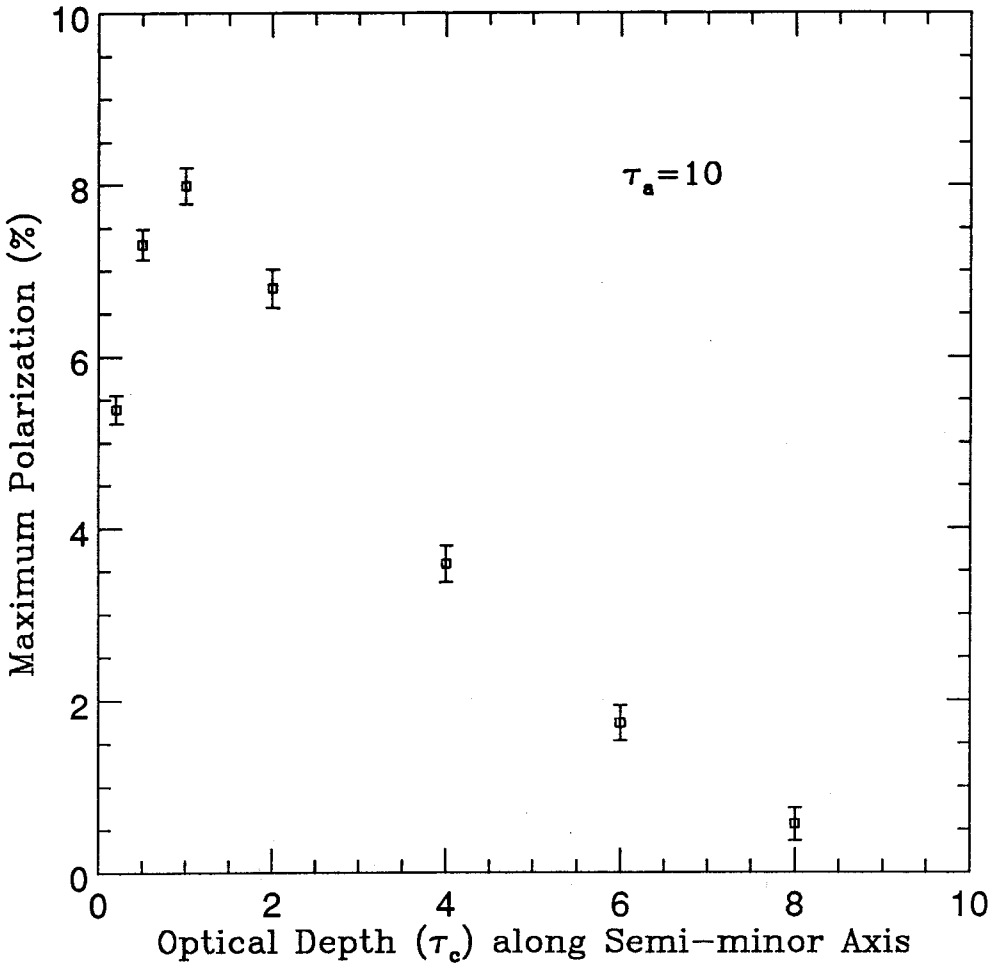
10
8
6
4
2
0
0
2
4
6
8
10
τ_a=10
Maximum Polarization (%)
Optical Depth (τ_c) along Semi-minor Axis

Figure 5

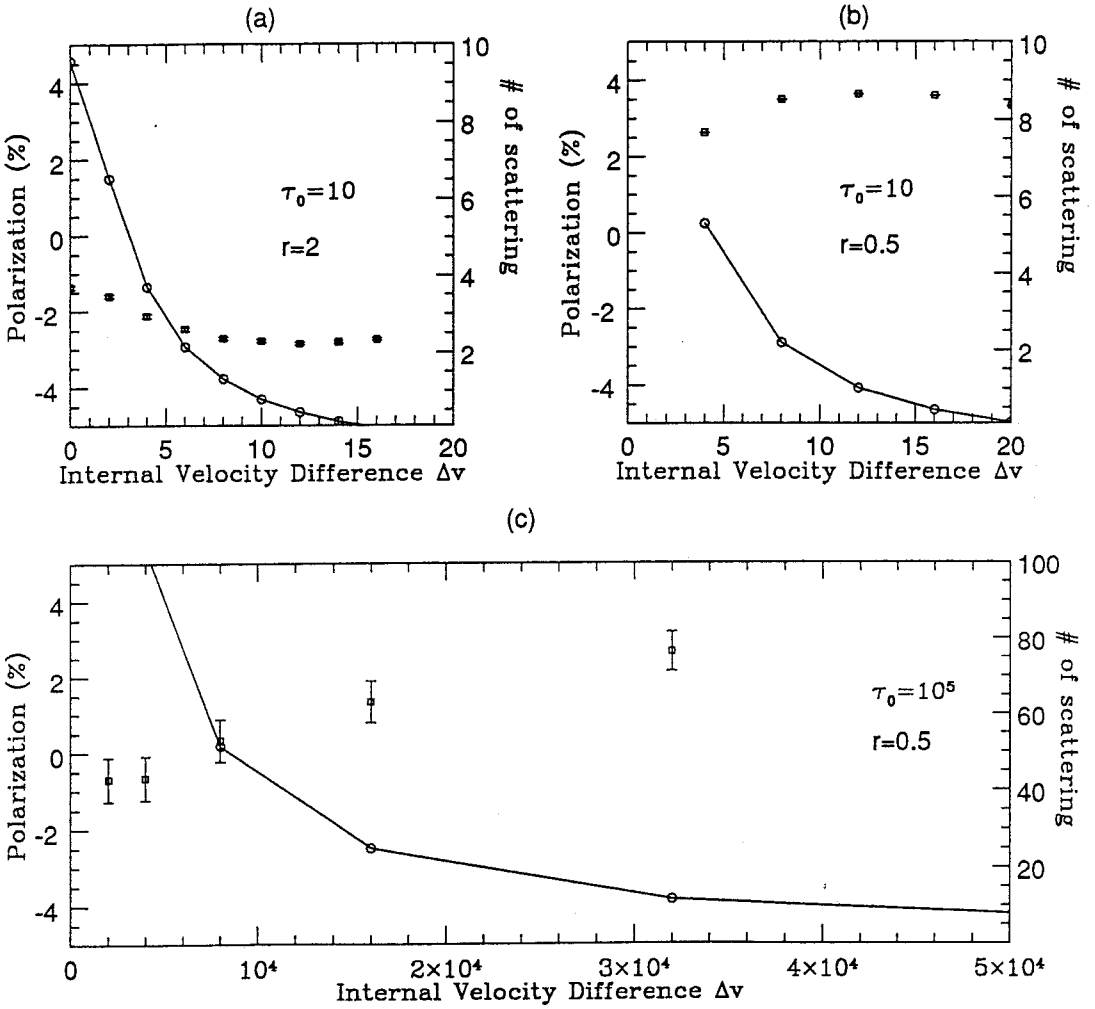
(a)
Polarization (%)
# of scattering
τ_0=10
r=2
Internal Velocity Difference Δv
(b)
Polarization (%)
# of scattering
τ_0=10
r=0.5
Internal Velocity Difference Δv
(c)
Polarization (%)
# of scattering
τ_0=10^5
r=0.5
Internal Velocity Difference Δv

Figure 6

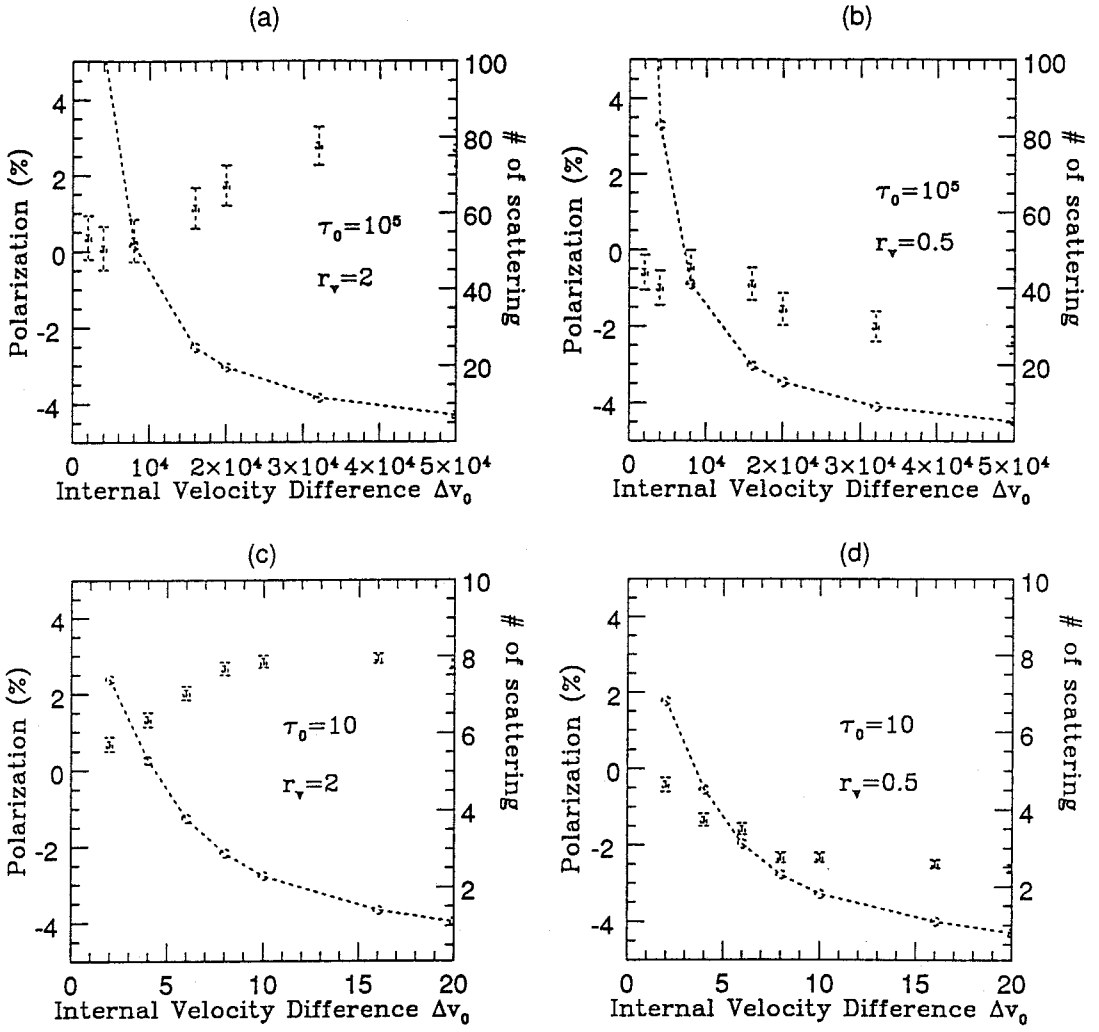
(a)
(b)
(c)
(d)
Polarization (%)
# of scatterings
Internal Velocity Difference Δv_0
$\tau_0=10^5$
$r_v=2$
$r_v=0.5$
$\tau_0=10$

Figure 7

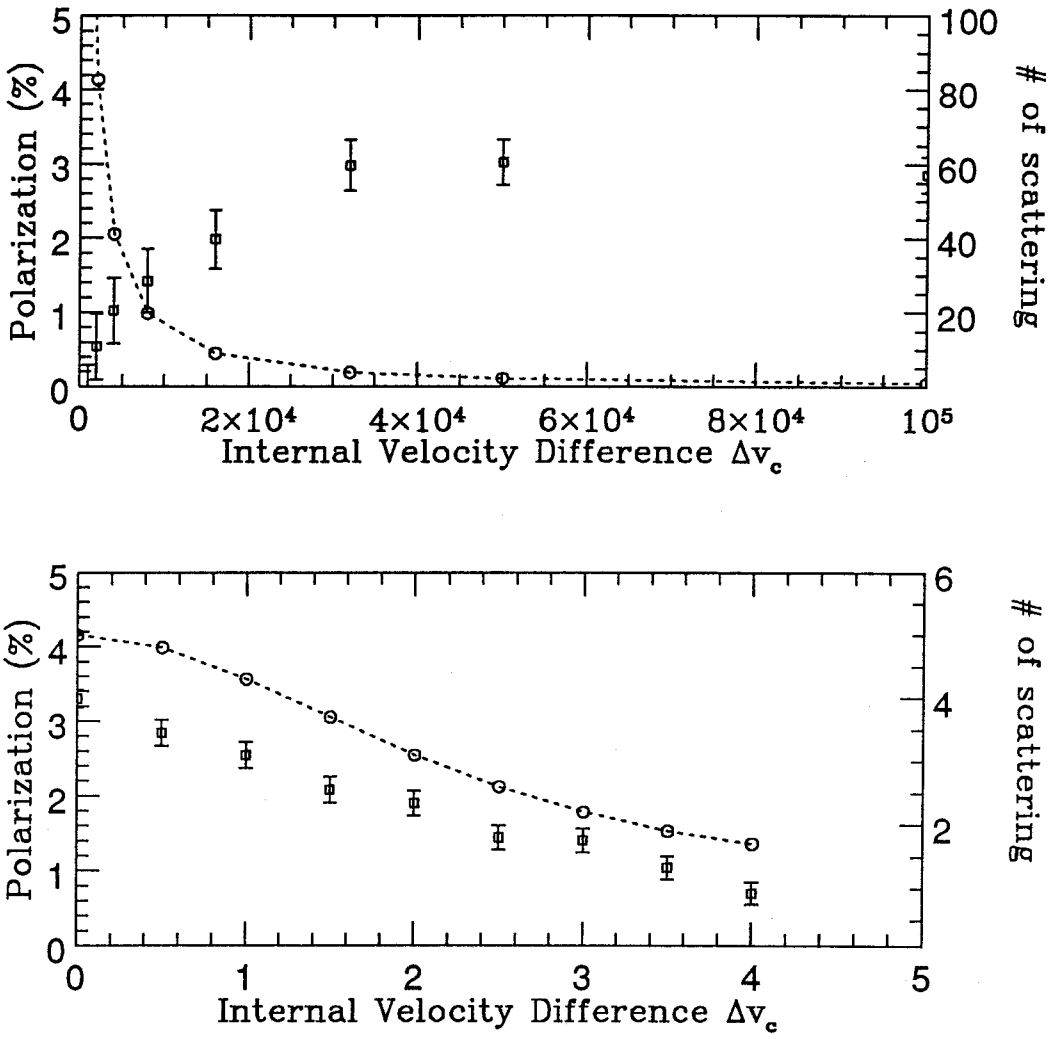
Polarization (%)
# of scattering
Internal Velocity Difference Δv_c
0
2×10⁴
4×10⁴
6×10⁴
8×10⁴
10⁵
20
40
60
80
100
1
2
3
4
5
6

Figure 8

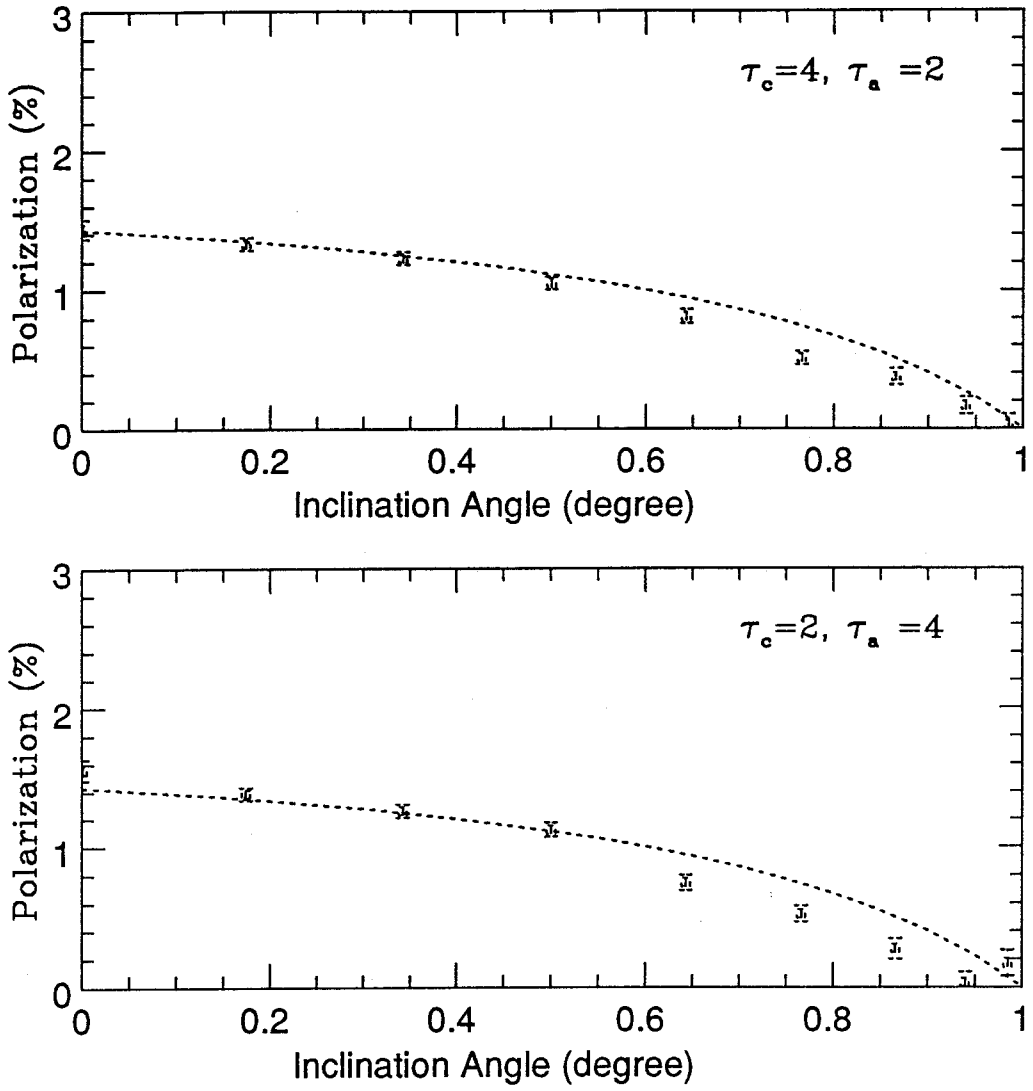
τ_c=4, τ_a =2
Polarization (%)
Inclination Angle (degree)
τ_c=2, τ_a =4
Polarization (%)
Inclination Angle (degree)

Figure 9

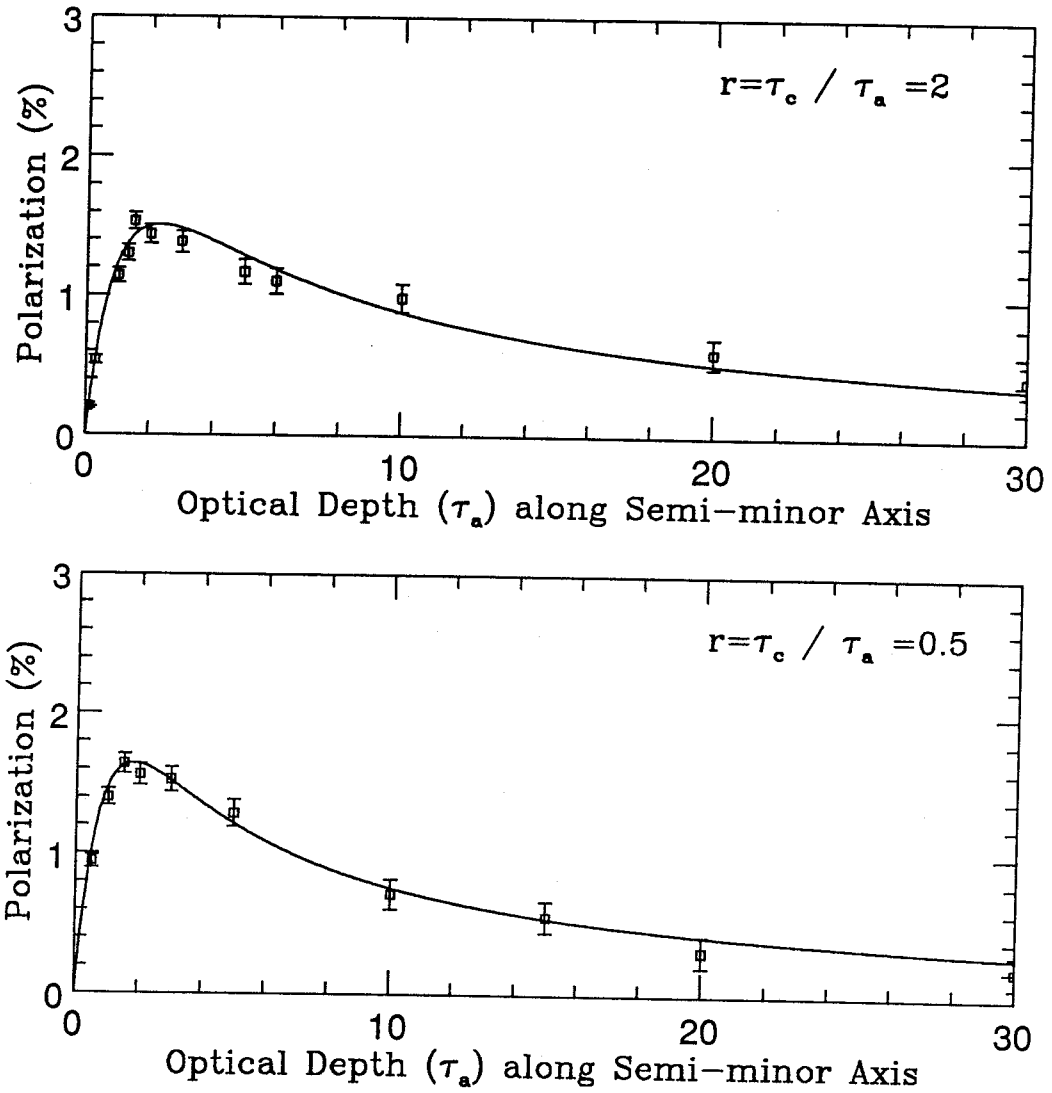
r=τc / τa =2
Polarization (%)
Optical Depth (τa) along Semi−minor Axis
r=τc / τa =0.5
Polarization (%)
Optical Depth (τa) along Semi−minor Axis

Figure 10

4

On the Polarization of Resonantly Scattered Emission Lines Polarization of Quasar Broad Emission Lines and Broad Absorption Line Troughs

H. -W. Lee,

R. D. Blandford

Caltech, Pasadena, CA 91125.

ABSTRACT

The contribution to the expected linear polarization of quasar broad emission and absorption lines from resonance scattering is computed using a Monte Carlo approach for specific, generic models. Attention is focussed on the external illumination of the scattering region. The polarization of the reflected component from an externally illuminated slab with finite optical depth is first considered as a model of a single, dense, broad emission line cloud. A polarization $\lesssim 40$ percent, ($\lesssim 10$ percent) is typically computed for $J = 0 \rightarrow 1$ ($J = 1/2 \rightarrow 3/2$) transitions. Integrating over a population of emission line clouds typically reduces the observed polarization by a factor $\sim (0.1 - 0.3) q_{BELR}$, where q_{BELR} is the covering factor for emission lines, while preserving the relative polarizations of different lines. Consequently, the low degree of polarization observed in the red wings of quasar emission lines limits the density of low column density emission line clouds.

Broad absorption lines are associated with outflowing gas of lower density. The polarization of both the transmitted and the reflected radiation is next computed for simple kinematic models of the outflow and the observed integrated

polarization in the absorption line troughs is found to be typically $\sim$ 10 percent. An equatorial flow model gives a large degree of polarization ($\sim$ 0.15) parallel to the symmetry axis in the absorption trough for the doublet transition J=1/2 $\rightarrow$ 1/2, 3/2, and the polarized flux is found to extend to the redside. In contrast, we obtain a smaller degree of polarization ($\sim$ 0.05) perpendicular to the jet axis from a bipolar flow model and the polarized flux is concentrated to the blue side of the line profile. It is predicted that the trough of singlet J=0 $\rightarrow$ 1 lines like C III λ977 should exhibit larger degrees of polarization if this is due to resonance scattering. Polarization observations of quasar emission lines promise to be a powerful diagnostic of the kinematics of gas in the central pc of a quasar.

1. INTRODUCTION

A distinctive and defining property of many Active Galactic Nuclei (AGN) is the presence of broad emission lines (BEL). Quasars and type 1 Seyfert galaxies typically exhibit lines with widths in excess of $\sim$ 1000 km s^{-1} (*e.g.* Osterbrock 1989). In addition, roughly ten percent of radio-quiet quasars exhibit broad, blue-shifted, absorption line troughs (*e.g.* Weymann *et al.* 1991). Although the kinematic details remain controversial, these observations are widely interpreted in terms of a model in which a central UV continuum source is surrounded by a broad line region containing dense clouds moving with large speeds from which emanates an outflow of more tenuous gas (at least in the case of the radio-quiet quasars).

Spectropolarimetry has already contributed much to our understanding of active galactic nuclei (AGN). In particular, Antonucci & Miller (1985) showed that Seyfert 2 galaxies sometimes show broad line components in their polarized spectra and argued that they were similar to Seyfert 1 galaxies except that their broad emission line regions are occulted by a thick molecular torus at low latitude and scattered by electrons at high latitude (*e.g.* Miller & Goodrich 1990). Polarization can also be created by dust, via transmission and reflection, and through scattering by the resonant ions themselves. The central regions of active galactic nuclei are

manifestly anisotropic and so it is to be expected that scattering generally produces polarization in AGN spectra. To date, polarization observations of AGN spectra have been limited to the brightest objects, but the advent of 10 m class telescopes and more sensitive polarimeters should increase their role as diagnostics.

In Lee, Blandford & Western 1994, (Paper 1), we introduced a formalism for computing the polarization of resonantly scattered emission lines and in Lee (1994, Paper 2), a Monte Carlo code was used to compute the polarization to be expected from a population of non-spherical and anisotropically expanding emission line clouds. It was found that standard emission line clouds emit almost unpolarized line radiation except when they have optical depths $\tau \sim 1$ as may be the case for the semi-forbidden C III] λ1909 transition.

In this paper, we address the possibility that photons are polarized by resonance line scattering after they have left their emission sites. We attempt to make semi-quantitative statements about the expected degree and direction of the polarization of quasar lines. We do this in the context of some fairly general, geometrical and radiative assumptions about the emitting and scattering gas, which we introduce in § 2. In § 3, we compute the polarization to be expected from scattering within the emission line region. We first perform Monte Carlo simulations of scattering by a single, stationary cloud and then estimate the integrated polarization from a large population of clouds. We next turn to broad absorption line quasars (BALQs). The line photons that appear to be "absorbed" are actually scattered by anisotropically distributed, outflowing gas with modest, line optical depths. We compute the magnitude of the resulting polarization in some simple kinematic models of the outflow using a hybrid Sobolev-Monte Carlo method in § 4. Inferences that can be drawn from existing polarization observations of AGN and the promise of future observations are discussed in § 5.

2. GENERIC QUASAR MODEL

2.1 Emission Line Region

We suppose, in common with many models, (*e.g.* Netzer 1990), that there is a compact, central continuum source of unpolarized ionizing radiation of size $\lesssim 10^{16}$ cm, surrounded by a zone, of size $R_{BELR} \lesssim 1$ pc, in which are found dense, line-emitting clouds (with electron density $n_e \sim 10^8 - 10^{10}$ cm^{-3} and temperature $T \sim 1 - 3 \times 10^4$ K). We further suppose that this gas has a small filling factor $f \sim 10^{-6}(R_{BELR}/1\mathrm{pc})^{-2}$, a modest BELR covering factor $q_{BELR} \sim 0.1$, and an ionization parameter $U \equiv n_{UV}/n_e \sim 0.1 - 1$. The velocity distribution of the clouds within this zone determines the line profiles and the clouds may well be stratified so that ions with different ionization potentials are concentrated at different distances from the central continuum source. (*e.g.* Peterson *et al.* 1990). In addition we suppose that there is an opaque disk/torus which prevents an observer from seeing the emission lines from an equatorial direction as well as the opposite hemisphere.

For present purposes, we need only suppose that individual clouds may be modeled as discrete regions that are individually optically thick to the permitted resonance line photons of primary interest to us. In standard cloud models, the hydrogen column densities are supposed to be $N_{\mathrm{H}} \sim 10^{22} - 10^{23}$ cm^{-2} at least five orders of magnitude larger than the minimum column density needed to be optically thick to most of the prominent emission lines (except C III] λ1909 semi-forbidden line). The connectivity and confinement of these clouds is problematic. One possibility (Rees 1987, Emmering, Blandford & Shlossman 1992, henceforth EBS), is that both the confinement and acceleration be attributable to the action of strong magnetic field. The origin of the emission gas is not especially relevant here, although accretion disks (*e.g.* EBS), giant stars (*e.g.* Scoville & Norman 1995) and supernovae (*e.g.* Williams & Perry 1994, Perry & Dyson 1985) have all been considered.

Of great importance for determining the polarization is the velocity distribution of these clouds. It is observed that quasar line profiles are centrally peaked with velocity widths $\Delta V_{em} \sim 10,000$ km s^{-1}. This is generally supposed to represent space motion of the emitting gas, (although electron scattering may contribute to the wings of the lines, Weymann 1970, EBS). In some quasars, the high ionization lines (HIL's) are blue-shifted with respect to the low ionization lines (LIL's) and some broad lines have blue asymmetry (*e.g.* Peterson *et al.* 1991, 1994, Corbin & Francis 1994). This is roughly consistent with an accretion disk model in which a wind accelerates away from a disk. We shall adopt this interpretation for illustrative purpose and use it to bring out some features of line formation in the polarized flux.

2.2 Formation of Broad Absorption Lines

The troughs in BALQs are observed in highly ionized, permitted lines and their velocity widths range up to $\sim 0.1c$, although a fraction exhibit lower ionization broad Mg II absorption. The absorption line profiles are reminiscent of those formed in the spectra of P-Cygni stars, which also suggests that the absorption region is dominated by outflow. Many troughs are "detached" in velocity from their associated emission lines with steep walls at their low velocity ends. This indicates that the kinematics is more complex than the simple radial outflow associated with models of P-Cygni stars. In particular, it suggests that the variation of the radial velocity of the absorbing gas along the line of sight is non-monotonic and exhibits a minimum.

Weymann *et al.* (1991) showed that the emission line properties of BALQs are almost identical to those of non-BALQs and developed a model in which all radio-quiet quasars have outflowing BAL clouds confined to an equatorial fan of total angular width $\sim 20°$. A total column density of outflowing gas $\gtrsim 3 \times 10^{20}$ cm^{-2} is needed assuming solar abundance to absorb throughout the trough, perhaps a few percent of the mean column density associated with the broad emission line region. The filling factor of the absorbing gas is generally assumed to be small for similar

reasons to those given for emission lines. The confinement of the absorbing clouds is also problematic. Again magnetic field provides a possible agency for achieving this.

Absorption troughs have velocity widths that are typically 3 times broader than the emission lines which implies that the absorbing gas is accelerated to speeds well in excess of the local virial speed. It is, however, quite unlikely to be accelerated from rest. It may be derived from emission line clouds (*e.g.* Murray *et al.* 1995), off giant stars in a central cluster (*e.g.* Scoville & Norman 1995), or the surface of an orbiting accretion disk (*e.g.* Weymann *et al.* 1982, EBS, Murray *et al.* 1995). This last possibility implies that the gas will start from zero latitude with the local Keplerian velocity without completely occulting the BELR, as there is no absorption at zero velocity. As the outflowing gas expands away from the disk plane, it will eventually reach the observer's latitude and occult the BELR and continuum. The gas that does this first will presumably have high speed as it originates at small radius. The ray from the observer may then pass through more slowly moving gas, on a different streamline, before finally encountering the gas that has been strongly accelerated. This is one way by which a minimum may be formed in the velocity of the outflow.

Most of the broad absorption troughs are not completely black. It is unreasonable to assume that the column density and ion abundances are adjusted so that the optical depth always saturates at $\tau \sim 2$. We suppose that photons are removed from the beam along the direct line of sight from the continuum source either partially or effectively totally, dependent upon velocity, and that there is scattering from other lines of sight which partially refills the troughs at a level $\lesssim 0.1$ of the continuum flux dependent upon the total covering fraction and velocity of the BAL (*cf.* Turnshek *et al.* 1988, Hamann *et al.* 1993). BALQ variability (Barlow *et al.* 1992 and references therein) is apparently common on timescales of weeks to months and is consistent with this interpretation.

The smoothness of BAL profiles on a velocity scale from comparable with the thermal width of the absorbing gas to $\sim 10,000\mathrm{km\ s^{-1}}$ (Barlow & Junkkari-

nen 1995, in preparation) indicates that the absorbing gas either flows smoothly (*cf.* Murray *et al.* 1995) or is contained in a spray of small clouds (*e.g.* Weymann *et al.* 1982, Arav & Begelman 1994). (Scattering into other lines of sight can also smooth the profiles.) As a consequence, no detailed model of the BAL region is necessary to explore the polarization beyond a rough specification of the disposition of the gas in phase space.

2.3 Polarization Mechanisms

There are many possibilities for creating polarization in the observed line and continuum emission. Firstly, as discussed in Paper 2, individual dense clouds whose ions create line photons following recombination or collisional excitation may be polarizing if they are non-spherical in shape or have an anisotropic velocity gradient tensor. The observed polarization depends upon the global average of these properties over the ensemble of clouds. Typically, this contribution to the polarization is unobservably small for permitted lines, because the scattering optical depth of an individual cloud is so large.

Secondly, polarization may be produced by reflection of resonance line photons. This arises when either an emission line photon produced in an emission line cloud or a continuum photon created in the central continuum source is incident upon an element of gas moving with a bulk velocity that Doppler shifts the photon into resonance with a permitted transition. The column density of resonant gas moving within a thermal velocity width of the resonance necessary to produce a single reflection is typically $\sim 10^{17}$ cm^{-2} for the most prominent UV permitted lines (*cf.* Paper 1). This gas may be found in the emission line regions or in the more tenuous, higher velocity gas associated with the BALR. Reflection of resonance line radiation produces a polarization perpendicular to the scattering plane with a degree that depends upon the scattering angle, in a manner similar to Thomson scattering, being large for a $\pi/2$ scattering and small for forward or backward scattering. The degree of polarization is reduced from that associated with single Thomson scattering on account of multiple scattering and it also depends upon the electronic transition involved. The total degree of polarization

obtained by combining the transmitted and the reflected radiation is dictated by the spatial distribution of scatterers and is likely to be frequency-dependent across the line.

Thirdly, there may be a broad band polarizer present affecting both the lines and the continuum. One possibility is scattering by dust (*e.g.* Laor & Draine 1993). This will create a wavelength-dependent degree of polarization. In addition polarization can be created in transmission if there is an organized magnetic field present along the line of sight. However in this case, an appreciable fraction of the photons that are removed from a beam are not absorbed by the grains but are scattered and, unlike in the case of interstellar polarization, photons scattered into our line of sight from other beams, must be included in the overall polarization. The other common type of broad band polarizer is electron scattering, where the polarization should be frequency-independent (*e.g.* Antonucci & Miller 1985, Tran, Miller & Kay 1992, Goodrich & Miller 1994), and where, as with resonance line reflection, the largest polarization is produced when the scattering angle is $\sim \pi/2$. However, this requires that there be a column density of ionized gas $\gtrsim 10^{23}$ cm^{-2}.

3. POLARIZATION FROM THE EMISSION LINE REGION

3.1 Reflected Polarization from a Single Cloud

In Paper 2, we developed a Monte Carlo code to compute the polarization of resonantly scattered photons originating within an anisotropically expanding cloud. The same code is used now to compute the polarization of resonantly scattered radiation originating outside the cloud and reflected by it. In this case, some photons are only scattered once and these can be highly polarized. However other photons are multiply scattered and this usually lowers the overall degree of polarization. In addition, some photons may penetrate the cloud and be transmitted.

We model the cloud as a plane slab of infinite extent in the x and y directions and of finite optical depth τ in the z direction. For the moment, we work in the rest frame of the slab and ignore velocity gradients. The polarization decreases as

the optical depth τ of the slab increases and at $\tau \sim 10$ the polarization reaches the saturation value. The largest polarization arises when the ground state angular momentum quantum number is 0, as discussed in Papers 1 and 2.

In Fig. 1, we show the result of computing the polarization of the emergent light scattered from a slab with $\tau = 5$, where the slab is illuminated by an unpolarized source. Introduce spherical polar coordinates θ, ϕ and let the incident photons propagate along a direction (θ_{in}, ϕ_{in}) and be scattered into (θ_{out}, ϕ_{out}). The scattering angle is $\alpha = \cos^{-1}[\cos\theta_{in}\cos\theta_{out} + \sin\theta_{in}\sin\theta_{out}\cos(\phi_{in} - \phi_{out})]$ and the direction of polarization is perpendicular to the scattering plane. The transition is J= 0 $\rightarrow$ 1 (*e.g.* C III λ977, Al II λ1671). The polarization is most dependent on α, but varies slowly for $\mu_{out} \gtrsim 0.5$. The highest polarization(~ 0.5) is attained, when $\alpha \sim \pi/2$. The polarization for the transition J= 1/2 $\rightarrow$ 3/2 is displayed in Fig. 2. Most of the prominent AGN emission lines (including C IV λ1549, Si IV λ1397, Mg II λ2798, N V λ1240, O VI λ1031) are doublets with the higher frequency component having weight 2/3 and corresponding to a J= 1/2 $\rightarrow$ 3/2 transition and the lower frequency component corresponding to J= 1/2 $\rightarrow$ 1/2 with weight 1/3. The velocity separations of these doublets range from $\sim$ 500 km s^{-1} for C IV to $\sim$ 2600 km s^{-1} for Si IV. These splittings are conveniently large compared with the thermal velocities within individual clouds, but small compared with total line velocity widths. As explained in Paper 1, when photons are resonant with the J= 1/2 $\rightarrow$ 1/2 transition, the scattered polarization is zero, independent of the incident polarization. Therefore we can average the polarization over the doublet by multiplying the result for a J= 1/2 $\rightarrow$ 3/2 simulation by 2/3. We find that the polarization behavior for J= 1/2 $\rightarrow$ 3/2 is almost identical to the case of the transition J= 0 $\rightarrow$ 1 except that the overall degree of polarization is reduced by a factor $\sim$ 0.4. This is similar to the ratio for a single scattering through an angle $\pi/2$ as shown in Paper 1 and for the integrated polarization from a stationary ellipsoidal cloud as shown in Paper 2. Therefore the net reflection polarization expected for scattering by a single cloud for a J= 1/2 $\rightarrow$ 1/2, 3/2 doublet transition

like C IV λ1549 is expected to be $\sim$ 30 percent of the value for a J= 0 $\rightarrow$ 1 singlet case like C III λ977.

We also consider the dependence on the azimuthal angle between the source and the observer, fixing the position of the scatterer. In the left panel of Fig. 2, the numerical result is shown by various points with error bars where $\mu = \frac{1}{2}$(fixed) and ϕ_{out} takes the values of 0, $\pi/4$, $\pi/2$, $3\pi/4$, and π. The theoretical maximum polarization (*i.e.* single electron scattering) is plotted for comparison with the case of the transition J=0 $\rightarrow$ 1. In the right panel the polarization from the transition J=1/2 $\rightarrow$ 3/2 is shown. The degree of polarization remains about 40 percent of the value for J=0 $\rightarrow$ 1. Note that the scale is different and the polarization should be further reduced by a factor of 2/3 for the case of doublet transition J=1/2 $\rightarrow$ 1/2, 3/2. Again the largest polarization is seen when the scattering angle is 90°. When $\phi_{in} \sim \phi_{out}$, the electric vector lies in the slab. Moreover when $|\phi_{in} - \phi_{out}| \sim \pi/2$, the polarization direction is roughly perpendicular to the slab.

3.2 Polarization from Reflection by a Population of Emission Line Clouds

We next consider the scattering of unpolarized light incident upon an ensemble of emission line clouds and compute the observed polarization. For illustration, we adopt a particular, idealized, kinematic model in which the clouds are illuminated by a central continuum source and there is an optically thick accretion disk present, so that only the hemisphere nearer to the observer can be seen (*cf.* EBS). We assume that there is axial symmetry. The velocity of each cloud is assumed to be purely poloidal making an angle θ_i with the disk and to vary with distance from the central source in proportion to $r^{-1/2}$ over three decades of radius (*cf.* Fig. 3). We assume that the number density $n(r)$ of clouds is proportional to r^p, where $p \sim -1.5$. The optical depth of each cloud is taken to have a constant value τ for a resonant photon, at line center. Hence the frequency of the emergent photons is determined by the velocity component of the scattering cloud along the line of sight.

In Fig. 4, we show the polarization, the flux of the scattered component and the polarized flux for $\mu_{out} = 0.2, 0.4, 0.6$, and 0.8 respectively when the clouds are

moving along a line inclined at an angle $\theta_i = 50°$ to the disk. The horizontal axis represents the observed frequency and the transition is J= 0 $\rightarrow$ 1. The degree of polarization of the scattered component is shown to be ~ 0.35 to the redward for $\mu_{out} < 0.5$, and double peaks appear for $\mu_{out} > 0.5$. Clearly a large polarization is obtained when the incoming and outgoing directions are orthogonal, and this condition is more likely to be met at small values of μ_{out}.

In Fig. 5, we show the numerical result for the transition J= 1/2 $\rightarrow$ 3/2 with the same conditions as in Fig. 4. The overall behavior of the polarization and the polarized flux is almost identical to that of the transition J= 0 $\rightarrow$ 1 with the exception that the degree of polarization is reduced by a factor ~ 0.4. The typical degree of polarization observed in the scattered radiation for this transition is $p \sim 0.1$. (Note that for the doublet transition this should be further reduced by a factor of 2/3 again.) However, we should not expect to see this polarization with observations. The success of reverberation mapping (Peterson *et al.* 1994) indicates that most broad line photons are not resonantly scattered. In fact if we denote the total covering factor of standard broad line clouds by q_{BELR}, and the ion thermal velocity by v_{th}, then the observed degree of polarization will be smaller than the degree of polarization in the scattered radiation by a factor $\sim q_{BELR} v_{th}/\Delta V$, and will be negligibly small.

3.3 Influence of Small Clouds

The clouds that emit most of the line photons may be just the largest representatives of a distribution that extends down to smaller sizes. These clouds probably have similar pressures and temperatures to the standard clouds and consequently similar densities. Although the integral of the hydrogen column density along a line of sight may be dominated by standard, large clouds, the smaller clouds can still be observationally significant if they are spread in velocity and "fill in" the absorption line profiles of the prominent resonance line transitions so that q_{BELR} is effectively very large. Just such a phase as this has already been proposed on quite different grounds by Shields *et al.* (1995). These hypothetical,

small clouds will therefore impede the free escape of emission line photons and may, as a consequence, impose polarization upon the emission lines by increasing the effective covering factor.

4. POLARIZATION FROM THE ABSORPTION LINE REGION

4.1 Scattering Optical Depth

We are interested in the optical depth of an outflow in which the velocity changes monotonically with position in such a manner that there is a single point at which an ion moving with the rest frame of the fluid can resonantly absorb photons of a given frequency. Absorption actually occurs within a neighborhood of this point where the bulk velocity lies within a few thermal widths of its value at resonance. The conventional technique for handling this type of problem is the Sobolev method (*e.g.* Sobolev 1947, Rybicki & Hummer 1978). In the presence of a fairly large velocity gradient, the Sobolev optical depth can be written as

$$\begin{aligned}\tau =& n_i \int \sigma d\nu c/[\nu(dV/ds)] \\ =& n_i f \lambda \left(\frac{\pi e^2}{m_e c}\right)\left(\frac{dV}{ds}\right)^{-1} \\ \sim& 0.3(X_i/10^{-4}) f \lambda_3 (dN_{H20}/dV_9),\end{aligned} \tag{4.1}$$

where s is the distance along the line of sight, f is the oscillator strength, n_i is the ion density, $X_i = n_i/n_H$ is the ion abundance relative to hydrogen atom, $\lambda_3 = \lambda/1000\mathring{A}$ refers to the emitted wavelength, $dV_9 = d(V/10^9 \mathrm{cm\ s^{-1}})$ and $dN_{H20} = n_H ds/10^{20}\mathrm{cm^{-2}}$ is the differential column density of hydrogen along the line of sight in unit of $10^{20}\mathrm{cm^{-2}}$. Note that this expression is independent of the ion thermal speed $\lesssim 10$ km s^{-1}. Adopting $\tau \sim 1$, $X_i \sim 10^{-4}$, $f \sim \lambda_3 \sim 1$, we see that the typical column density over which absorption of a given line photon occurs is $\sim 10^{17}$ cm^{-2}. However, a total column of $\gtrsim 3 \times 10^{20}$ cm^{-2} is necessary to absorb throughout the whole absorption trough. These columns are small compared with the column associated with a single, standard emission line cloud.

4.2 Collisional Effects

In Paper 1, we distinguished collisional mixing, when the collisions are much more frequent than radiative excitation from the ground state, from radiative mixing, when the reverse is true. We showed that radiative mixing obtains when the ionization parameter

$$U = \frac{\int_{\nu_L}^{\infty} d\nu F_\nu / h\nu}{cn_e} \sim \left(\frac{L_{UV}}{10^{46}\mathrm{ergs}^{-1}}\right)\left(\frac{r}{10^{18}\mathrm{cm}}\right)^{-2}\left(\frac{n_e}{10^{7}\mathrm{cm}^{-3}}\right)^{-1} \tag{4.2}$$

satisfies

$$U \gtrsim 0.04 T_4^{1/2} \nu_{15}^{3/2} f^{-1}, \tag{4.3}$$

where f is the oscillator strength, and ν_L is the Lyman limit frequency. This inequality is well satisfied in most models (*cf.* Hamann *et al.* 1993). Semi-forbidden transitions may, however, be collisionally mixed (*cf.* §5.1).

The rates for collisional excitation are lower by an exponential factor than the rates for collisional mixing of the ground state sublevels. It therefore follows *a fortiori* that we should be able to ignore collisional production of photons in the BAL region and we shall assume this. Furthermore, the excitation time is always short compared with the anticipated dynamical time and so radiative equilibrium can be safely assumed.

4.3 The Sobolev-Monte Carlo Approach

The conventional Sobolev approach to line radiative transfer in moving media involves expanding the velocity field to first order about the point of resonance and solving approximately the equations of continuum radiative transfer under the escape probability approximation (*e.g.* Rybicki & Hummer 1978). Usually this is done without regard to polarization. It is possible to extend this approach to incorporate polarization (*e.g.* Jeffery 1990 and references therein) but it turns out to be easier and more appropriate for extension to global outflow models to replace solving approximate equations of radiative transfer by a Monte Carlo simulation. We now illustrate the general principles involved by computing the scattered radiation when an unpolarized beam is incident upon some simple flows.

Consider a photon propagating in the direction $\mathbf{n}_i$ with frequency $\nu_i = \nu_0 + \Delta\nu$, where ν_0 is the line center frequency of a given ion after the i'th scattering at $\mathbf{X}_i$. The Doppler shift $\Delta_i \equiv \Delta\nu/\nu_0$ is given by

$$\Delta_i = \mathbf{n}_i \cdot (\mathbf{V}(\mathbf{X}_i) + \mathbf{v}_i)/c, \tag{4.4}$$

where $\mathbf{V}(\mathbf{X})$ is the velocity field of the flow and $\mathbf{v}_i$ is the velocity of the i'th scatterer relative to the local flow. A distance s along the direction $\mathbf{n}_i$ we may approximate the velocity field by

$$\mathbf{V}(\mathbf{X}_i + s\mathbf{n}_i) = \mathbf{V}(\mathbf{X}_i) + s(\mathbf{n}_i \cdot \nabla)\mathbf{V}. \tag{4.5}$$

The component of velocity along $\mathbf{n}_i$ of the next scatterer must then satisfy

$$\mathbf{n}_i \cdot \mathbf{v}_{i+1} = \mathbf{n}_i \cdot \mathbf{v}_i - s\mathbf{n}_i \cdot (\mathbf{n}_i \cdot \nabla)\mathbf{V} \tag{4.6}$$

and the new Doppler shift is

$$\Delta_{i+1} = \Delta_i + (\mathbf{n}_{i+1} - \mathbf{n}_i) \cdot (\mathbf{V}(\mathbf{X}_{i+1}) + \mathbf{v}_{i+1})/c. \tag{4.7}$$

We assume that the 1D velocity $v = \mathbf{n} \cdot \mathbf{v}$ has a Maxwellian distribution $f_M^1(v) \equiv (1/\sqrt{2\pi})\exp(-v^2/2)$, where we measure the flow velocity in units of the thermal velocity. As the natural line width is negligible compared with the thermal width, the optical depth τ_{i+1} between the i'th and $(i+1)$'th scattering is given by

$$\begin{aligned}\tau_{i+1} =& \int_0^{|\mathbf{X}_2 - \mathbf{X}_1|} ds \int d\mathbf{v} f_M^3(\mathbf{v})\sigma(\nu) \\ =& \frac{1}{2}\tau_0 |\mathrm{erf}(\mathbf{n}\cdot\mathbf{v}/\sqrt{2}) - \mathrm{erf}([\mathbf{n}\cdot\mathbf{v} - (\mathbf{X}_2 - \mathbf{X}_1)\cdot(\mathbf{n}\cdot\nabla)\mathbf{V}]/\sqrt{2})|,\end{aligned} \tag{4.8}$$

where $f_M^3(\mathbf{v}) \equiv f_M^1(v_x) f_M^1(v_y) f_M^1(v_z)$ is a 3 dimensional Maxwellian distribution. Here, τ_0 is given by a generalization of Eq. (4.1)

$$\tau_0 \equiv n_i f \lambda \left(\frac{\pi e^2}{m_e c}\right) |\mathbf{n} \cdot (\mathbf{n} \cdot \nabla)\mathbf{V}|^{-1}. \tag{4.9}$$

The escape condition is written as $|\mathbf{X}_2 - \mathbf{X}_1| \to \infty$ and in this case Eq.(4.9) reduces to

$$\tau_{\rm esc} = \frac{1}{2}\tau_0 \begin{cases} 1 + {\rm erf}(\mathbf{n}\cdot\mathbf{v}/\sqrt{2}) & \text{for } \mathbf{n}\cdot(\mathbf{n}\cdot\nabla)\mathbf{V} > 0 \\ 1 - {\rm erf}(\mathbf{n}\cdot\mathbf{v}/\sqrt{2}) & \text{for } \mathbf{n}\cdot(\mathbf{n}\cdot\nabla)\mathbf{V} < 0. \end{cases} \tag{4.10}$$

The electron collision frequencies are large compared with $|\nabla V|$, and so it is reasonable to assume a Maxwellian ion distribution function. However, this is not a crucial assumption. If there are relatively more highly suprathermal ions in the distribution function, then the photons will have a higher probability of being given a larger Doppler shift. However, there will be a compensatory increase in the opacity at this frequency and the escape probability per scattering will remain $\sim \tau_0^{-1}$. If, however, there are *no* sufficiently suprathermal ions, so that the photons cannot be Doppler shifted enough to escape directly, then spatial diffusion is inevitably important and our results should be modified.

Since the local thermal speed is small compared with the flow velocity, we can introduce Sobolev surfaces, for a given frequency shift Δ and observer direction $\mathbf{n}$ where the flow velocity $\mathbf{V}(\mathbf{X})$ satisfies $\mathbf{n}\cdot\mathbf{V}/c = \Delta$. Photons escape from the vicinity of a Sobolev surface by diffusion in frequency rather than configuration space, and so their last scattering sites are near Sobolev surfaces.

The Sobolev-Monte Carlo procedure then begins by locating the point where the incident photon frequency matches the Doppler shift associated with the bulk velocity. We fix this as the origin of the coordinate system. We next pick a random number $\mathcal{R}$ in $[0,1]$ and assign an optical depth $\tau = -\ln(\mathcal{R})$. If $\tau > \tau_0$, the photon will be transmitted without scattering. Otherwise, we use Eq. (4.8) to determine the location of the first ($i = 1$) scattering as well as the component of ion velocity along $\mathbf{n}$. A new propagation direction $\mathbf{n}$ and polarization are generated according to the reemission probability distribution and the local ion velocity component perpendicular to the previous wavevector is also produced from a 1-dimensional Maxwellian distribution (See Paper 2) to obtain the new Doppler shift along the new direction using Eq. (4.7). We then iterate until the photon escapes noting the emergent direction, Doppler shift and polarization.

4.4 Scattering at a Singlet Sobolev Surface: J= 0 → 1

We consider first the local problem, that is, scattering at a single Sobolev surface of the unidirectional monochromatic incident radiation field. For the moment, we confine our attention to the simple case of a singlet $J = 0 \rightarrow 1$ for Be-like ions such as C III, N IV, O V, where the polarization pattern is identical to that familiar from classical Thomson scattering.

4.4.1 Parallel Expansion

We assume that the incident photons propagate along the z-direction which coincides with the only non-zero component of velocity. That is to say $V_z = V_{z0} + zV'$. The Sobolev optical depth along the direction $\mathbf{n} = (\sin\theta\cos\phi, \sin\theta\sin\phi, \cos\theta)$ is then given by

$$\tau_{\rm esc} = \tau_0/\cos^2\theta, \tag{4.11}$$

where τ_0 is the optical depth along the $z-$direction. τ_0 is determined by atomic physics and the local ion density on the Sobolev surface. Note that the optical depth diverges in the perpendicular direction and photons do not escape this way. In Fig. 6a the degree of polarization and the emergent photon flux are shown as a function of $\mu \equiv \cos\theta$ for different τ_0. Observationally, a useful polarization measure is the ratio of the observed polarized flux F_P to the total continuum flux F_C, estimated from measurements at wavelengths where the BALR is transparent. We find that

$$\frac{F_P(\nu,\mathbf{n})}{F_C(\nu,\mathbf{n})} = \frac{1}{F_C(\nu,\mathbf{n})}\int d\Omega_{BALR}\frac{dP}{d\Omega}(\nu,\mathbf{n}), \tag{4.12}$$

where $d\Omega_{BALR}$ is the solid angle subtended by an element of BALR cloud at the continuum source and $dP/d\Omega$ is the polarized flux scattered per sterad towards the observer. The polarization ratio $R_P = (1/F_C)(dP/d\Omega)$ can be estimated from the Monte Carlo simulations by the product of the fraction of incident photons scattered per sterad and the degree of polarization. As the total solid angle subtended by the BAL region is believed to be $\Omega_{BALR} \sim 1$ sterad, a suitably averaged R_P is a measure of the ratio F_P/F_C to be expected from a global model.

As was the case for scattering by a slab (§ 3.1), the largest degree of polarization is obtained when the last scattering is through an angle close to a right-angle. However, photons with $\theta \sim \pi/2$ cannot escape and peak polarization ratio is found for $\theta \sim 45°, 135°$. When $\tau_0 \lesssim 2$, the maximum polarization ratio is $R_P \sim 0.01$; roughly half the photons are scattered once and most of the remainder traverse the Sobolev surface unscattered. The polarization is almost symmetrical with respect to $\theta = \pi/2$, reflecting the symmetry of the cross section and the preponderance of single scatterings. When $\tau_0 \gtrsim 2$, the polarization ratio diminishes and backward scattering starts to dominate. This asymmetry has its origin in the location of the photon source. The first scattering usually occurs before the resonant surface is reached and, on average, the photon has a negative Doppler shift. It is therefore less likely to diffuse in velocity space and escape with a positive Doppler shift than be reflected spatially and escape with $\Delta < 0$. It is found that when $\tau_0 \sim 10$, 56% of the photons are reflected at a Sobolev surface.

4.4.2 Isotropic Expansion

As a second example of local scattering at a Sobolev surface, we consider a locally isotropic expansion - a "Hubble" flow. This is appropriate for purely radial expansion with $V_r \propto r$. The results are quite similar to those found for the parallel expansion except that highly polarized photons once-scattered through $\sim \pi/2$ can now escape. The peak polarization ratio for side-scattering is now ~ 0.02 for $\tau_0 \sim 2$. Again strong backscattering is apparent at large optical depth (*cf.* Fig. 6b).

4.4.3 Perpendicular Expansion

For our third, simple example, we suppose that the flow expands almost entirely transversely ($\tau(\mu) = \tau_0/(1-\mu^2)$). This is a model of a spherical outflow with nearly constant radial velocity. Here, the escape of low polarization forward- and backward scattered photons is inhibited and effectively all normally incident photons are scattered once. R_P is increased further to a peak value $R_P \sim 0.04$.

In this case the bias to backscattering sets in at a lower value of the transverse optical $\tau \gtrsim 1$ (*cf.* Fig. 6c).

4.4.4 Converging Flow

In order to illustrate the changes introduced when there is a simple, converging flow such as might be associated with a shock front, we suppose that the velocity gradient is negative along the propagation direction of the incident photon and positive along the two orthogonal directions. It is assumed that the absolute values for the velocity gradients are equal, *i.e.* $\tau(\cos\theta) = \tau_0/(|1 - 2\cos^2\theta|)$. The results are shown in Fig. 6d. Since the Sobolev optical depth goes to infinity at $\mu \equiv \cos\theta = \pm 2^{-1/2}$, there are local minima in those directions in the polarized flux. A peak value $R_P \sim 0.03$ is achieved at $\tau_0 \sim 2$ and the forward-backward asymmetry begins to show up at $\tau_0 \sim 5$.

4.5 Scattering at a Doublet Sobolev Surface: J= 1/2 → 1/2, 3/2

Resonance scattering by ions that are isoelectronic with Li atoms like C IV, N V, O VI is more complicated when the velocity in the flow changes by more than the doublet separation, expressed as a velocity. (We are indebted to Ray Weymann who urged us to consider the feasibility of separating doublets in polarization.) This appears to be relevant for BAL regions in contrast to individual BEL clouds because the absorption line profiles are known to be smooth, implying that there are no gaps in velocity space along a typical line of sight at a resolution $\sim$ 8 km s^{-1} (Barlow & Junkkarinen 1995 in preparation).

Consider first a single photon emitted by the central continuum source and incident upon an expanding outflow. Let its wavelength be blueshifted with respect to the emission line by a velocity $\sim 20,000$ km s^{-1} say, so that it lies outside the emission line and well within the observed trough. The first resonant velocity surface that it will encounter is that associated with the J= 1/2 → 3/2 transition. Dependent upon the Sobolev optical depth along its direction of propagation it may be scattered one or more times within a distance corresponding to a few thermal widths of it original resonant surface. It will emerge along a new direction

with a frequency that is almost identical to its initial frequency when measured in the fluid rest frame, but which will be redshifted by typically $\sim 20,000$ km s^{-1} in the AGN frame. On average it will be polarized. If the fluid is expanding in all directions about the original point of resonance, then the photon will have a second opportunity to scatter as it encounters the J= $1/2 \rightarrow 1/2$ resonance. The optical depth will be reduced from that for the J= $1/2 \rightarrow 3/2$ by one factor of two to account for the different statistical weight of the transition and changed by the inverse ratio of the velocity gradient along the propagation direction. If there are one or more scatterings at this second resonance, then this time the emergent photon will, on average, be unpolarized. It will also be emitted isotropically. *One scattering in the J= $1/2 \rightarrow 1/2$ resonance suffices to erase all memory of the incident direction of propagation and polarization.* At large optical depth, resonantly scattered photons will be isotropized and depolarized. At small optical depth, a few photons will be scattered once in the J= $1/2 \rightarrow 3/2$ resonance and most of these will escape with no further J=$1/2 \rightarrow 1/2$ scattering and emerge with high polarization.

4.5.1 Parallel Expansion

We carry out a Monte Carlo simulation to the parallel expansion case discussed for the J= $0 \rightarrow 1$ case, and show the result in Fig. 7a. The only changes that are necessary are to modify the radiation pattern and polarization of the radiation scattered at the J= $1/2 \rightarrow 3/2$ resonance Sobolev surface and then to give all emergent photons, including those that are unscattered, an opportunity of being scattered at the J= $1/2 \rightarrow 1/2$ resonance. If they are scattered, then they emerge isotropically without polarization. As before, at small optical depth, the scattering is mainly in the forward and backward directions. Therefore those photons that do avoid J= $1/2 \rightarrow 1/2$ scattering have a low polarization on average. Therefore the emergent polarization is very small ($R_P \sim 0.001$) and for $\tau \gtrsim 2$, the polarization effectively vanishes.

4.5.2 Isotropic Expansion

As might be expected from the foregoing discussion, a larger degree of polarization ensues when sideways scattering is allowed ($R_P \lesssim 0.006$). The rapid decrease in R_P for $\tau_0 \gtrsim 2$ is deduced from the fact that the unpolarizing $1/2 \rightarrow 1/2$ resonance photons contribute increasingly to the scattered radiation field. The forward-backward asymmetry shows up $\tau \sim 5$. However, due to the rapid decrease of R_P the polarization is negligible for $\tau \gtrsim 10$ (*cf.* Fig. 7b).

4.5.3 Transverse Expansion

When sideways scattering is required, we find a peak value $R_P \sim 0.02$, about half the value for the J= $0 \rightarrow 1$ resonance(*cf.* Fig. 7c). However, the polarization rapidly decreases with increasing τ for the same reason as in the preceding case.

4.5.4 Converging Flow

A maximum value of $R_P \sim 0.01$ is seen when $\tau_0 \sim 1$, which is comparable to the perpendicular expansion case. The polarization behavior is also similar to the perpendicular expansion except for the existence of local minima in R_P because of the infinite optical depth at $\mu = \pm 2^{-1/2}$. Since the flow is contracting in the directions with $|\mu| \leq 2^{-1/2}$, all the photons scattered in those directions are out of resonance with the transition J=$1/2 \rightarrow 1/2$. These photons escape without further scattering and hence do not suffer any depolarization. For $\tau_0 \gtrsim 5$ the local minima in R_P disappear and the only observable polarized flux is seen in the directions with $|\mu| \leq 2^{-1/2}$ (*cf.* Fig. 7d).

4.6 Scattering at Multiplet Sobolev Surfaces-Lyα-NV

Lyα emission lines are rarely prominent in BALQs. This is usually attributed to absorption of the emission line by outflowing NV ions. The NV doublet (separation 970 km s^{-1}) is separated from the Lyα blended doublet (separation 1 km s^{-1}) by a velocity $\Delta V = 5900$ km s^{-1}. This is a significant fraction of the width of the whole absorption trough. On the presumption that the initial spectrum at the base of the acceleration contains a flat continuum plus a broad, blended Lyα-NV emission line, Turnshek *et al.* (1988) and Arav & Begelman (1994) have proposed

that the outflowing BAL gas should be subject to mild line-locking. Specifically, they suggest that the radiative acceleration of the gas increase and then decrease as the NV ions move into and then out of resonance with the blended emission line. The velocity history is then imprinted in the trough of a more passive ion like C IV which should show less absorption at a blueshift of ~ 5900 km s^{-1}, relative to the Lyα-NV emission line. Korista *et al.* (1993) report possible observation of this effect in the spectra of a minority of BALQs.

In attempting to assess the prospects for polarimetry, we should note that the Lyα doublet, which will be encountered first by photons of a given frequency in the AGN frame, has a separation (~ 1 km s^{-1}) much less than the local thermal width. Using the formalism of Paper 1 we can then compute the polarization to be expected after a single scattering through an angle θ. We find that

$$P(\theta) = \frac{3\sin^2\theta}{11 + 3\cos^2\theta} \tag{4.13}$$

which will intermediate between the value $P(\theta) = 3\sin^2\theta/(7 + 3\cos^2\theta)$ for J= $1/2 \rightarrow 3/2$, and the value $P(\theta) = 0$ for J= $1/2 \rightarrow 1/2$. As the optical depth in the Lyα transition is likely to be substantial, we expect that these photons will emerge from their local Sobolev scatterings significantly depolarized. At wavelengths sufficiently close to 1240Å, where the NV resonance can also be encountered, the polarization behavior will be similar to that described in §4.5. As the scattering associated with the Lyα-NV resonances is quite non-local, the expected polarization is quite model-dependent.

4.7 Radiative Mixing of Higher Multiplet Transitions

Although many of the most prominent resonance lines are simple singlets and doublets like those already considered, there are several more complex multiplet transitions and these may also contribute to the net polarization. These lines allow several choices for the total angular momenta of the ground and excited states and the permitted transitions have to be considered collectively. The polarization can be computed according to the principles we have already described although,

there are three complicating factors. Firstly, some multiplet lines have frequency shifts less than the Doppler shifts associated with the ion thermal motion. This means that the ground energy levels are effectively degenerate so that scattering in the different components occurs effectively simultaneously, (as with Lyα), not successively (as with C IV). Secondly, when the ground state angular momentum satisfying $J_g \geq 1$, radiative mixing of the ground sublevels leads to significantly enhanced polarization (*cf.* Paper 1, §4.2) relative to that computed for collisional mixing. Thirdly, in order to compute the radiative mixing correctly, all ground state transitions, not just those in a given multiplet, must be included to derive the distribution of ions among ground state sublevels.

For the common, low Z ions, there are two further cases to consider, beyond Li-like and Be-like ions. Firstly, we consider ions iso-electronic with B atoms, like C^+, N^{++}, O^{3+}. Here, the ground levels are ${}^2P^o_{1/2,3/2}$, with the $J_g = 1/2$ state having the lower energy and the splitting exceeding the Doppler width. The excited states to which excitations are permitted are ${}^2S_{1/2}$, which gives doublets (D′), ${}^2D_{3/2,5/2}$, which gives rise to triplets (T) and ${}^2P_{1/2,3/2}$ which produces quadruplets (Q). All lines are distinct. An important example is the O IV ion where the lines with significant oscillator strength are $\lambda 789(\mathrm{T}), 609(\mathrm{D}'), 554(\mathrm{Q}), 238(\mathrm{T})$. (Only the $\lambda 789$ triplet has been observed in BALQ spectra, Korista *et al.* 1992, Arav, private communication.) The relative frequency of these different excitations depends upon the spectral index, with the longer wavelength transitions being more prominent for steeper spectra.

In Appendix A, we summarize how to compute the polarization under conditions when a multiplet is present and the radiation field is axisymmetric with respect to the outward radial direction. The scattered radiation also exhibits this symmetry and the scattered radiation will only be polarized parallel and perpendicular to the $\mathbf{k} - \hat{\mathbf{r}}$ plane. The results are expressed as a scattering matrix that relates the polarization state of the scattered radiation to the polarization of the incident photons. We have computed the polarization in the various O IV multiplet transitions assuming an isotropic expansion of variable optical depth. We

find that as a consequence of the interplay between the different transitions, the population of the ground state sublevels is closer to statistical than in the simple (and fictitious) two level ions considered in Paper 1. This reduces the net observed polarization.

The incident radiation field is assumed to be given by a power law

$$F_\nu \propto \nu^{\alpha+1}. \tag{4.14}$$

We consider two cases $\alpha = 1,\ 3$. Most of multiplet transitions are not highly polarized. In the case of doublet D′ no polarization is obtained because the excited state sublevels are always populated evenly so that isotropic reemitted radiation field results. The highest polarization is shown in the triplet transition (T) where $p \lesssim 0.01$. Figs. 8(ab) show the result for a range of optical depths.

The second case that we must consider involves ions isoelectronic with C atoms, like N^+ and O^{++}. Here the ground state is ${}^3P^o_{0,1,2}$. One possible excited state is ${}^3S_1$, which produces triplets (T'). Another possible excited state is ${}^3P_{0,1,2}$ which gives six transitions (H) satisfying the selection rules. However, it turns out that the $J_e = 1, 2$ energy levels are effectively degenerate and only four distinct lines are formed. The final case is ${}^3D_{1,2,3}$ where again there are six possible transitions and the degeneracy of the $J_e = 1, 2$ states reduces the number of lines to four.

An important example of this set of transitions is provided by O^{++}. Here the important lines are $\lambda 835(H'), 703(H), 508(T'), 305(H')$ of which the first two lines have been reported. We have again computed the emergent polarization assuming an axisymmetric radiation field and an isotropic expansion and the results for the shifted hexaplet (H′) are shown in Figs.8(cd). The other multiplet transitions yield much lower polarization. Shifted hexaplet (H′) shows the highest polarization, up to $p \sim 0.01$

There is one final possible complication that we have chosen not to consider and this is that there may be significant scattering from ions in metastable excited

states. In particular, if the UV spectrum is sufficiently hard, the rate of photoionisation from the ground state can be as large as ~ 0.2 of the excitation rate. The subsequent recombination may leave the ion in a state with a different value of S. In the case of O^{3+}, there are no permitted transitions from states with $S = 3/2$ to states with $S = 1/2$ and so recombination into a state with $S = 3/2$ will be followed by a cascade down to a metastable state. In a sufficiently tenuous gas where collisional de-excitation can be ignored (as will generally be the case for BALQ flows), the fraction of ions in the metastable state will be given roughly by the ratio of the photionisation rate to the A-value for the intercombination line. In the case of O^{3+}, $A_{intercomb} \sim 2 \times 10^3$ s^{-1}. We estimate the ratio of the strength of the intercombination line to the permitted lines to be $\sim 0.1(\alpha = 1)$, $\sim 0.01(\alpha = 3)$, and so it should not seriously alter the ground state sublevel populations. (A quantitative measure of the importance of intercombination transition is provided by observation of permitted transition from the metastable state. Interestingly, tentative evidence for such a transition in O^4+ has been presented by Korista *et al.* 1992.)

5. GLOBAL OUTFLOW MODELS

We next turn to considering global models in which there is a large scale flow so that photons that emerge along a particular direction can have their last scattering anywhere along a particular extended Sobolev surface parametrized by their Doppler shift. We assume that photons originate within a compact central continuum source located at the origin and propagate outward until they encounter a Doppler surface where the frequency in the rest frame of the gas equals the natural frequency of the resonance transition. At this point they are scattered into a direction and with a polarization determined probabilistically by the local Sobolev optical depth and the velocity gradient tensor. The scattered photons are then allowed to scatter again if they encounter additional resonant surfaces as they emerge from the nucleus. In this manner, the photons incident upon the

Sobolev surface corresponding to the final scattering can arrive from a variety of directions and so the observed polarization can be diminished.

Our approach is similar in many respects to that of Hamann *et al.* (1993). However, there are three important innovations. Firstly, by using a Monte-Carlo approach, we can track the polarization. Secondly, we consider non-radial flow fields which allow non-monotonic velocity variation along a line of sight despite steady expansion along a given streamline. Thirdly, we also allow for the presence of angular momentum which as we shall see introduces some important kinematic changes (*cf.* Murray *et al.* 1995).

5.1 Disk and Conical Wind

As a first example and as a check on our code, we consider the kinematic model proposed by Hamann *et al.* (1993) who calculated the line profiles formed in conical or disk-like winds with radial velocity law $v_r \propto r^\gamma$, where $\gamma = 1$. This is similar to the isotropic expansion prescription considered above. The optical depth prescription, which Hamann *et al.* introduced and we adopt, is given by a function of radial velocity which has the maximum value 2 for velocities 4000 km s^{-1} – 6000 km s^{-1} and the covering factor is $q = 0.25$. Hamann *et al.* used the escape probability formalism to construct line profiles. As a check on our formalism, we reproduce their total intensity distributions using our Sobolev-Monte Carlo approach and, in addition, compute the degree of polarization for the transition J= 0 $\rightarrow$ 1 (Figs. 9).

The incident continuum is assumed to be unpolarized and hence the polarization is solely due to the scattered component, which is shown by the dotted lines. The scattered component is approximately symmetric with respect to the line center and the polarized flux shows similar symmetry. This approximate symmetry is explained by the low optical depth $\tau \lesssim 2$ adopted in this problem, where single scattering dominates. However, the degree of polarization is fairly large (~ 0.1) in the absorption trough since the ratio of the scattered component to the transmitted continuum component is significantly higher than that in the emission part.

The polarization direction is parallel to the projected disk axis, confirming that the polarized flux is dominated by side-scattering.

In Fig. 9b the disk wind with angular momentum is considered. The velocity field is given by $\mathbf{V} \propto [r\hat{r} + A\hat{\phi}/(r\sin\theta)]$, where A is constant. A is chosen to satisfy $V_\phi/V_r = 0.2$ at the point where $V_r = 18,000$ km s^{-1}, $\theta = \pi/2$. The addition of an azimuthal velocity component introduces an additional Doppler shift to the scattered photons, so that a different absorption trough is obtained. The dramatic reduction of the degree of polarization implies that the photons filling in the trough originate from the parts of the disk having angles larger than or smaller than 90° with the observer's line of sight.

Fig. 9c shows the result for a conical wind with the same covering factor as in the disk wind case. A similar absorption profile is obtained. However the degree of polarization in the absorption trough is small (~ 0.02) compared to the case of disk wind. This is due to the dominance of forward scattering.

When an azimuthal component is introduced into this conical wind (*cf.* Fig. 9d) there is little difference in polarization from the purely poloidal flow as in Fig. 9c. This is explaiined by the fact that the azimuthal motion does not affect the forward scattering which is responsible for the dominant polarized flux in the conical wind.

5.2 Equatorial Flow

For our second, global model we consider an equatorial flow where the BAL material accelerates on hyperboloid surfaces to an asymptotic speed which is inversely proportional to the square root of the radius of the foot point of the flow (*cf.* Appendix A). We consider both purely poloidal flow and flow with an azimuthal component. Fig. 10 shows a truncated section of a Sobolev surface for a flow with angular momentum for an observer lying on $x - z$ plane with colatitude $\theta_o = \pi/3$. The viewpoint is the observer's line of sight and the illuminated side is the part lying in $-x$ direction from the central continuum source. Unlike Hamann *et al.* 's model considered in the preceding section, scatterers are not confined to a

region with a small covering factor but flow throughout a large volume in a manner that conserves mass. In this model, the optical depth increases toward the equatorial plane so that the Sobolev surface with moderate optical depth ($\tau_{Sob} \gtrsim 1$) is only present at low latitude (See also Appendix A). It is more likely that the absorbing clouds expand as they flow radially outward which would tend to decrease the Sobolev optical depth as a function of blue-shift.

The radial velocity component along the line of sight has a minimum near the center, which corresponds to the sharp cutoff at the broad absorption trough in the line profile. The Sobolev optical depth along the radial direction is much larger than 1 when $\mu = \cos\theta \to 0$ and much less than 1 as $\mu \to 1$.

Fig. 11a shows the polarization that results from a purely poloidal flow, simulated using 10^7 photons. The parameters are chosen so that the Sobolev optical depth $\tau_{Sob} = 1$ at $-\Delta V = 1.7 \times 10^9 \mathrm{cm\ s^{-1}}$ in the direction $\mu = 0.2$. Here, the maximum degree of polarization in the absorption trough is ~ 0.5, which results from side-scattering at low latitude. The polarized flux ratio defined in the preceding section is $R_P \sim 0.03$ in this case. Outside the trough, the radiation is unpolarized. The negative degree of polarization signifies that the electric vector is parallel to the symmetry axis. The maximum degree of polarization coincides with the deepest absorption of the line because the unpolarized transmitted component contributes least here. However, the polarized flux extends to the red-side with peak value located in the blue-side near the line center. A closer look at the polarized flux also reveals a slight asymmetry with respect to the peak, which is reminiscent of the asymmetry encountered in the local analysis. It should be noted that the positions of peak values do not necessarily coincide with the position of the deepest absorption trough.

We next add azimuthal motion (Fig. 11b). The same parameters were chosen as in the case of purely poloidal flow and the constant specifying the azimuthal component (B in Eq. A3) is chosen to be 5. This shifts the negative polarization into higher $\Delta\nu$, where positive polarization dominates. The addition of azimuthal motion generally reduces the degree of polarization and the polarized

flux. When the azimuthal component of the flow dominates the radial component, then the side-scattering gains large Sobolev optical depth toward the observer's line of sight, whereas the forward scattering is relatively less affected by azimuthal component. This leads to a change in the polarization direction. However, it should be emphasized that the polarized flux is much smaller than that in the case of purely poloidal flow. The absorption trough gets deeper because reduced number of photons scattered sideways fills in the trough, which also explains the decreased polarized flux.

In Figs. 11cd, the results from the transition J= 1/2 $\rightarrow$ 1/2, 3/2 doublet case for a purely poloidal flow and a flow with angular momentum, where the multiplet separation is assumed to be much larger than the local thermal velocity. The largest degree of polarization from the purely poloidal flow is ~ 0.15 at the absorption trough, and the polarized flux ratio is $R_P \sim 0.008$. Apparently the contribution of unpolarized J= 1/2 $\rightarrow$ 1/2 photons is not large in this case. Again the addition of angular momentum leads to reduced polarized flux and in the case of high angular momentum case polarization direction changes. The peak value for the degree of polarization in this case is ~ 0.1, but the polarized flux is no larger than 0.1 % that of the unpolarized continuum flux.

5.3 Bipolar Flow

Finally, we consider another simple poloidal flow where the BAL material moves on a family of paraboloidal level surfaces. Fig. 12 shows a truncated part of a Sobolev surface for a purely poloidal flow seen from the observer lying in $x - z$ plane with colatitude $\pi/3$. The Sobolev optical depth is calculated in a similar way described in the previous section. In this flow, however, the density function is chosen to be $n(\xi_2) \propto \exp(1/\xi_2)$ (See Appendix B), which gives large optical depth to the jet-direction. Here, the adopted velocity law gives a monotonically increasing velocity along the flow line but decreasing velocity along the radial line of sight from the central source to the observer. Hence, in contrast to the equatorial flow considered in the previous section, photons making the transition

J=1/2 $\rightarrow$ 1/2 hit the Sobolev surface first and then possibly they can be scattered at the second Sobolev surface associated with the transition J=1/2 $\rightarrow$ 3/2.

The numerical results are shown in Figs. 12. In this bipolar flow case, the direction of polarization is perpendicular to the projection of the disk symmetry axis. The degree of polarization of the purely poloidal flow is $\sim$ 0.15, 0.05 for J=0 $\rightarrow$ 1 transition and J=1/2 $\rightarrow$ 1/2, 3/2 doublet respectively. The polarized flux ratios of $R_P \sim 0.02,\ 0.005$ are obtained from the two cases respectively. The low degree of polarization and the polarized flux compared with the counterparts of an equatorial flow may be attributed to the dominance of forward scattering over side-scattering. Different polarization behavior between the J=0 $\rightarrow$ 1 singlet transition and the J=1/2 $\rightarrow$ 1/2, 3/2 doublet transition is attributed to the different Sobolev structures. Again, we consider the effects of azimuthal motion. Contrary to the equatorial flow, the degree of polarization changes little when angular momentum is introduced into the flow. This is explained by the fact that the azimuthal motion does not affect the forward scattering which is also shown in the conical model discussed in the previous section. Since back-scattering is not important for the bipolar flow, the polarized flux is concentrated on the blue side, where absorption occurs. However, if the obsever lies at low latitude, then the backscattering may not be negligible. In this way bipolar flow can be distinguished from equatorial flow.

6. OBSERVATIONAL RAMIFICATIONS

In the §2, we introduced a generic model for line formation by radio-quiet quasars involving a compact continuum source, a broad emission line region and a scattering outflow. In §3,4, we have discussed how spectropolarimetry can elucidate the geometrical and kinematical organization of these three components. We will now summarize what we have learnt from recent observations and outline some immediate possibilities for furthering our understanding of quasar line formation.

6.1 Interpretation of Recent Spectropolarimetric Observations

The spectropolarimetric database for radio-quiet quasars is sparse. The brightest example of a BALQ, PHL 5200 was first observed in this manner by Stockman *et al.* (1981). More recently, Glenn *et al.* (1994) have presented observations of CSO 755 and Cohen *et al.* (1995) report upon Keck/Palomar data from PHL 5200 and 0105-266.

It appears that BALQs exhibit a modest ($p_C \lesssim 3$ percent), continuum polarization that varies at most slowly in wavelength and constant position angle. Prominent UV emission lines, by contrast, appear to be unpolarized at about the ~ 0.5 percent level. A possible exception is C III] λ1909 which Cohen *et al.* found to exhibit 1.3 percent polarization in PHL5200 in the same direction as the electron scattering (See also Goodrich & Miller 1995). If this pattern is verified by further observation, it will provide support for the standard model of emission line regions in which the emitting gas moving at a given velocity occupies discrete contiguous regions (or clouds) in phase space each with large resonance line optical depths. Exterior to these clouds, though, the BELR is optically thin at a given velocity along most lines of sight. Based on our calculations in §3, we estimate that the mean optical depth at a given velocity in small clouds is $\lesssim 0.1$, which translates into a column density limit $N_H \lesssim 10^{19}$ cm^{-2} for gas moving with speed $\lesssim 10,000$ km s^{-1} of the line center, constraining the model of Shields *et al.* (1995). By contrast, a weak polarization in the C III] line was predicted in Paper 2 on the grounds that the optical depth within a single emission line cloud was uniquely low ($\tau \sim 1 - 10$) and that therefore this line should be emitted with a measurable polarization.

In the BALQs, PHL5200, 0105-266, it appears that the absorption line troughs are less deep in polarized flux and the degree of polarization can reach $p_C \sim$ 12 percent at intermediate velocity within the absorption trough (*cf.* Cohen *et al.* 1995). More relevantly, the ratio of the polarized flux in the troughs to the continuum flux well removed from the line is typically $F_P/F_C \sim 0.01 - 0.02$. The direction of the trough polarization vector is also apparently along the same

direction as that of the continuum polarization. Although there appears to be velocity structure in the line polarization, it is not possible to decide whether or not there is additional polarization associated with the red wings of the emission line.

Fortunately, there are good prospects for resolving some of these uncertainties. High dispersion spectroscopy in the vicinity of selected prominent resonance lines, combined with an atlas of weak lines, should enable a careful continuum level to be constructed. Let us suppose that we can define a continuum from the measured flux for $|V| \gtrsim 30,000$ km s^{-1}. It should then be possible to define a line profile, perhaps including very broad wings that may comprise scattered resonance line radiation. If we further assume that there is only significant absorption in the blue wing, then it should be possible to subtract the line polarization so as to determine the polarized contribution to the line flux at wavelengths blueward of any absorption trough. Finally, if the absorption is strong, then the measured radiation in the trough is probably scattered and its polarized flux can be measured.

As we have already emphasized, scattering of line radiation can take two forms, electron scattering and resonance line scattering and they are probably both present. Cohen *et al.* (1995) interpret their observations in terms of a simple model in which a minority of continuum photons are Thomson-scattered along a higher altitude ray so that they are less attenuated by the outflowing BAL gas than the unscattered, direct radiation. This explanation accounts naturally for the constancy of the polarization direction. However, the free electrons probably have to be co-spatial with the emission line clouds, so that the emission lines emerge unpolarized.

Alternatively, adopting the standard interpretation of BALQ (*cf.* also Hamann *et al.* 1993, Cohen *et al.* 1995), we can assume that a fraction $q_{BALR} \sim 0.1$ of the continuum photons with frequency in the interval $\sim 1.03 - 1.1\nu_0$ of a prominent resonance line of frequency ν_0, are scattered by outflowing gas. These photons escape along different directions, possibly encountering other resonant Sobolev surfaces along the way and being rescattered. A minimum equivalent width for

the resonance-scattered radiation, $W_\lambda \sim \lambda_0 q_{BALR} \Delta V_{BALR}/c \sim 10$ Å averaged over direction, seems unavoidable. Taking into account all the uncertainties, this is not inconsistent with the fluxes typically measured in absorption troughs.

As discussed in §4, three features determine the contribution to the polarized flux in a given line from an element of suitably ionized outflowing gas. Firstly, the component of velocity resolved along the line of sight dictates the Doppler shift. Hence, the prevalence of blue-shifted absorption points to a general outflow. Secondly, the scattering angle dictates the degree of polarization; side scattering is highly polarized; forward and backward scattering exhibit low polarization. The diminishing degree of polarization observed at the blue end of the trough is then consistent with a flow that accelerates to move along the line of sight. Thirdly the local velocity gradient tensor determines the optical depth and its variation with direction. If the optical depth $\tau \gtrsim 1$, photons escape most readily along directions where the velocity gradient is largest. For the doublet transitions, this allows photons to be scattered sideways with substantial polarization in a slowly accelerating but expanding flow and to escape extreme depolarization in the J= $1/2 \rightarrow 1/2$ resonance at modest optical depth. The similarity of the polarization direction in both the continuum and the trough constrains the model. In a bipolar outflow model (*e.g.* Hes 1995), the continuum must be polarized perpendicular to the symmetry axis, in an equatorial outflow model the polarization direction will be parallel.

To be quantitative, the simulations presented in §4 show that a typical equatorial outflow with no angular momentum gives a polarized flux ratio $R_P \sim$ 0.03, 0.01, and degree of polarization in the absorption trough $\sim$ 0.5, 0.15 for a singlet J=0 $\rightarrow$ 1 and a doublet J=1/2 $\rightarrow$ 1/2, 3/2 transition respectively. The polarized flux extends to the redside because of backscattering. From a bipolar flow the polarized flux ratio is typically found to be $\sim$ 0.02, 0.005 for the singlet and the doublet transitions respectively. The degree of polarization can reach up to $\sim$ 0.15, 0.1 correspondingly. The polarized flux, however, is prominent only on the blue side of the line.

6.2 Kinematical Inferences

Assuming that resonance scattering contributes to the flux in the absorption line troughs, we can use polarization observations to decide whether this scattered flux is present in the emission line and its redward extension as might be expected if receding gas is directly observable. If so, this would support an equatorial outflow model. However, if there are bipolar jets launched from an optical thick accretion disk then only the approaching component will be seen and excess polarized flux should only be measured in the line's blueward extension.

The actual shape of the absorption trough, which varies from line to line and object to object, also contains kinematic information. Its smoothness implies that the absorbing gas either comprises a continuous wind flow as in the model of Murray *et al.* (1995) or many clouds as in the model of *e.g.* Arav & Begelman (1994). If we adopt a covering solid angle for the BAL gas $\Omega_{BALR} \sim 1$ sterad and a total BAL column $\sim 3 \times 10^{20}$ cm^{-2}, then the wind discharge in a typical quasar with $L_{46} \sim 1$ is bounded by $\dot{M} \gtrsim 0.03(R_{BALR}/1\mathrm{pc})$ M$_\odot$ yr^{-1}. If the troughs are partially filled with scattered radiation then this will automatically lead to a smooth profile as long as the lines are totally absorbing. With a thermal velocity dispersion in the absorbing gas ~ 10 km s^{-1}, this requires at least 3000 individual clouds along a line of sight. If these clouds are freely expanding then, whatever their initial size, they will expand to become almost contiguous in phase space (*i.e.* they will form a wind) as they double their radius. One difficulty with a wind model (addressed by Murray *et al.* 1995) is that the ionization parameter will be $U \sim 10^6 L_{46} R_{pc}^{-1}$, orders of magnitude larger than the value generally supposed for the range of ionization states observed in absorption. If the clouds are confined so as to maintain $U \sim 0.1$, then their characteristic sizes will be extremely small, $\lesssim 10^8 R_{pc}^2 L_{46}^{-1}$ cm.

6.3 Dynamical Considerations

The very presence of absorption line troughs informs us that momentum is removed from the radiation field by the accelerating gas (*e.g.* Weymann *et al.* 1982).

If we ignore a slight correction for preferential back-scattering, then the radial acceleration of a fluid element is

$$g_{rad} = \left[V\frac{dV}{dr}\right]_{tot} \sum_{\ell} \frac{\nu_\ell F_{\nu_\ell}}{Jc^2}\left(1 - e^{-\tau(\nu_\ell, V)}\right), \tag{6.1}$$

where $\nu_\ell F_{\nu_\ell}$ is the radiative flux per $\ln \nu_\ell$ for each contributing line and J is the mass flux (*cf.* Arav & Begelman 1994). Eq. (5.1) has the implication that if there are no significant non-radiative forces and the flow is purely radial, then

$$\sum_{\ell} \nu_\ell L_{\nu_\ell \Omega}\left(1 - e^{-\tau_\ell(\nu_\ell, V)}\right) = \dot{M}_\Omega c^2, \tag{6.2}$$

where the subscript Ω denotes a quantity per sterad. This is just an expression of momentum conservation. It is not clear how much radiative acceleration is associated with the far UV (Korista *et al.* 1992). However, on the basis of this simple estimate, we can bound the mass discharge in a purely radiatively driven flow

$$\dot{M} \lesssim 10^{-2} L_{46} \Omega_{BALR} \mathrm{M}_\odot \mathrm{yr}^{-1}. \tag{6.3}$$

In order to have enough column density to produce deep troughs then requires that $R \lesssim 10^{17} L_{46} \Omega^{-1}$ cm. This is smaller than the estimated size of the BELR. Although none of these estimates can be regarded as secure at this stage, it is clearly worth considering alternative accelerating agents such as cosmic rays (Begelman, de Kool & Sikora 1991), dust acceleration (Scoville & Norman 1995), thermal pressure (Weymann *et al.* 1982) and magnetic field (EBS).

6.4 Continuum Polarization

A longstanding puzzle concerning continuum observations of quasars is the low value observed for the linear polarization in the optical and UV continuum. In most cases the polarization is found to be $\sim 1-3$ percent (Stockman *et al.* 1979). Furthermore, in the case of radio-loud objects, the polarization direction is often found to be aligned parallel to the radio source axis. This behavior is in marked contrast to the expectations of optically thick, geometrically thin accretion disk

models, which usually have an electron scattering atmosphere that ought to impose a polarization perpendicular to the symmetry axis with a degree that can be as large as 12 percent, dependent upon the observer's latitude and the relative importance of absorptive and scattering opacity (eg Laor *et al.* 1990).

One way of reconciling these observations with the theoretical expectation of a disk flow is to suppose that accretion disks contain strong magnetic fields that can Faraday depolarize the emergent radiation. In order for this to occur, there must be a few radians rotation of the plane of polarization in the final Thomson scattering optical depth. This will occur for wavelengths longer than

$$\lambda \sim 1000 \left(\frac{B}{1000\mathrm{G}} \right)^{-1/2} \mathring{A}. \tag{6.4}$$

Field strengths as large as $\sim 100 - 1000$ G have been invoked to drive accretion flows close to the black hole. (Note that if the radiation is approximately thermal with an effective temperature $T(r) \sim hc/3\lambda$, then condition (5.1) can be rewritten as a condition that the ratio of the magnetic pressure to the photospheric radiation pressure exceed 0.01, independent of wavelength. Again, this does not seem too difficult to satisfy.) The small wavelength-independent continuum polarization that is observed might be imposed externally through electron scattering, or it might be a limiting polarization from the disk atmosphere.

In a remarkable recent observation, Koratkar *et al.* (1995) (*cf.* also Impey *et al.* 1994) have used Hubble Space Telescope to measure polarization blueward of the Lyman continuum and find that it increases to a value $\sim 10 - 20$ per cent. Curiously, this apparent edge in the polarized flux is not matched by an edge in the total flux. It seems simplest to attribute this radiation to an increasing fraction of non-thermal synchrotron emission from a corona to thermal radiation from the disk with decreasing radius and increasing frequency (*cf.* Rauch & Blandford 1992). In this case, the strong differential rotation is likely to produce a toroidal magnetic field and a polarization vector parallel to the symmetry axis.

6.5 Unification and Grand Unification

The, by now, standard and unifying explanation for the difference between types 1 and 2 Seyfert galaxies is that they are similar types of AGN, the former viewed at high latitude and the latter at low latitude so that the central continuum source and BELR are obscured by an orbiting torus. The broad permitted lines from Seyfert 2 nuclei are then supposed to be formed through reflection by free electrons at high latitude. This model is consistent with the observation that the polarization direction in Seyfert 2 galaxies is typically perpendicular to the projected radio source axes in contrast to the situation in Seyfert 1 galaxies where the polarization direction is parallel.

Now, although a few Seyfert galaxies exhibit comparatively narrow, blue-shifted absorption lines, there are no cases where lines as broad as 30,000 km s^{-1} are seen. It is therefore not certain how to relate BALQ to their lower power, Seyfert counterparts. If we adopt the equatorial outflow model and suppose that they are related to the Seyfert2 galaxies, then the fact that the polarization direction is maintained through the trough suggests that, if there is resonance line scattering, then the polarization direction is perpendicular to the projected source symmetry axis opposite to the prediction of the models. Conversely, if we suppose that BAL are bipolar outflows driven by radiation pressure in very powerful ionization cones, (*e.g.* Wilson 1995) and that we only see the approaching jet, then the polarization will be perpendicular to the source axis, consistent with the models.

Theories of grand unification strive to relate radio-loud to radio-quiet sources. One of the most striking properties of BALQs is that they appear to be completely absent among radio-loud objects. If the outflow turns out to be equatorial, then we should probably interpret this absence by deducing that it originates at such a small radius that it precludes the existence of a polar jet. If the BAL outflow turns out to be polar, then this will probably indicate that the jet speed is too low for there to be highly efficient acceleration of relativistic electrons as is the case in expanding supernova remnants. The formation of relativistic jets may require the presence of a rapidly spinning black hole and the absence of a central cluster of

mass-losing stars (*e.g.* Perry & Williams 1993, Blandford 1994, Scoville & Norman 1995), both long-lived characteristics of a galactic nucleus. It is therefore to be expected that radio-loud quasars should not exhibit polarized resonance scattering like their radio-quiet counterparts.

6.6 Observational Tests

We conclude by summarizing the principal observational tests that can be used to diagnose BALQs. Firstly, one of our basic hypotheses-that the continuum is uniformly polarized-can be substantiated through measuring the polarization in several more objects and over a broader range of wavelength. Secondly, high dispersion spectroscopy can be used to measure line profiles in both radio-quiet quasars and BALQ. It will be of particular interest to determine if the line wings are intrinsically irregular or smooth. If they are irregular, then this will rule out the presence of a strong scattering component. If, however, they are smooth and symmetric, then this may point to an electron scattering origin. By contrast, broad, smooth yet asymmetric wings are a signature of resonance line scattering. The net equivalent width of the resonance scattering component may be as much as ten percent of the full line equivalent width and the velocity width as much as 30,000 km s^{-1}. A particularly intriguing example is provided by the Mg II BALQ MRK 231 (Smith *et al.* 1995). Thirdly, if there is evidence for resonance line scattering in both radio-quiet quasars and BALQ, then, in the former case, the polarization of the emission lines can be measured in more objects to verify that they are generally unpolarized (excepting semi-forbidden lines) but possess broad wings of polarized flux. The effect should be much stronger in singlet J= $0 \rightarrow 1$ lines than in the more common doublet transitions. The singlet lines expected to be prominent in absorption include C III 977, N IV λ765, O V λ630, Mg I λ2853, Al II λ1671, and Si III λ1207 (*cf.* Verner *et al.* 1994). Finally, and this is the key result of this paper, if a resonance-scattered component can be detected, through either its total or, more convincingly, through its polarized flux, then it should be a good diagnostic of the overall disposition of gas in the nucleus of the quasar

(*cf.* Hamann *et al.* 1993). If only blue-shifted resonance line radiation is seen in BALQ, then this will be consistent with a bipolar jet model (which we observe from close to the jet axis). Alternatively, if the resonance scattered radiation extends into the red wing of BALQ, then this will be compatible with the more widely-supported equatorial outflow model. Similar fluxes of partially polarized scattered resonance line radiation should be seen in non-BAL radio-quiet quasars where the line of sight does not intercept the scattering gas. A more detailed analysis of the polarized line profile might reveal rotation in the outflow. Most interesting of all, though, would be the failure to detect any evidence of resonance-scattered radiation which may call into question the standard interpretation of quasar broad absorption lines.

ACKNOWLEDGEMENTS

We are indebted to several colleagues, notably Ski Antonucci, Nahum Arav, Marshall Cohen, Bob Goodrich, Ari Laor, Norm Murray, Patrick Ogle, and Ray Weymann for invaluable discussions and helpful suggestions. Support under NSF grant AST 92-23370 is gratefully acknowledged.

APPENDIX A POLARIZATION SCATTERING MATRIX

In this appendix, we describe how to compute the scattering matrix for scattering of polarized radiation when the radiation field is axisymmetric with respect to the direction $\hat{\mathbf{r}}$. We assume radiative mixing of the ground sublevels when $J_g \geq 1$. Let the incident photons be characterized by the wave vector $\mathbf{n}_i = (\sin\theta_i \cos\phi_i, \sin\theta_i \sin\phi_i, \cos\theta_i)$ and polarization vector $\mathbf{e}^i_\alpha$, where $\alpha = \|, \perp$, parallel and perpendicular to the $\hat{\mathbf{r}} - \mathbf{n}_i$ plane.

Adopting the notation of Paper 1, the matrix elements are given by

$$\begin{aligned} M_{eg}(\mathbf{e}^i_\|) &= [2^{-1/2}\cos\theta_i e^{i\phi_i} R^{-1}_{eg}, -\sin\theta_i R^0_{eg}, -2^{-1/2}\cos\theta_i e^{-i\phi_i} R^1_{eg}] \\ M_{eg}(\mathbf{e}^i_\perp) &= [2^{-1/2} i e^{i\phi_i} R^{-1}_{eg},\ 0,\ 2^{-1/2} i e^{-i\phi_i} R^1_{eg}]. \end{aligned} \tag{A.1}$$

We now expand our basis eigenstates with respect to $\hat{\mathbf{r}}$ so that both the ground and excited density matrices will be diagonal and we write the ground state occupation probabilities as ρ_g, $-J_g \leq g \leq J_g$, normalized so that $\sum_g \rho_g = 1$. (Note that $\rho_g = \rho_{-g}$.) In equilibrium, the excited state occupation probabilities are given by

$$\tilde{\rho}_e = \int d\Omega_i \sum_{\alpha g} \mathcal{N}_\alpha M_{eg}(\mathbf{e}^i_\alpha) \rho_g M^*_{eg}(\mathbf{e}^i_\alpha), \tag{A.2}$$

where $d\Omega_i = \sin\theta_i d\theta_i d\phi_i$ and $\mathcal{N}_\alpha$ is the photon occupation number (assumed $<< 1$). Averaging over azimuth, this becomes

$$\begin{aligned} \tilde{\rho}_e = (\frac{1}{2}\cos^2\theta_i \mathcal{N}_\| + \mathcal{N}_\perp)|R^1_{ee-1}|^2 \rho_{e-1} \\ + \sin^2\theta_i \mathcal{N}_\| |R^0_{ee}|^2 \rho_e \\ + (\frac{1}{2}\cos^2\theta_i \mathcal{N}_\| + \mathcal{N}_\perp)|R^{-1}_{ee+1}|^2 \rho_{e+1}. \end{aligned} \tag{A.3}$$

The scattered radiation field is given by

$$j_{\alpha\alpha'} = \sum_{e,g} M^*_{eg}(\mathbf{e}^o_\alpha) \tilde{\rho}_e M_{eg}(\mathbf{e}^o_{\alpha'}), \tag{A.4}$$

where the outgoing wavevector is given by $\mathbf{n}_o = (\sin\theta_o \cos\phi_o, \sin\theta_o \sin\phi_o, \cos\theta_o)$. The direct substitution of Eq.(A.3) into Eq.(A.4) and averaging over the azimuth

ϕ_o gives

$$
\begin{aligned}
j_{\parallel\parallel} &= \sum_e \left[\frac{1}{2}\cos^2\theta_o\{(R^{-1}_{ee+1})^2 + (R^1_{ee-1})^2\} + \sin^2\theta_o (R^0_{ee})^2\right] \\
&\times \left[\frac{1}{2}(\mathcal{N}_\parallel \cos^2\theta_i + \mathcal{N}_\perp)\{C_{e+1}(R^{-1}_{ee+1})^2 + C_{e-1}(R^1_{e-1}(R^1_{ee-1})^2\}\right. \\
&\left. + \mathcal{N}_\parallel \sin^2\theta_i C_e (R^0_{ee})^2\right] \\
j_{\perp\perp} &= \sum_e \frac{1}{2}\{(R^{-1}_{ee+1})^2 + (R^1_{ee-1})^2\} \\
&\times \left[\frac{1}{2}(\mathcal{N}_\parallel \cos^2\theta_i + \mathcal{N}_\perp)\{C_{e+1}(R^{-1}_{ee+1})^2 + C_{e-1}(R^1_{ee-1})^2\}\right. \\
&\left. + \mathcal{N}_\parallel \sin^2\theta_i C_e (R^0_{ee})^2\right] \\
j_{\parallel\perp} &= j_{\perp\parallel} = 0.
\end{aligned}
\tag{A.5}
$$

From Eq.(A.5) we obtain the scattering matrix S, defined by the relation

$$
\begin{pmatrix} J_\parallel \\ J_\perp \end{pmatrix} = S \begin{pmatrix} n_\parallel \\ n_\perp \end{pmatrix}, \tag{A.6}
$$

where $J_\parallel \equiv j_{\parallel\parallel}$, and similarly for $J_\perp$.

The elements of S are given by

$$
\begin{aligned}
S_{\parallel\parallel} &= \sum_e \left[\frac{1}{2}\cos^2\theta_o\{(R^{-1}_{ee+1})^2 + (R^1_{ee-1})^2\} + \sin^2\theta_o (R^0_{ee})^2\right] \\
&\times \left[\frac{1}{2}\cos^2\theta_i\{C_{e+1}(R^{-1}_{ee+1})^2 + C_{e-1}(R^1_{ee-1})^2\}\right. \\
&\left. + \sin^2\theta_i C_e (R^0_{ee})^2\right] \\
S_{\parallel\perp} &= \sum_e \left[\frac{1}{2}\cos^2\theta_o\{(R^{-1}_{ee+1})^2 + (R^1_{ee-1})^2\} + \sin^2\theta_o (R^0_{ee})^2\right] \\
&\times \frac{1}{2}\{C_{e+1}(R^{-1}_{ee+1})^2 + C_{e-1}(R^1_{ee-1})^2\} \\
S_{\perp\parallel} &= \sum_e \frac{1}{2}\{(R^{-1}_{ee+1})^2 + (R^1_{ee-1})^2\} \\
&\times \left[\frac{1}{2}\cos^2\theta_i\{C_{e+1}(R^{-1}_{ee+1})^2 + C_{e-1}(R^1_{ee-1})^2\}\right. \\
&\left. + \sin^2\theta_i C_e (R^0_{ee})^2\right] \\
S_{\perp\perp} &= \sum_e \frac{1}{2}\{(R^{-1}_{ee+1})^2 + (R^1_{ee-1})^2\} \\
&\times \frac{1}{2}\{C_{e+1}(R^{-1}_{ee+1})^2 + C_{e-1}(R^1_{ee-1})^2\}.
\end{aligned}
\tag{A.7}
$$

Noting the relations

$$(R^{-1}_{ee+1})^2 = (R^{1}_{-e\ -e-1})^2 \tag{A.8}$$

$$(R^{0}_{ee})^2 = (R^{0}_{-e\ -e})^2, \tag{A.9}$$

we obtain simpler relations

$$\begin{aligned}
S_{\|\|} &= \sum_e \left[\frac{1}{2}\cos^2\theta_o\{(R^{-1}_{ee+1})^2 + (R^{1}_{ee-1})^2\} + \sin^2\theta_o(R^{0}_{ee})^2\right] \\
&\quad \times \left[\cos^2\theta_i C_{e+1}(R^{-1}_{ee+1})^2 + \sin^2\theta_i C_e(R^{0}_{ee})^2\right] \\
S_{\|\perp} &= \sum_e \left[\frac{1}{2}\cos^2\theta_o\{(R^{-1}_{ee+1})^2 + (R^{1}_{ee-1})^2\} + \sin^2\theta_o(R^{0}_{ee})^2\right] \\
&\quad \times C_{e+1}(R^{-1}_{ee+1})^2 \\
S_{\perp\|} &= \sum_e \frac{1}{2}\{(R^{-1}_{ee+1})^2 + (R^{1}_{ee-1})^2\} \\
&\quad \times \left[\cos^2\theta_i C_{e+1}(R^{-1}_{ee+1})^2 + \sin^2\theta_i C_e(R^{0}_{ee})^2\right] \\
S_{\perp\perp} &= \sum_e \frac{1}{2}\{(R^{-1}_{ee+1})^2 + (R^{1}_{ee-1})^2\} \times C_{e+1}(R^{-1}_{ee+1})^2.
\end{aligned} \tag{A.10}$$

The population of the ground state sublevels after the scattering is given by

$$\begin{aligned}
\tilde{\rho}'_g &= \sum_e \tilde{\rho}_e M^*_{eg}(\mathbf{e}^o_\alpha) M_{eg}(\mathbf{e}^o_{\alpha'}) \\
&= \frac{1}{2}(\cos^2\theta_o + 1)[(R^{1}_{g+1\ g})^2\tilde{\rho}_{g+1} + (R^{-1}_{g-1\ g})^2\tilde{\rho}_{g-1}] \\
&\quad + \sin^2\theta_o(R^{0}_{gg})^2\tilde{\rho}_g.
\end{aligned} \tag{A.11}$$

APPENDIX B: EQUATORIAL FLOW MODEL

We model an equatorial flow using oblate spheroidal coordinates

$$\begin{aligned} x &= d\cosh\mu\sin\lambda\cos\phi \\ y &= d\cosh\mu\sin\lambda\sin\phi \\ z &= d\sinh\mu\cos\lambda \end{aligned} \tag{B.1}$$

setting $\lambda =$ constant along a flow line. For the velocity field, we adopt

$$\begin{aligned} v_p &= \dot{\mu}(\sinh^2\mu + \cos^2\lambda)^{1/2} = A(1/\sin\lambda - 1/r^{1/2}) \\ v_\phi &= \dot{\phi}\cosh\mu\sin\lambda \propto 1/\cosh\mu\sin\lambda = B/r\sin\theta. \end{aligned} \tag{B.2}$$

The equation of a Sobolev surface corresponding to Eq. (A4) is given by

$$\begin{aligned} v_l &= d(\dot{\mu}\sinh\mu\sin\lambda\cos\phi - \dot{\phi}\cosh\mu\sin\lambda\sin\phi)\sin\theta_o + d_0\dot{\mu}\cosh\mu\cos\lambda\cos\theta_o \\ &= \left[\frac{A[r^{1/2} - (d\sin\lambda)^{1/2}]}{[r\sin\lambda(\sinh^2\mu + \cos^2\lambda)]^{1/2}}\right] \\ &(\sinh\mu\sin\lambda\cos\phi\sin\theta_0 + \cosh\mu\cos\lambda\cos\theta_0) \\ &- \frac{B\sin\phi\sin\theta_0}{r\sin\theta}, \end{aligned} \tag{B.3}$$

where $r = d(\sinh^2\mu + \sin^2\lambda)^{1/2}$.

The conserved number flux corresponding to Eq. (A5) is

$$N(\lambda)d\lambda = \pi n(\mu,\lambda)d^3\dot{\mu}\cosh\mu\sin\lambda(\sinh^2\mu + \cos^2\lambda)d\lambda \tag{B.4}$$

and the density is

$$n(\mu,\lambda) = \frac{(r\sin\lambda)^{1/2}\ h(\lambda)}{\pi A d^{3/2}\cosh\mu\sin\lambda(\sinh^2\mu + \cos^2\lambda)^{1/2}\ [r^{1/2} - (d\sin\lambda)^{1/2}]}, \tag{B.5}$$

where $h(\lambda)$ is a function to be specified.

These relations are sufficient to compute the Sobolev optical depth along a ray.

APPENDIX C: BIPOLAR FLOW MODEL

We model a bipolar outflow using a simple model in which the poloidal velocity lies on level surfaces (ξ_2 =constant) of the paraboloidal coordinate system in which

$$\begin{aligned} x =& \xi_1\xi_2\cos\phi \\ y =& \xi_1\xi_2\sin\phi \\ z =& \frac{1}{2}(\xi_1^2-\xi_2^2). \end{aligned} \tag{C.1}$$

We adopt simple, kinematic prescriptions for the poloidal and toroidal velocity components describing an accelerating flow in which mechanical angular momentum is conserved

$$\begin{aligned} v_p &= \dot{\xi}_1(\xi_1^2+\xi_2^2)^{1/2} = A\left[\frac{1}{\xi_2}-\left(\frac{1}{r}\right)^{1/2}\right] \\ v_\phi &= \dot{\phi}\xi_1\xi_2 = \frac{B}{\xi_1\xi_2}, \end{aligned} \tag{C.2}$$

where $r=(\xi_1^2+\xi_2^2)/2$ and A, B are constants.

The equation of a Sobolev surface is given by $\vec{v}\cdot\hat{\mathbf{n}} = v_l$ = constant. Making use of the relations

$$\begin{aligned} \xi_1 =& (r+z)^{1/2} = r^{1/2}(1+\cos\theta)^{1/2} \\ \xi_2 =& (r-z)^{1/2} = r^{1/2}(1-\cos\theta)^{1/2} \end{aligned} \tag{C.3}$$

we obtain

$$\begin{aligned} v_l &= \left(\frac{A}{r^{1/2}}\right)\left[\frac{1-(1-\cos\theta)^{1/2}}{(1-\cos\theta)^{1/2}}\right] \\ &= [(1+\cos\theta)^{1/2}\cos\phi\sin\theta_o + (1-\cos\theta)^{1/2}\cos\theta_o] \\ &\quad - B\sin\phi\sin\theta_o/r\sin\theta, \end{aligned} \tag{C.4}$$

where $\hat{\mathbf{n}} = (\sin\theta_o, 0, \cos\theta_o)$. This can be solved as a quadratic for $r^{1/2}$.

Since ξ_2 =constant along a streamline, the number flux across the surface z = constant with ξ_2 in $d\xi_2$ must be independent of ξ_1 satisfies

$$N(\xi_2)d\xi_2 = n(\xi_1,\xi_2)\dot{\xi}_1\xi_1\xi_2(\xi_1^2+\xi_2^2)d\xi_2. \tag{C.5}$$

Hence

$$n(\xi_1,\xi_2) = \sqrt{1-\cos\theta}f(\xi_2)/[\sqrt{2}A_v r\sin\theta(1-\sqrt{1-\cos\theta})], \tag{C.6}$$

where $f(\xi_2)$ is a function to be specified.

REFERENCES

Antonucci, R. R. J., & Miller, J. S. 1985. *Ap. J.*, **297**, 621.

Arav, N., Li, Z. Y., & Begelman, M. C. 1994. *Ap. J.*, **432**, 62.

Barlow, T. A. *et al.* 1992. *Ap. J.*, **397**, 81.

Barlow, T. A., & Junkkarinen, V. T. 1995. . Begelman, M. C., de Kool, M., & Sikora, M.91Ap. J.382416

Blandford, R. D. 1994. *Astrophys. J. Suppl.*, **90**, 515.

Cohen, M. H. *et al.* 1995. *Ap. J. Lett.*, in press.

Corbin, M. R., & Francis, P. J. 1994. *Astronom. J.*, **108**, 2016.

Emmering, R. T., Blandford, R. D., & Shlosman, I. 1992. *Ap. J.*, **385**, 460. (EBS)

Goodrich, R. W. & Miller, J. S. 1994. *Ap. J.*, **434**, 82.

Goodrich, R. W. & Miller, J. S. 1995. *Ap. J.*, in press.

Glenn, J., Schmidt, G. D., & Foltz, C. B. 1994. *Ap. J.*, **434**, L47.

Hamann, F., Korista, K. T., & Morris, S. L. 1993. *Ap. J.*, **415**, 541.

Hes, R 1995. Ph.D. Thesis.

Impey, C. D., Malkan, M. A., Webb, W., & Petry, C. E 1995. *Ap. J.*, **440**, 80.

Jeffery, D. J. 1990. *Ap. J.*, **352**, 267.

Koratkar, A., Antonucci, R. R. J., Bushouse, H., & Kinney, A. 1995. *Ap. J. Lett.*, in press.

Koratkar, A., Antonucci, R. R. J., Goodrich, R. W., Bushouse, H., & Kinney, A. 1995. *Ap. J.*, in press.

Korista, K. T., Voit, G. M., Morris, S. L., & Weymann, R. J. 1993. *Astrophys. J. Suppl.*, **88**, 357.

Laor, A., & Draine, B. T. 1993. *Ap. J.*, **402**, 441.

Laor, A., Netzer, H., & Piran, T. 1990. *MNRAS*, **242**, 560.

Lee, H.-W., Blandford, R.D. & Western L. 1994. *MNRAS*, **267**, 303. (Paper 1)

Lee, H.-W. 1994. *MNRAS*, **268**, 49. (Paper 2)

Miller, J. S., & Goodrich, R. W. 1990. *Ap. J.*, **355**, 456.

Murray, N., Grossman, S. A., & Chiang, J. 1995. *Ap. J.*, in press.

Netzer, H. 1990. *Active Galactic Nuclei*, Berlin: Springer-Verlag.

Osterbrock, D. E. 1989. Astrophysics of Gaseous Nebulae abd Active Galactic Nuclei, University Science Books, Mill Valley.

Perry, J., & Dyson, J. E. 1985. *MNRAS*, **213**, 665.

Perry, J. J. & Williams, R. 1993. *MNRAS*, **260**, 437.

Peterson, B.M., Reichert, G. A., Korista, K. T., & Wagner, R. M. 1990. *Ap. J.*, **352**, 68.

Peterson, B.M. *et al.* 1991. *Ap. J.*, **368**, 119.

Peterson, B.M. *et al.* 1994. *Ap. J.*, **425**, 622.

Rauch, K. P., & Blandford, R. D. 1991. *Ap. J.*, **381**, L39.

Rees, M.J. 1987. *MNRAS*, **228**, 47P.

Rybicki, G. B.,& Hummer, D. G. 1978. *Ap. J.*, **219**, 654.

Scoville, N.,& Norman, C. 1995. *Ap. J.*, in press.

Shields, J., Ferland, G. & Peterson, B. M. 1995. *Ap. J.*, **441**, 507.

Smith, P. S., Schmidt, G. D., Allen, R. G., & Angel, J. R. P. 1995. *Ap. J.*, in press.

Sobolev, V. V. 1947. Moving Envelopes of Stars (Leningrad: Leningrad State University)(English trans.: S. Gaposchkin [Cambridge: Harvard University Press, 1960].

Stockman, H. S., Angel, J. R. P.,& Hier, R. G. 1981. *Ap. J.*, **243**, 404.

Stockman, H. S., Angel, J. R. P., & Miley, G. K. 1979. *Ap. J.*, **227**, L55.

Tran, H. D., Miller, J. S., & Kay, L. E. 1992. *Ap. J.*, **397**, 452.

Turnshek, D. A. 1988. in Space Telescope Sci. Inst. Symposium 2, QSO Absorption Lines: Probing the Universe,ed. S. C. Blades, D. A. Turnshek, & C. A. Norman (Cambridge: Cambridge Univ. Press), p.17.

Verner, D. A., Barthel, P. D., & Tytler, D. 1994. *Astron. Astrophys. Suppl. Ser*, **108**, 287.

Weymann, R. J. 1970. *Ap. J.*, **160**, 31.

Weymann, R. J., Morris, S. L., Foltz, C. B.,& Hewett, P. C. 1991. *Ap. J.*, **373**, 23.

Weymann, R. J., Scott, J. S., Schiano, A. V. R., & Christiansen, W. A. 1982. *Ap. J.*, **262**, 497.

Weymann, R. J., Turnshek, D. A., & Christiansen, W. A. 1985. in Astrophysics of Active Galaxies and Quasi-Stellar Objects, ed. J. Miller, (University Science Books: Mill Valley).

Williams, R. & Perry, J. J. 1994. *MNRAS*, **269**, 538.

Wilson, A. S. 1995. in Evidence for the Torus Oxford Astrophysics Workshop in press.

FIGURE CAPTIONS

Figure 1 – Polarization of the emergent light from an illuminated slab with optical depth $\tau = 5$, when the source and the observer is collinear. In the upper panel the polarization for transition J=0 $\rightarrow$ 1 is shown. In the lower panel the polarization for transition J=1/2 $\rightarrow$ 3/2. (Note that for the doublet transition J=1/2 $\rightarrow$ 1/2, 3/2 the statistical factor 2/3 should be multiplied in order to get the correct degree of polarization.) The horizontal axis represents the cosine of the scattering angle α defined in the text. The photons scattered into $\mu_{out} \leq 0.1$ are collected from various incident directions.

Figure 2 – Polarization of the emergent light from an illuminated slab with optical depth $\tau = 5$, where the source and the observer is not collinear. The light source is fixed in the direction of $\mu = 0.5$, $\phi = 0$ and the scattered photons are collected as a function of $\mu_{out} = \cos\theta_{out}$ for azimuthal angles. The continuous lines represent the result from single scattering which generally gives the largest degrees of polarization. In the left panels the transition is J=0 $\rightarrow$ 1 and in the right panels the result is for the transition J=1/2 $\rightarrow$ 3/2. In order to get the result for the doublet transition J=1/2 $\rightarrow$ 1/2, 3/2, the statistical factor 2/3 should be multiplied.

Figure 3 – Schematic geometry of clouds moving radially outward. Each line emitting cloud is moving linearly outward from the disk making an angle θ_i with the disk and $\mu_{out} \equiv \cos\theta_{out}$ is the cosine of the angle between the disk axis and the line of sight to the observer.

Figure 4 – Scattered flux, degree of polarization, and polarized flux of scattered radiation of central continuum from an ensemble of line emitting clouds shown in Fig. 3. Each cloud is moving radially making an angle $\theta_i = 50^\circ$ with constant speed $\propto r^{-1/2}$ along a linear trajectory, where r is the distance from the center to the foot point. The clouds are assumed to be distributed over 3 decades of radius.

Figure 5 – The same quantities as in Fig.4 for the transition J=1/2 $\rightarrow$ 3/2. For the doublet transition J=1/2 $\rightarrow$ 1/2, 3/2, the statistical factor 2/3 should be multiplied.

Figure 6a – Polarized flux per sterad of scattered photon from a singlet Sobolev surface (J=0 $\rightarrow$ 1) for a flow expanding paralell to the incident direction. The velocity field is given by $\mathbf{V} = \mathbf{V_0} + (\mathbf{zV'})\hat{\mathbf{z}}$, where $\mathbf{V_0}$ and V' are constant. The Sobolev optical depth is given by $\tau_{esc}(\mu) = \tau_0/\mu^2$ where $\mu = \cos\theta$ is the cosine of the angle between the wavevector of the scattered photon and the line of sight. The normalization is given by the total incident flux.

Figure 6b – Same quantity as in Fig. 6a for isotropic expansion. The velocity field is given by $\mathbf{V} = \mathbf{V_0} + V'(x\hat{x} + y\hat{y} + z\hat{z})$, where $\mathbf{V_0}$ and V' are constant. The Sobolev optical depth is given by $\tau_{esc}(\mu) = \tau_0$.

Figure 6c – Same quantity as in Fig. 6a for perpendicular expansion. The velocity field is given by $\mathbf{V} = \mathbf{V_0} + V'(x\hat{x} + y\hat{y})$, where $\mathbf{V_0}$ and V' are constant. The Sobolev optical depth is given by $\tau_{esc}(\mu) = \tau_0/(1-\mu^2)$.

Figure 6d – Same quantity as in Fig. 6a for converging flow. The velocity field is given by $\mathbf{V} = \mathbf{V_0} + V'(z\hat{z} - x\hat{x} - y\hat{y})$, where $\mathbf{V_0}$ and $V' > 0$ are constant (expanding in the incident direction). The Sobolev optical depth is given by $\tau_{esc}(\mu) = \tau_0/|1-2\mu^2|$.

Figure 7abcd – Same quantities as Fig. 6abcd for J=1/2 $\rightarrow$ 1/2, 3/2 doublet.

Figure 8ab – Same quantities as Fig. 6a for the triplet $^2S_{1/2} \rightarrow ^2 D_{3/2,\ 5/2}$, where the incident spectrrum is given by a power law where $\alpha = 1$, and $\alpha = 3$. Figure 8cd – Same quantities as Fig. 6a for the shifted hexaplet $^3P^O_{0,1,2} \rightarrow ^3 D_{1,2,3}$ with the same incident spectrrum as in Fig. 8ab.

Figure 9a – Total flux, polarization and polarized flux from disk wind models by Hamann *et al.* 1993. The velocity is given by $\mathbf{V} \propto r\hat{r}$ and the covering factor is $q_{disk} = 0.25$.

Figure 9b – Total flux, polarization and polarized flux from the same model as in Fig. 8a with additional azimuthal velocity component. The velocity is given by $\mathbf{V} \propto [r\hat{r} + A\hat{\phi}/(r\sin\theta)]$, where A is constant. A is chosen to satisfy $V_\phi/V_r = 0.2$ at the point where $V_r = 18,000$ km s^{-1}, $\theta = \pi/2$.

Figure 9c – Total flux, polarization and polarized flux from a conical wind model by Hamann *et al.* 1993. The same velocity law and the same covering factor are adopted as in Fig. 8a.

Figure 9d – Total flux, polarization and polarized flux from the same model as in Fig. 8c with additional azimuthal velocity component. The same velocity law is adopted as in Fig. 8b and A is chosen to satisfy $V_\phi/V_r = 0.1$ at the same point.

Figure 10 – A typical Sobolev surface of an equatorial flow with angular momentum for an observer lying on $x - z$ plane with colatitude $\theta = \pi/3$. Each flow line lies on a hyperboloid ($\lambda = constant$ in the oblate spheroidal coordinate system. See Appendix A), and the fluid element accelerates to an asymptotic speed (See the text).

Figure 11a – Total flux, polarization and polarized flux from a purely poloidal equatorial flow for J=0 $\rightarrow$ 1. The observer's line of sight is $\cos\theta = 0.2$ and the parameters are chosen so that $\tau_{Sob} = 1$ at $\Delta V = -1.7 \times 10^9$ cm s^{-1}. See Appendix for detail.

Figure 11b – Total flux, polarization and polarized flux from an equatorial flow with angular momentum for J=0 $\rightarrow$ 1.

Figure 11c – Total flux, polarization and polarized flux from an equatorial flow with no angular momentum for J=1/2 $\rightarrow$ 1/2, 3/2 doublet.

Figure 11d – Total flux, polarization and polarized flux from an equatorial flow with angular momentum for J=1/2 $\rightarrow$ 1/2, 3/2 doublet.

Figure 12 – A typical Sobolev surface of a bipolar flow without angular momentum for an observer lying on $x - z$ plane with colatitude $\theta = \pi/3$. Each flow line lies on a paraboloid ($\xi_2 = constant$ in the parabolic coordinate system. See Appendix B), and the fluid element accelerates to an asymptotic speed (See the text).

Figure 13a – Total flux, polarization and polarized flux from a purely poloidal bipolar flow for J=0 $\rightarrow$ 1. The observer's line of sight is $\cos\theta = 0.8$ and the parameters are chosen so that $\tau_{Sob} = 1$ at $\Delta V = -1.7 \times 10^9$ cm s^{-1}. See Appendix for detail.

Figure 13b – Total flux, polarization and polarized flux from a bipolar flow with angular momentum for J=0 $\rightarrow$ 1.

Figure 13c – Total flux, polarization and polarized flux from a bipolar flow with no angular momentum for J=1/2 $\rightarrow$ 1/2, 3/2 doublet.

Figure 13d – Total flux, polarization and polarized flux from a bipolar flow with angular momentum for J=1/2 $\rightarrow$ 1/2, 3/2 doublet.

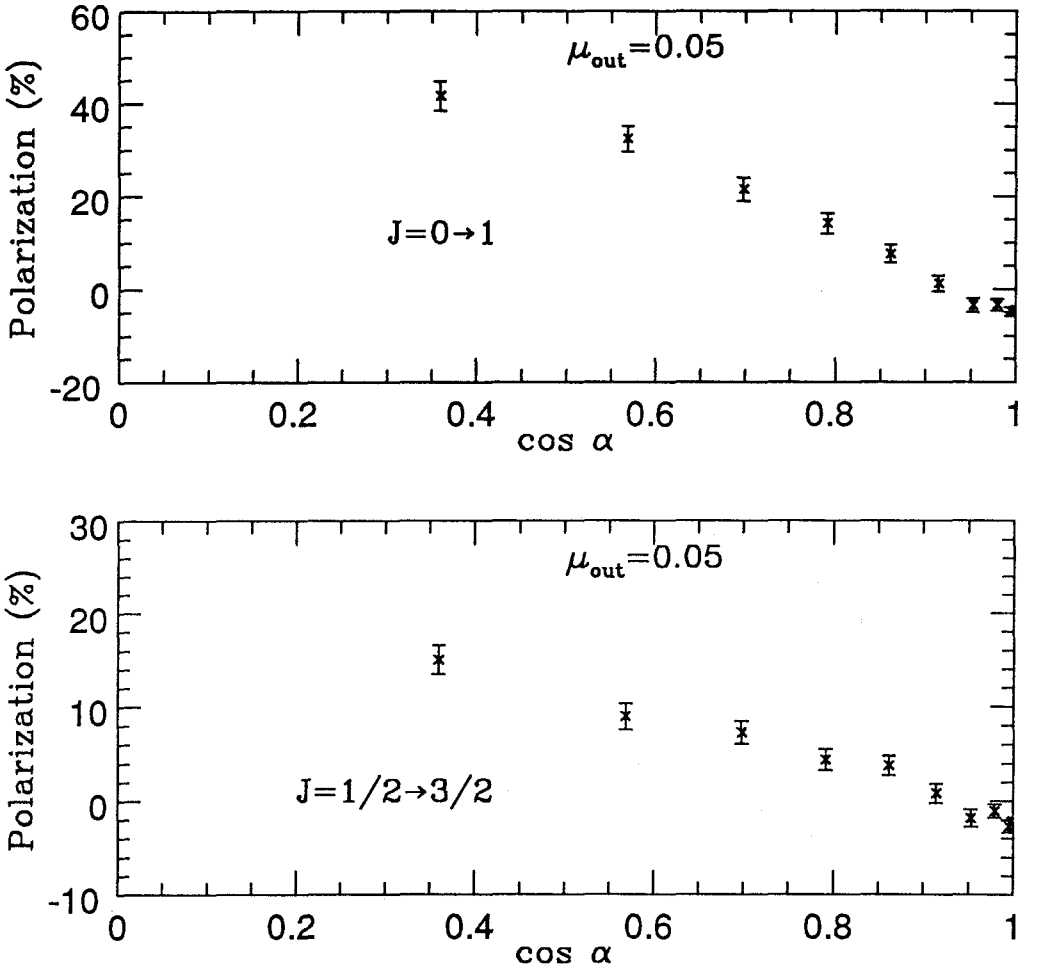
Polarization (%)
60
40
20
0
-20
μ_{out}=0.05
J=0→1
0
0.2
0.4
0.6
0.8
1
cos α
Polarization (%)
30
20
10
0
-10
μ_{out}=0.05
J=1/2→3/2
0
0.2
0.4
0.6
0.8
1
cos α

Figure 1

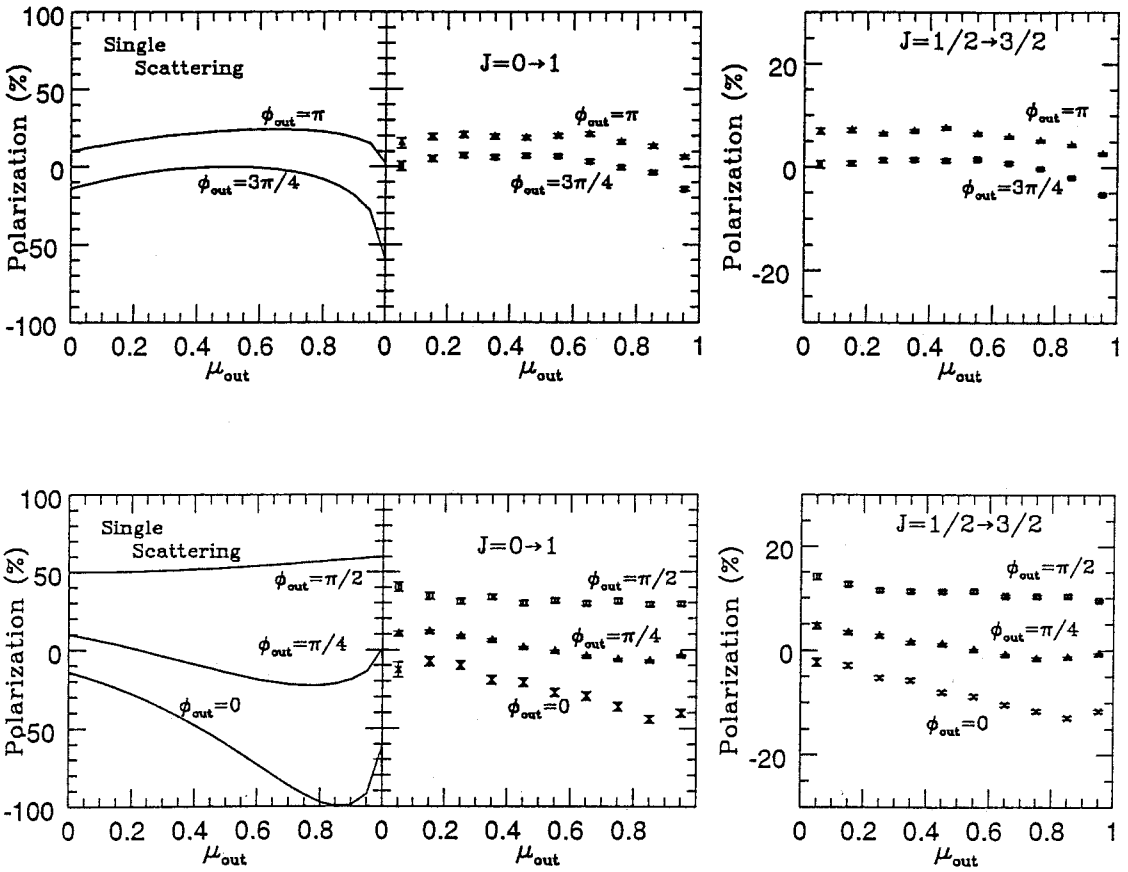
Single
Scattering
J=0→1
J=1/2→3/2
Polarization (%)
μ_{out}
$\phi_{out}=\pi$
$\phi_{out}=3\pi/4$
$\phi_{out}=\pi/2$
$\phi_{out}=\pi/4$
$\phi_{out}=0$

Figure 2

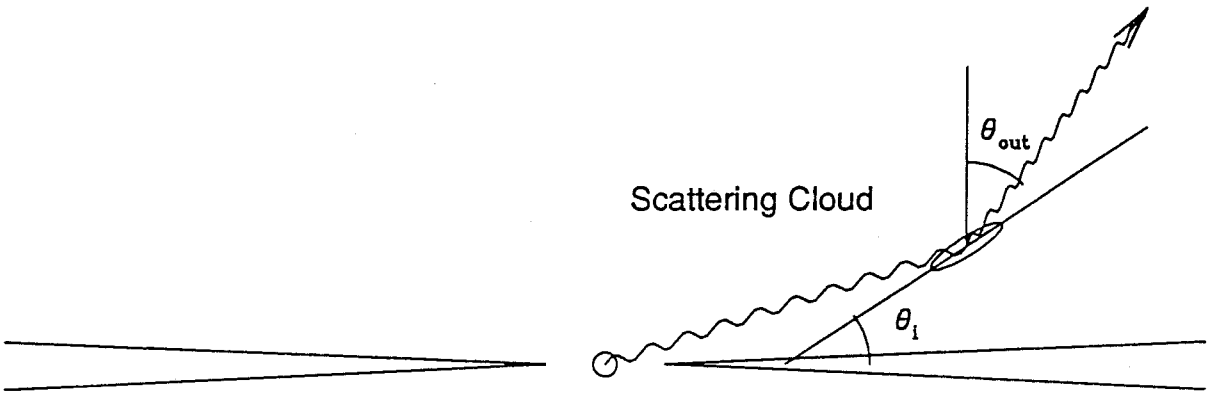
θ_{out}
Scattering Cloud
θ_i
The Central Continuum Source

Figure 3

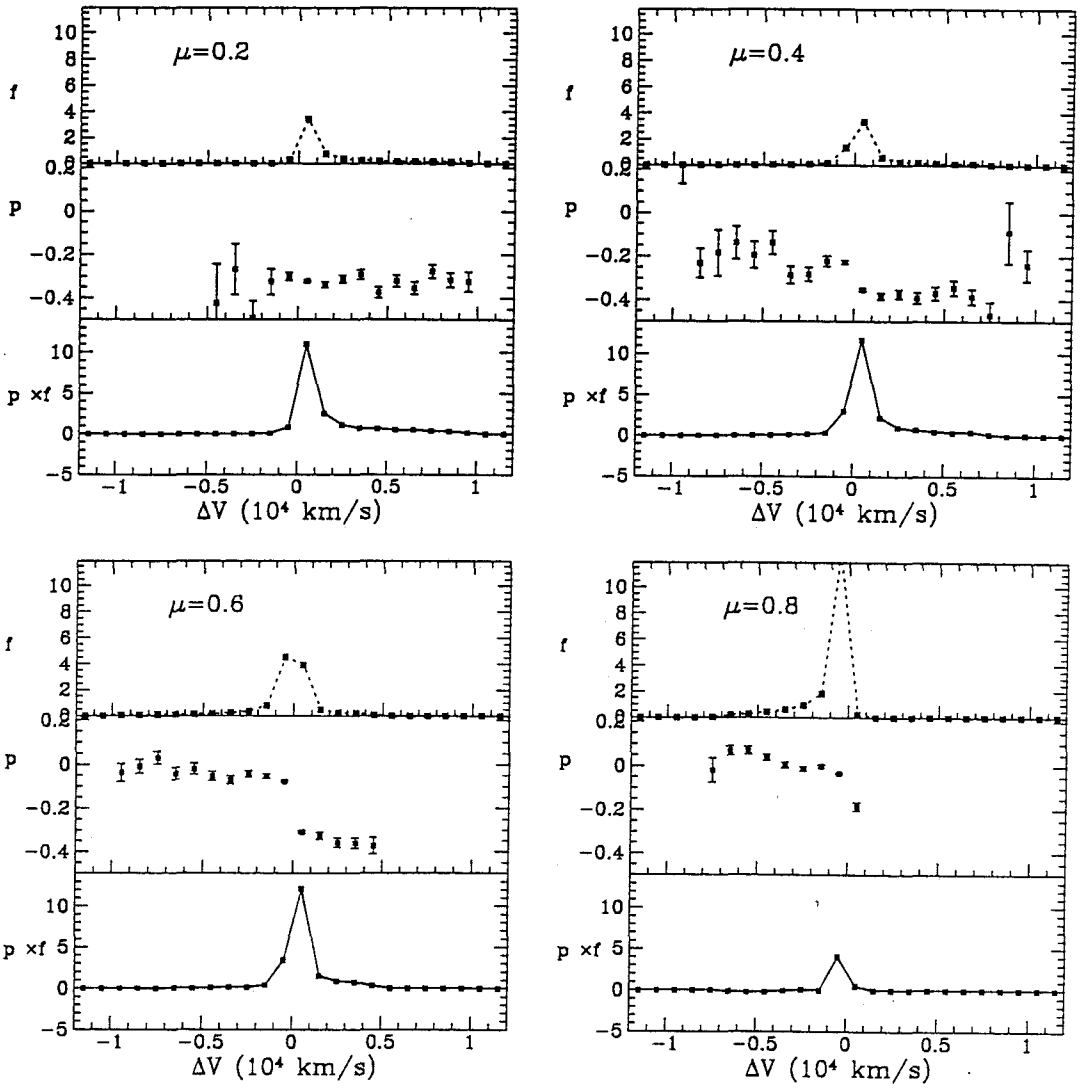

Figure 4

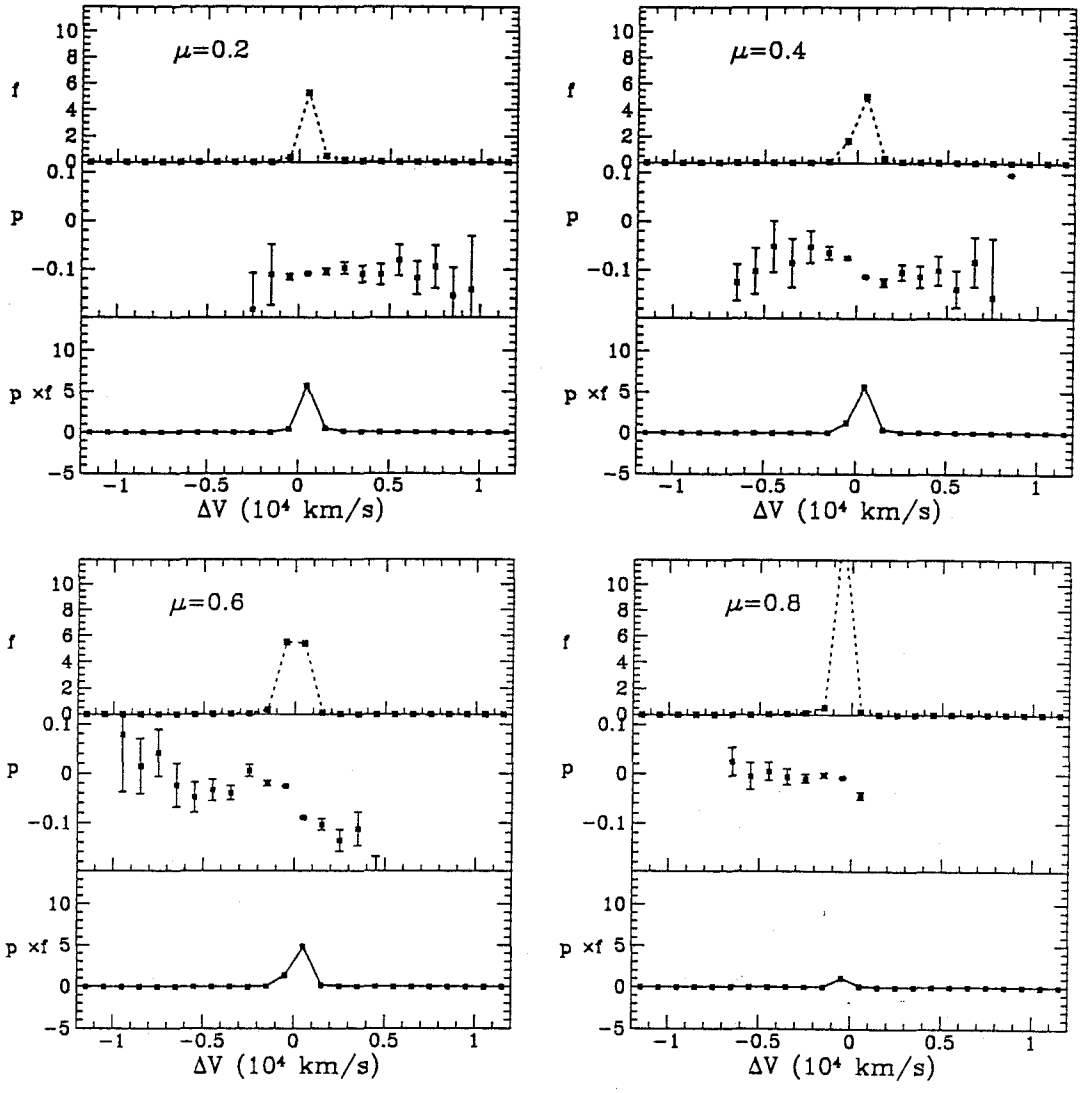

Figure 5

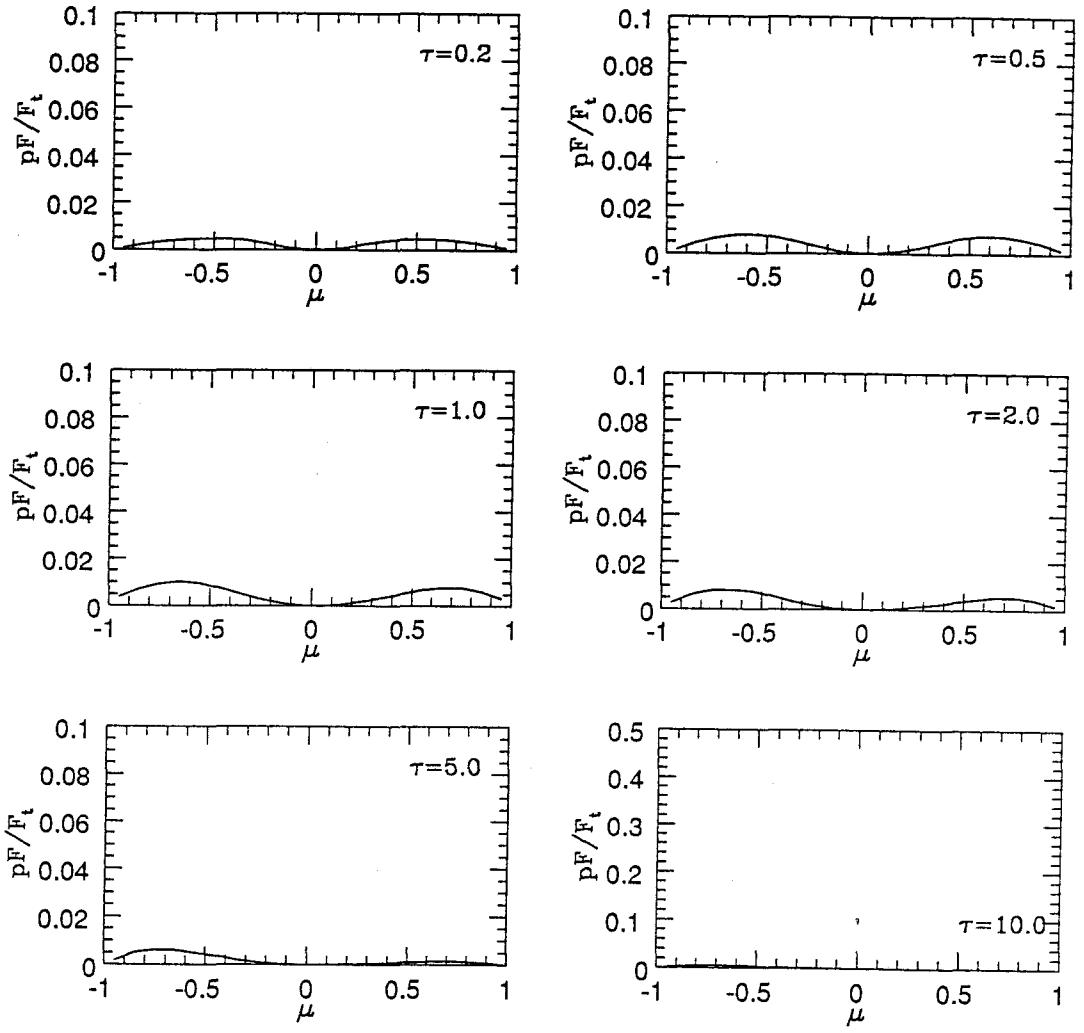

Figure 6a

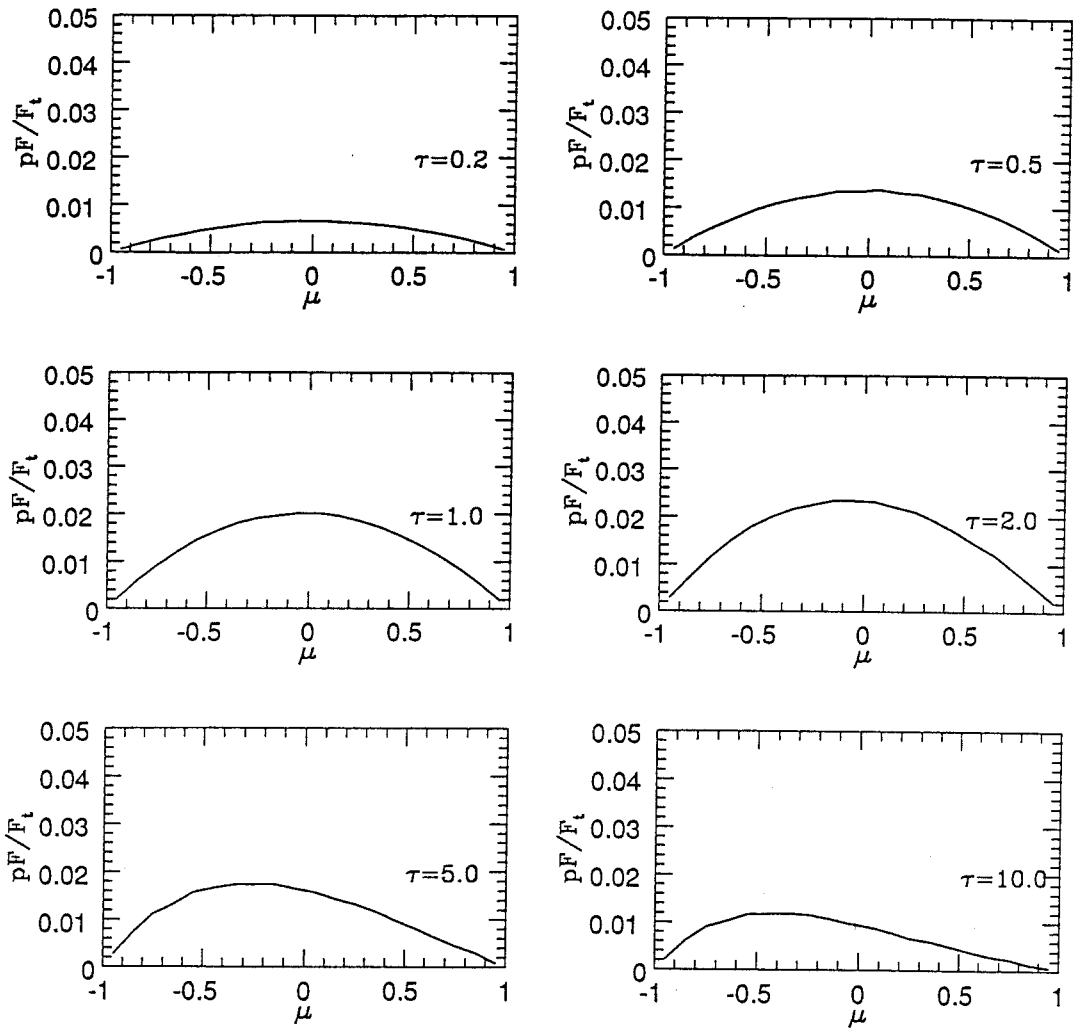

Figure 6b

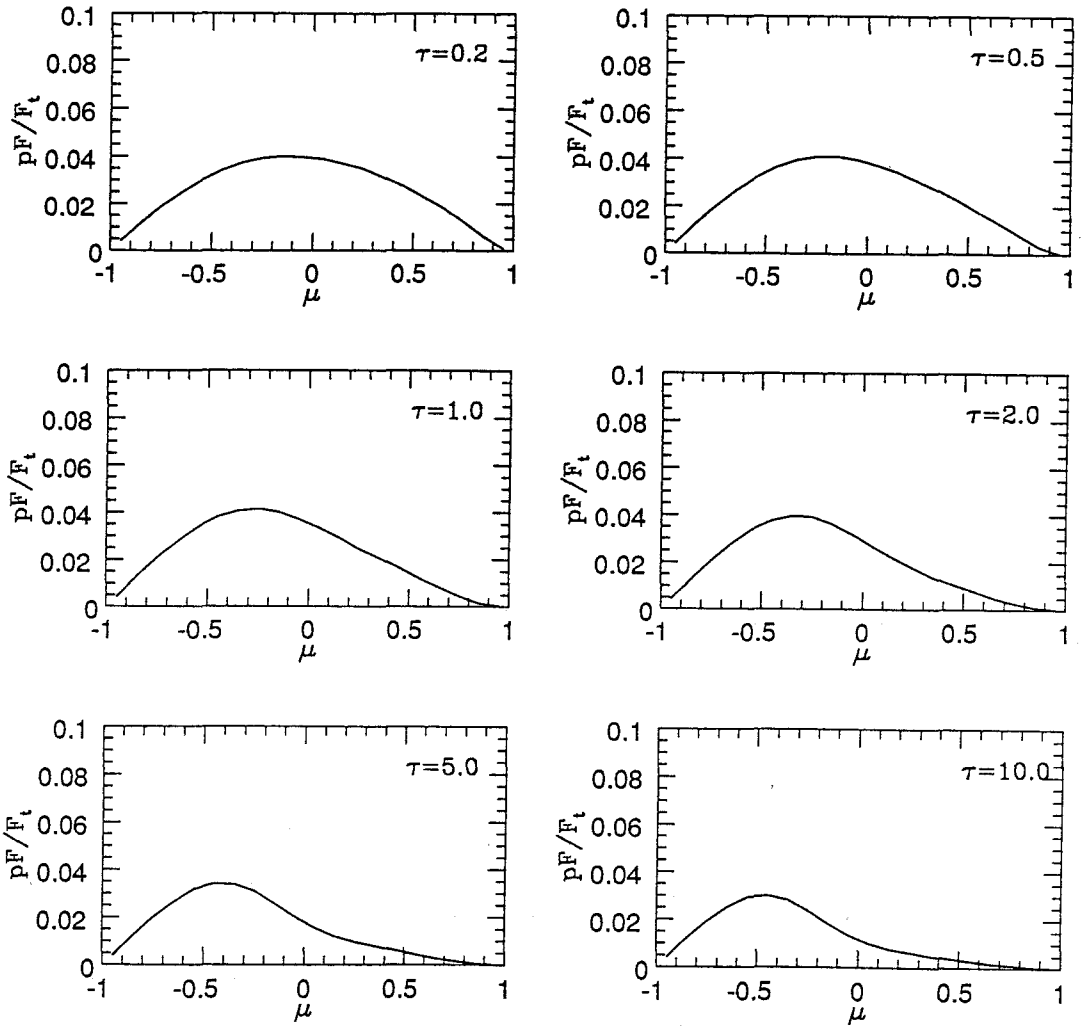

Figure 6c

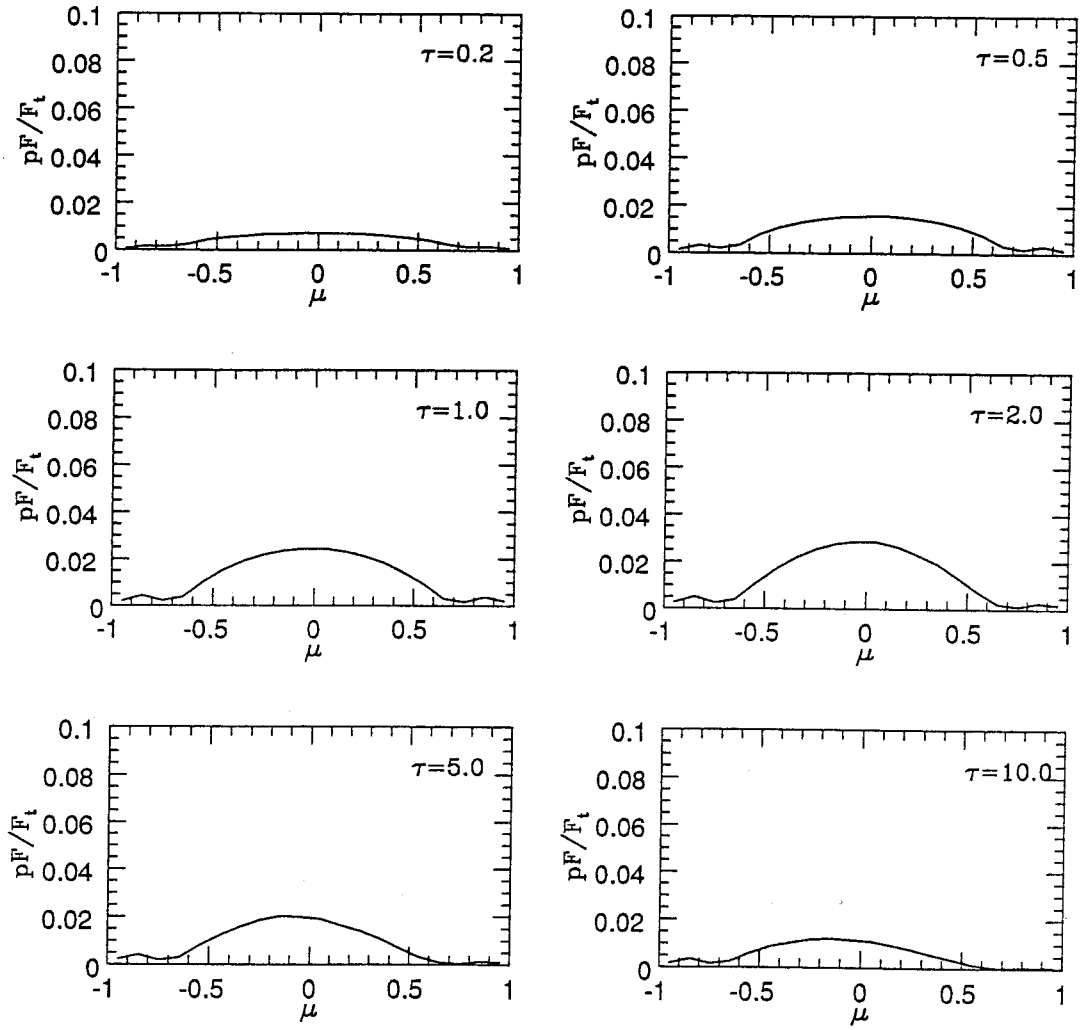

Figure 6d

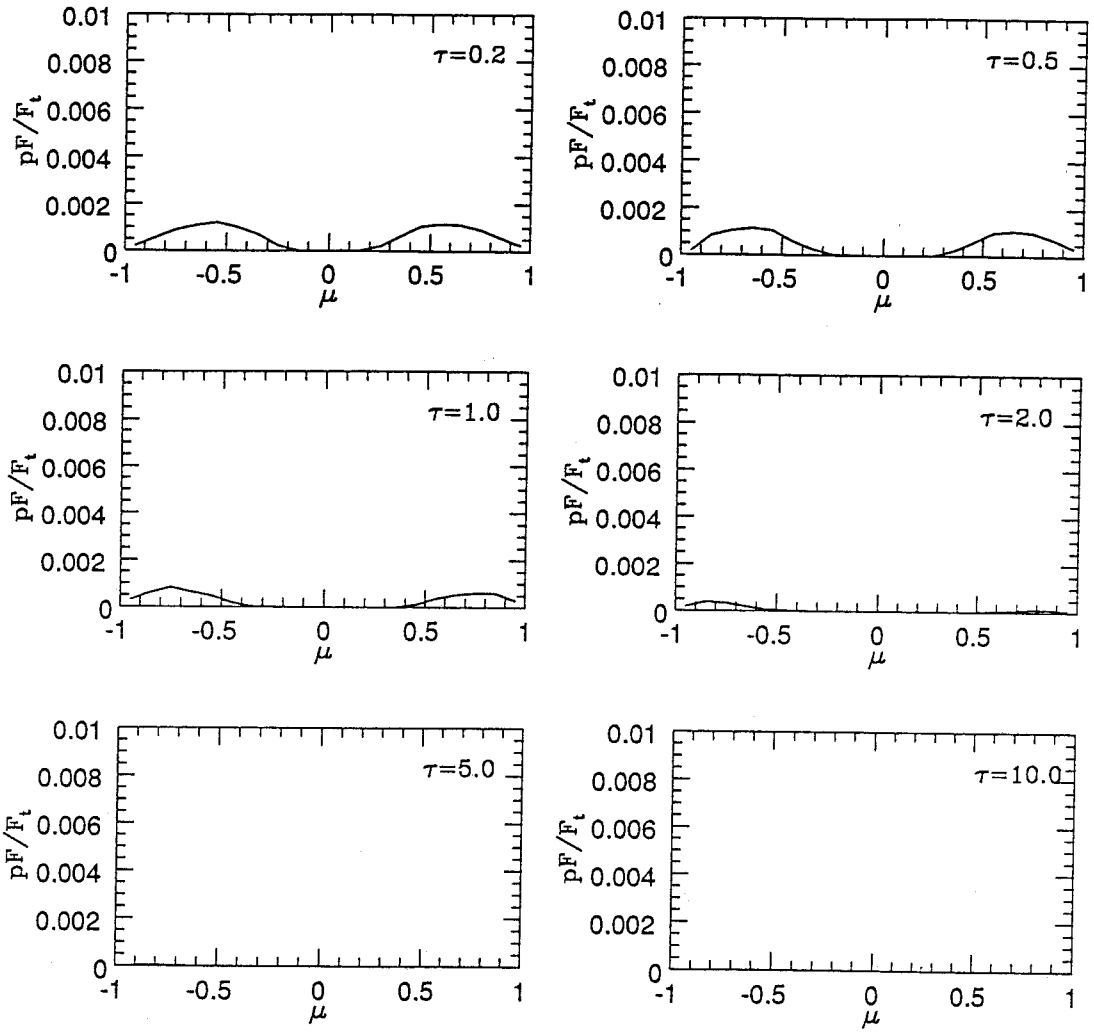
τ=0.2
τ=0.5
τ=1.0
τ=2.0
τ=5.0
τ=10.0
pF/F_t
μ
0.01
0.008
0.006
0.004
0.002
0
-1
-0.5
0
0.5
1

Figure 7a

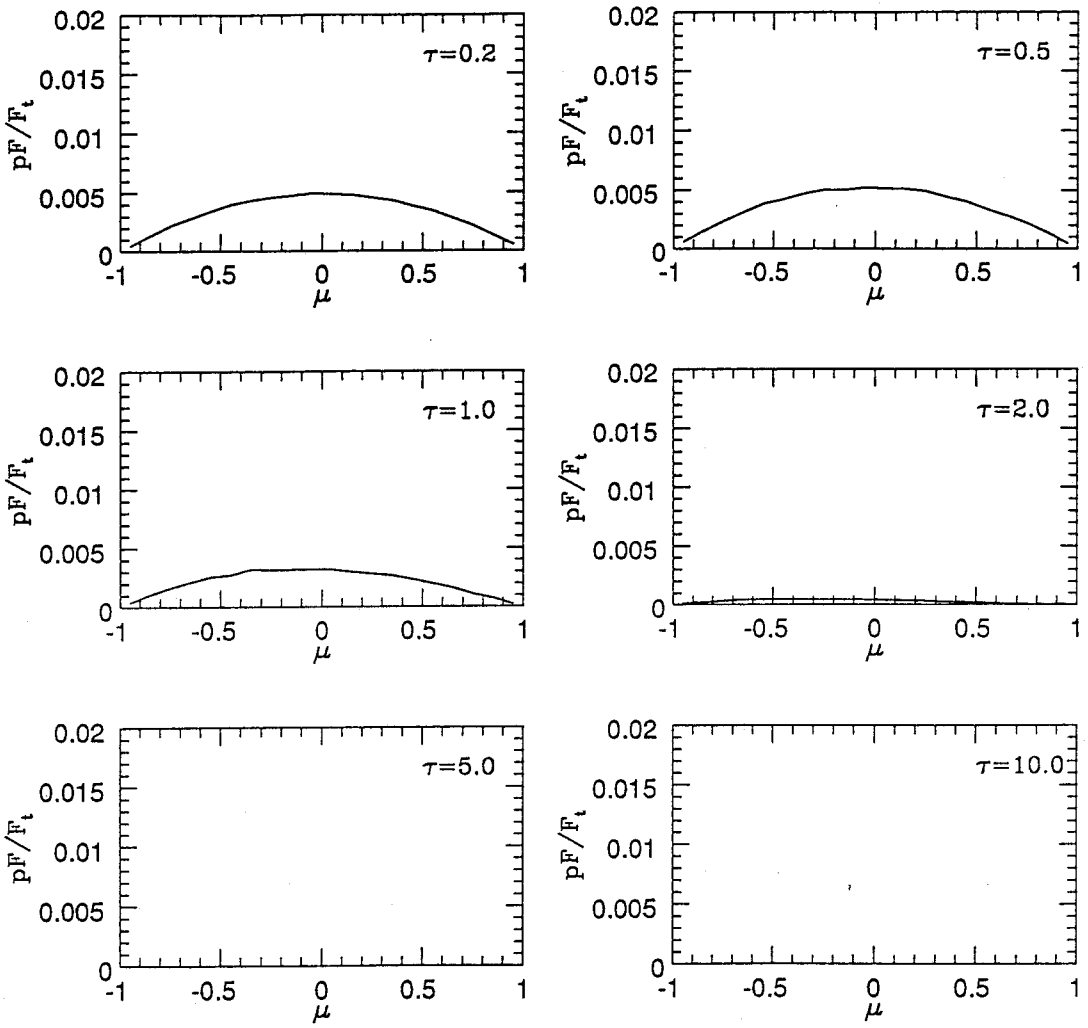

Figure 7b

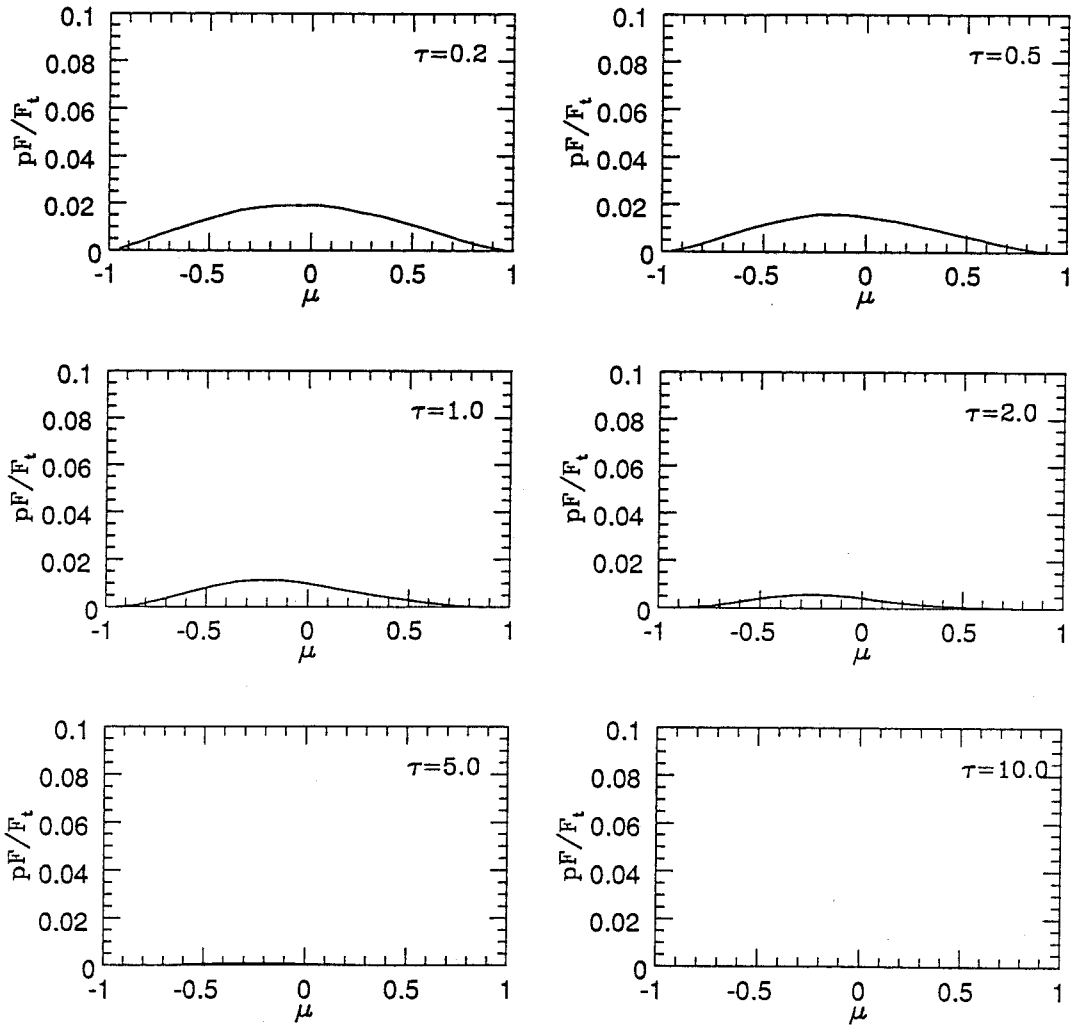

Figure 7c

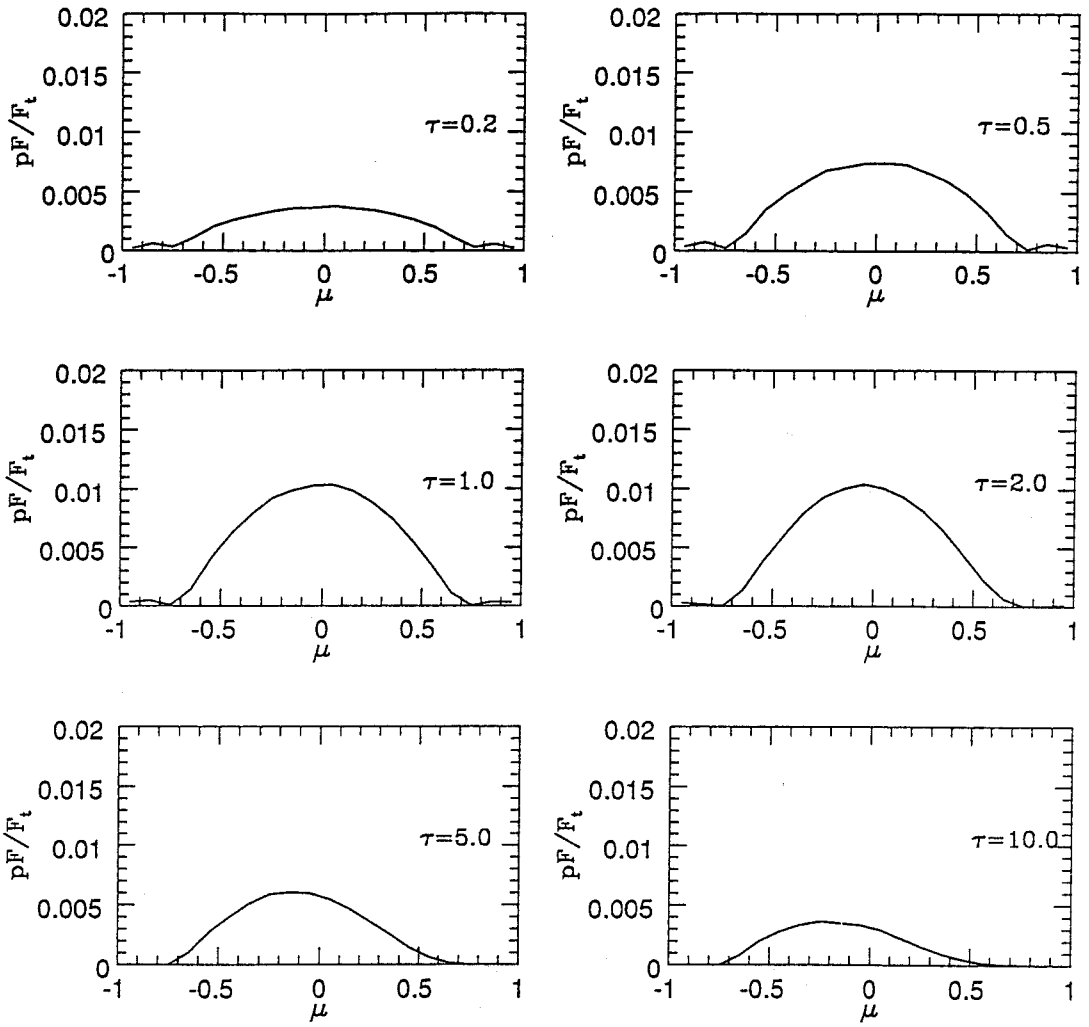

Figure 7d

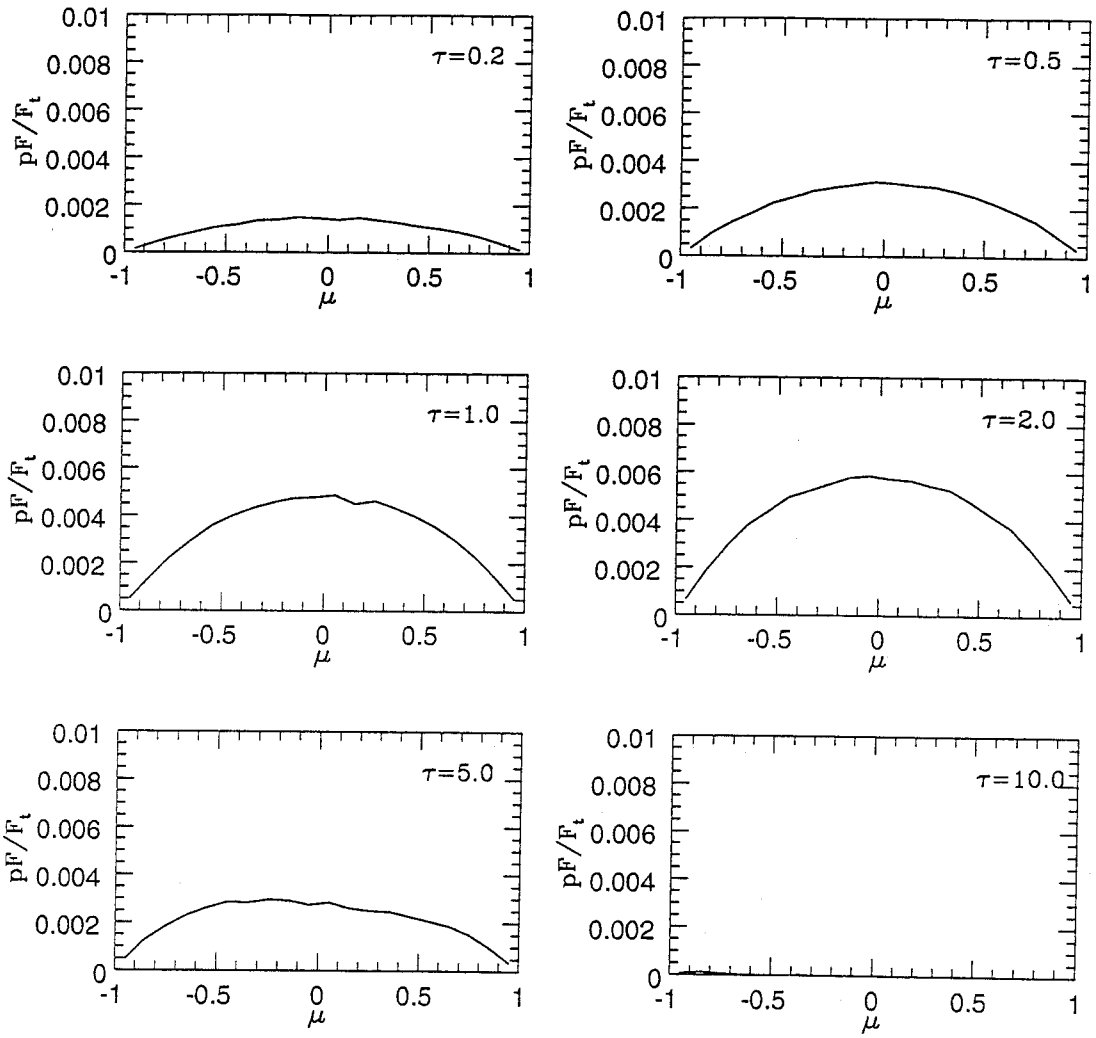
0.01
0.008
0.006
0.004
0.002
0
pF/F_t
τ=0.2
τ=0.5
τ=1.0
τ=2.0
τ=5.0
τ=10.0
-1
-0.5
0
0.5
1
μ

Figure 8a

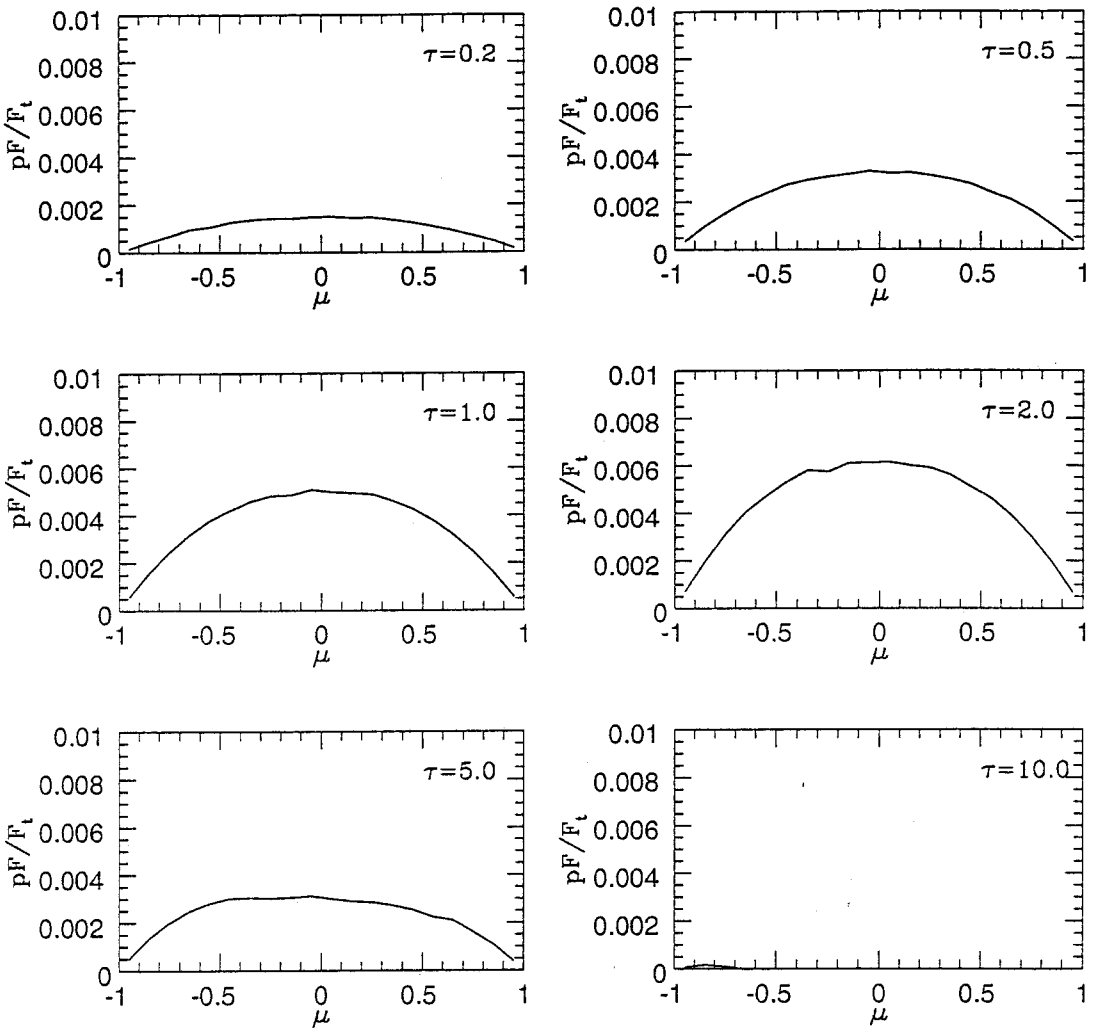
τ=0.2
τ=0.5
τ=1.0
τ=2.0
τ=5.0
τ=10.0
pF/F_t
μ
0.01
0.008
0.006
0.004
0.002
0
-1
-0.5
0
0.5
1

Figure 8b

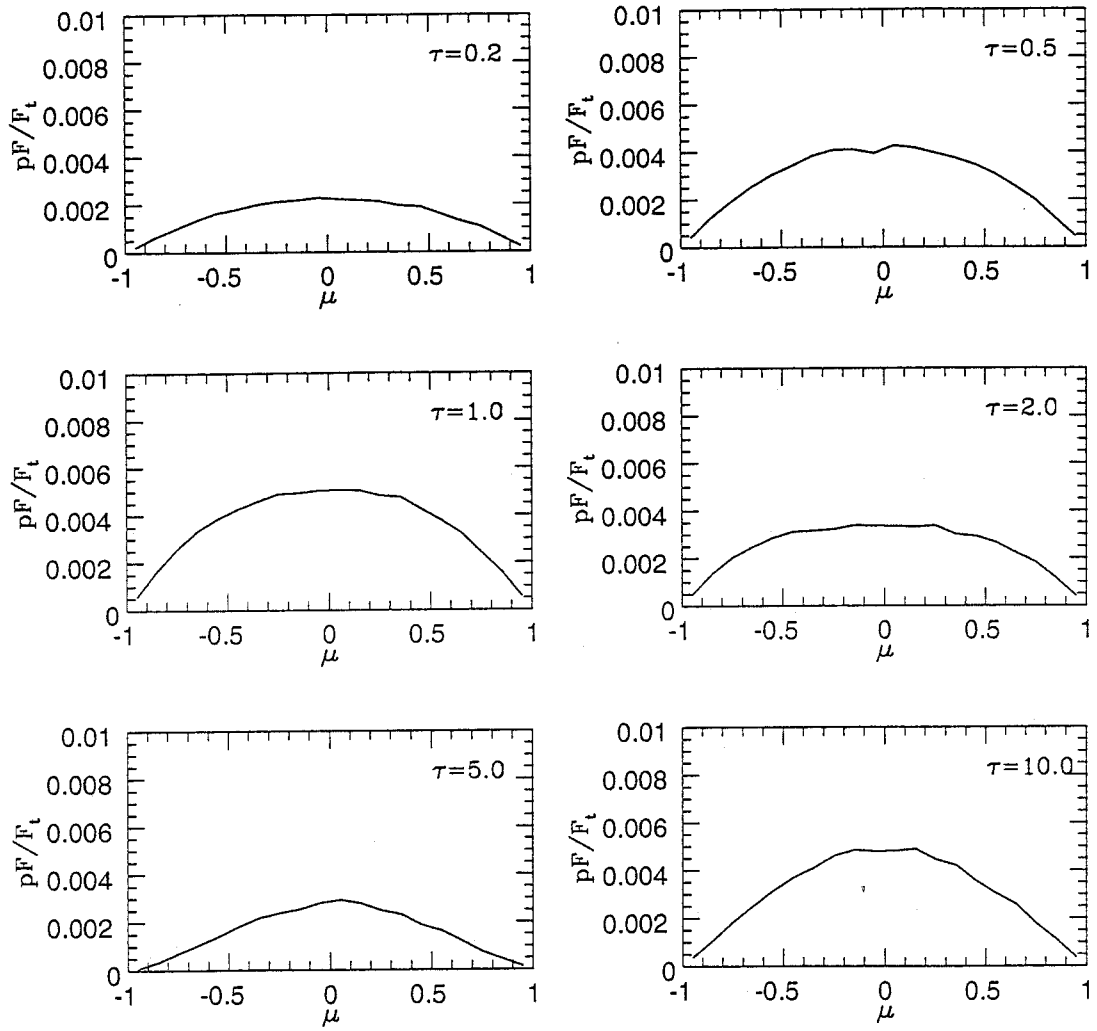
τ=0.2
τ=0.5
τ=1.0
τ=2.0
τ=5.0
τ=10.0
pF/F_t
μ
0.01
0.008
0.006
0.004
0.002
0
-1
-0.5
0
0.5
1

Figure 8c

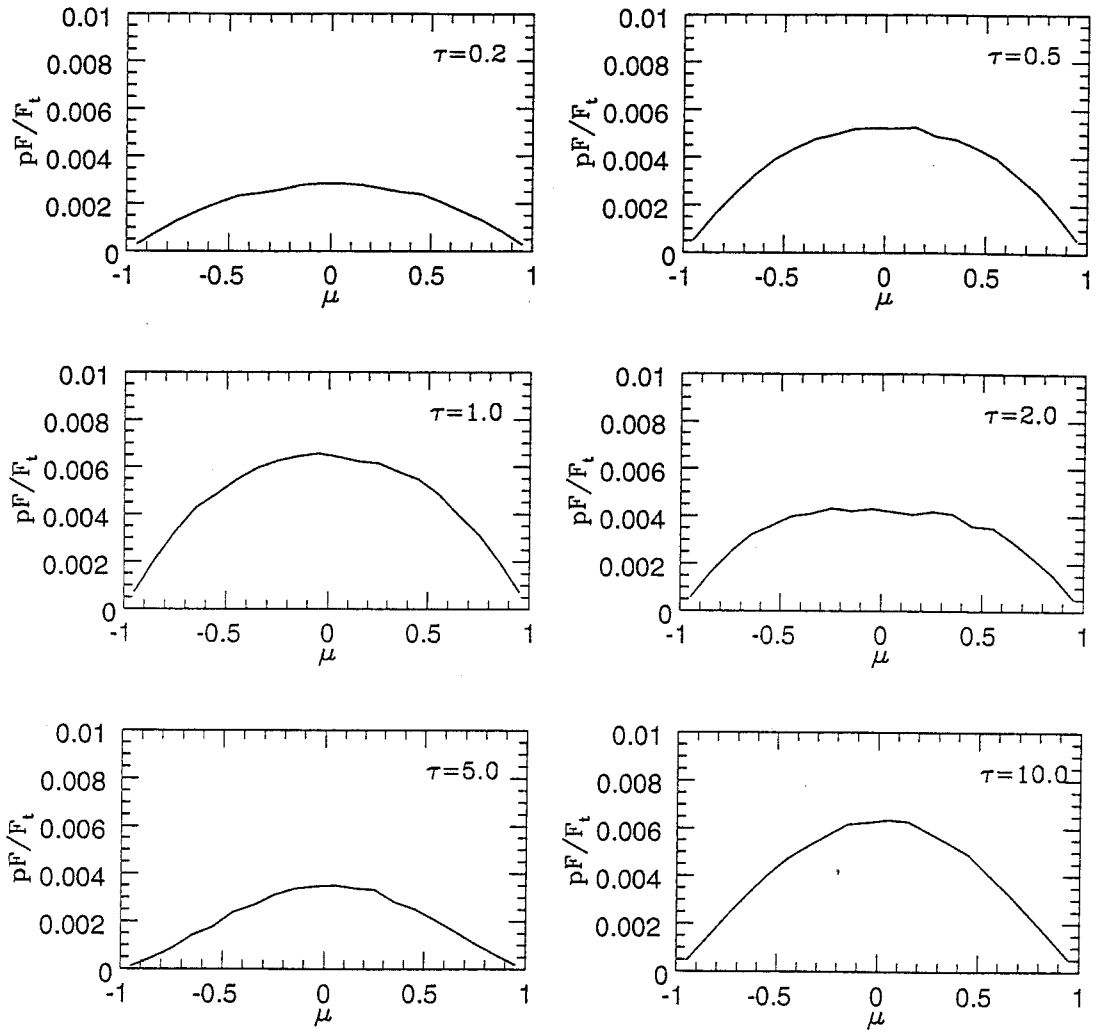
τ=0.2
τ=0.5
τ=1.0
τ=2.0
τ=5.0
τ=10.0
pF/F_t
μ
0.01
0.008
0.006
0.004
0.002
0
-1
-0.5
0
0.5
1

Figure 8d

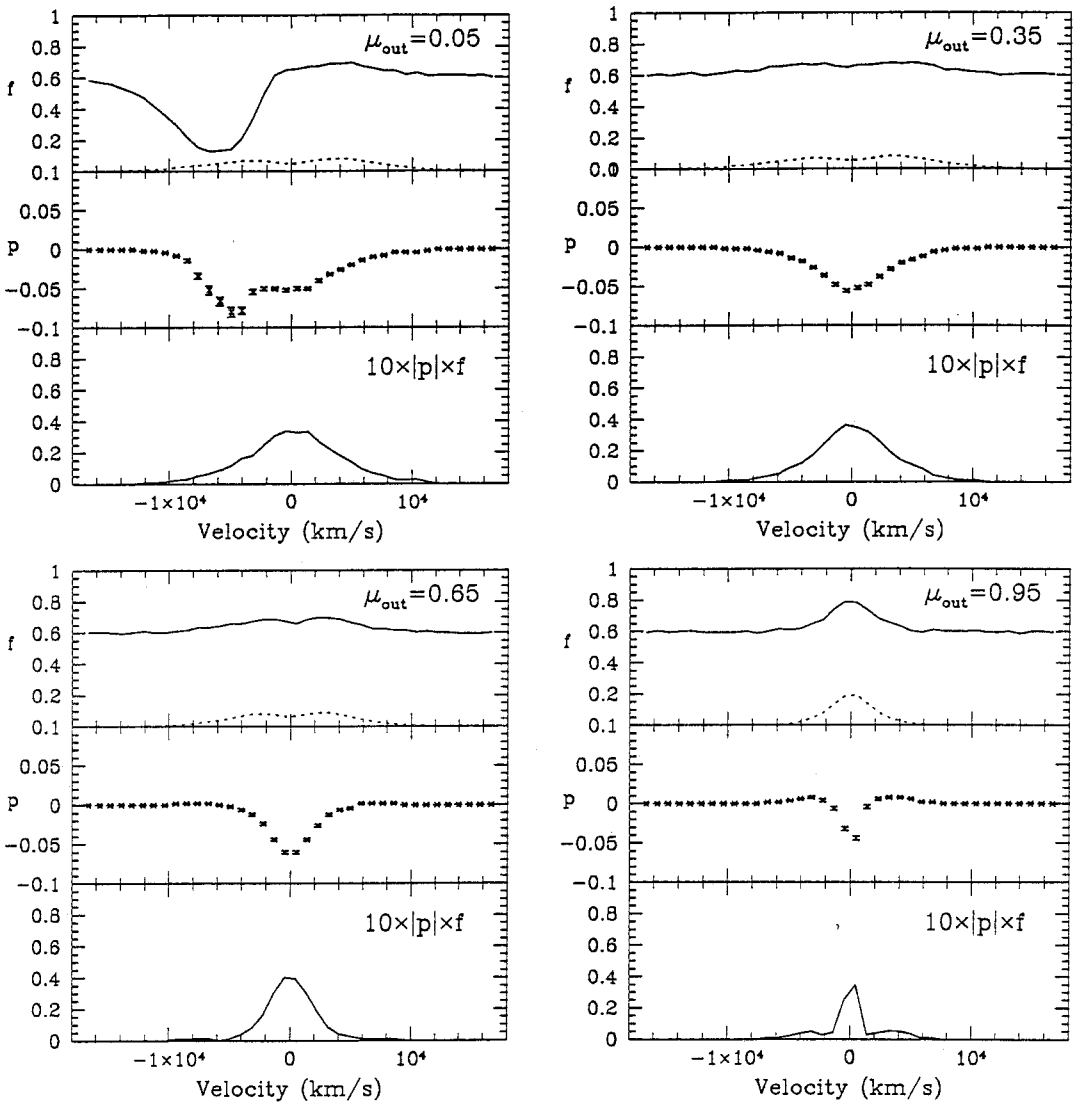
μ_{out}=0.05
μ_{out}=0.35
μ_{out}=0.65
μ_{out}=0.95
f
p
10×|p|×f
−1×10⁴
0
10⁴
Velocity (km/s)

Figure 9a

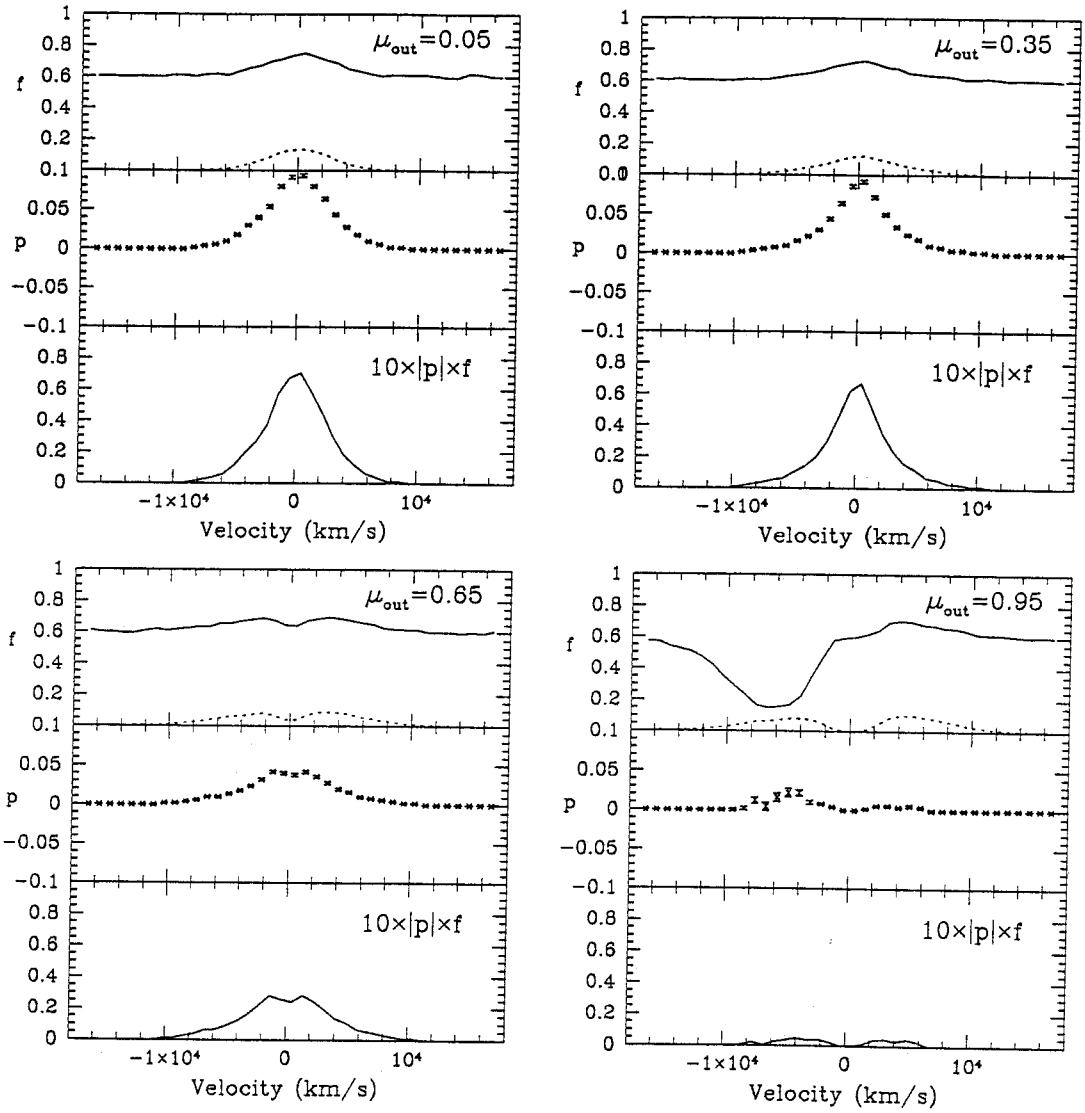
μ_{out}=0.05
μ_{out}=0.35
μ_{out}=0.65
μ_{out}=0.95
f
p
10×|p|×f
Velocity (km/s)
−1×10⁴
0
10⁴

Figure 9b

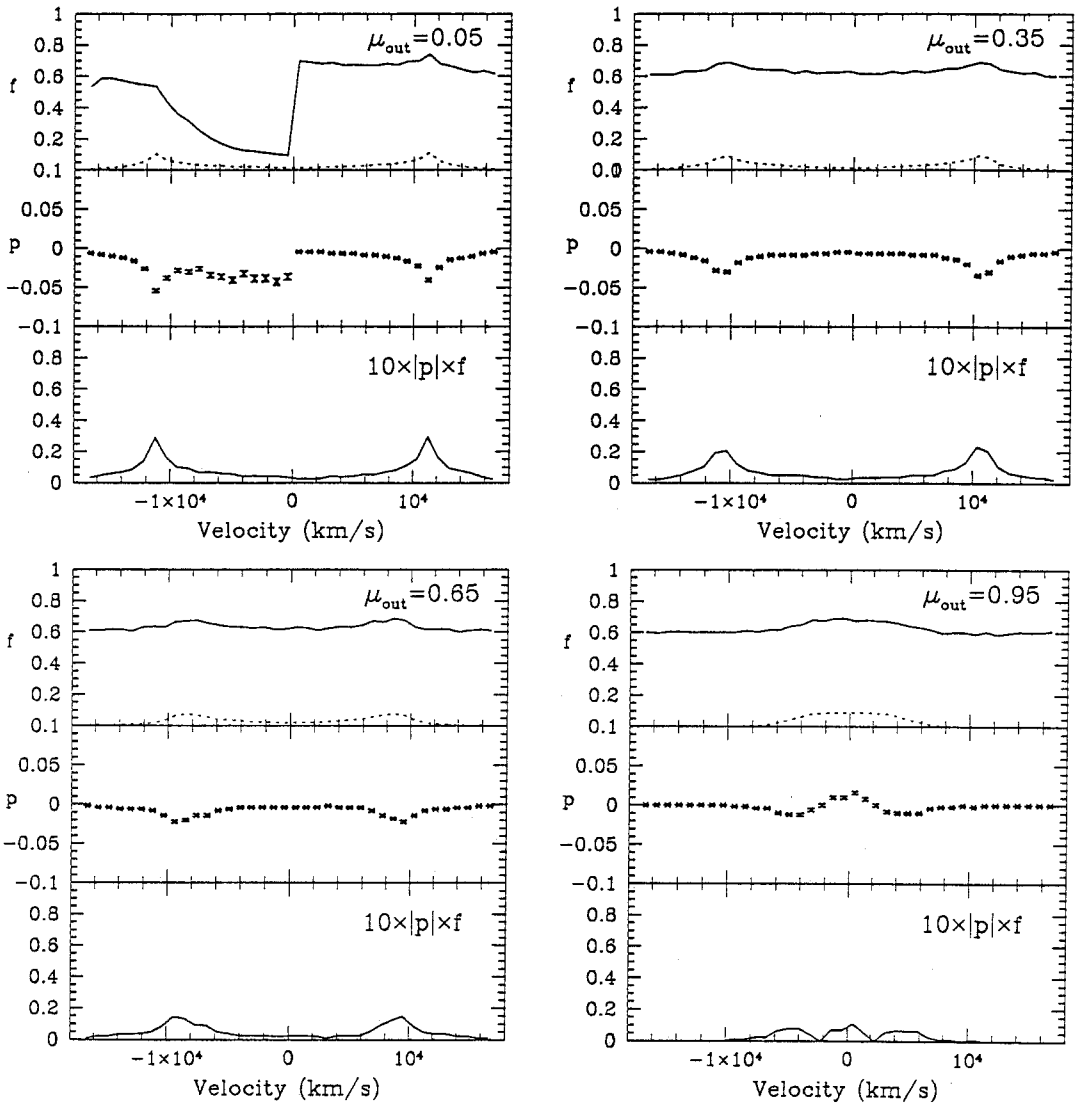
μ_{out}=0.05
μ_{out}=0.35
μ_{out}=0.65
μ_{out}=0.95
f
p
10×|p|×f
Velocity (km/s)
−1×10⁴
0
10⁴

Figure 9c

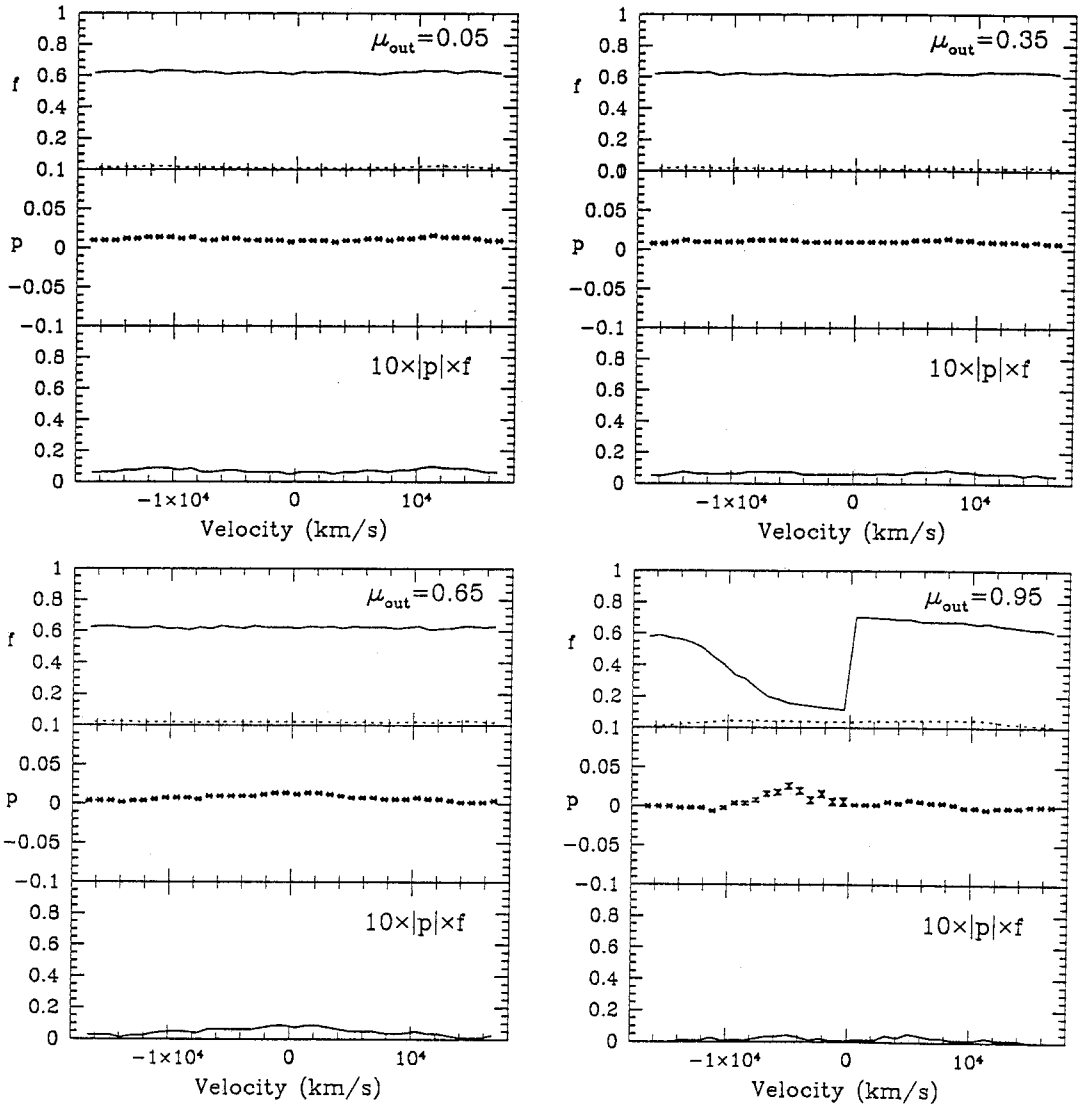
μ_{out}=0.05
μ_{out}=0.35
μ_{out}=0.65
μ_{out}=0.95
f
p
10×|p|×f
−1×10⁴
0
10⁴
Velocity (km/s)

Figure 9d

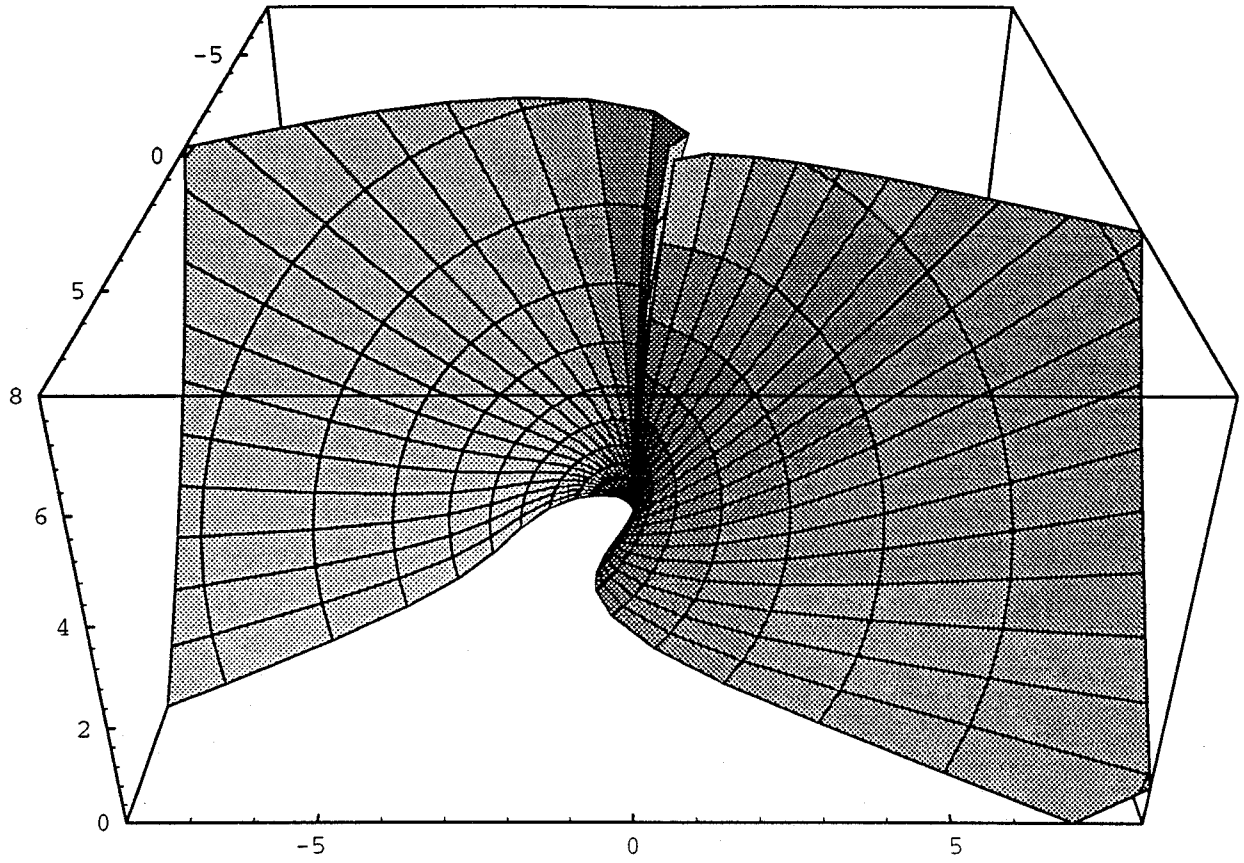

Figure 10

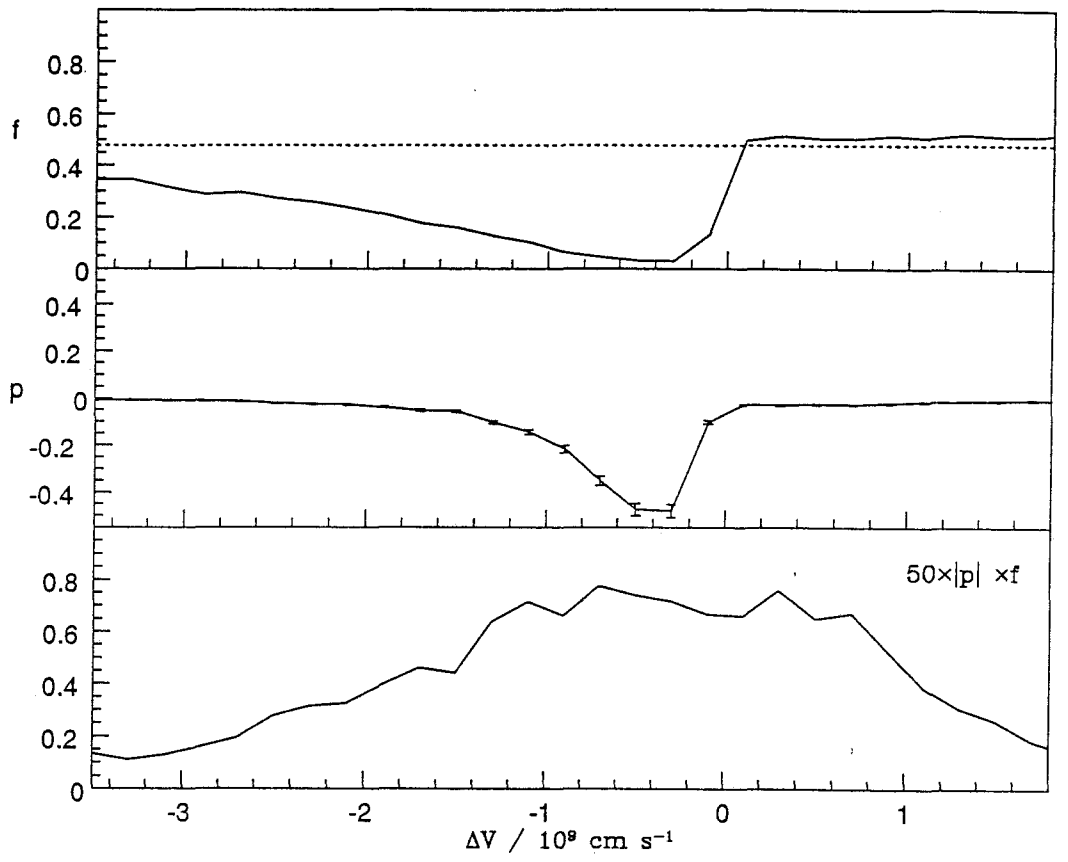

Figure 11a

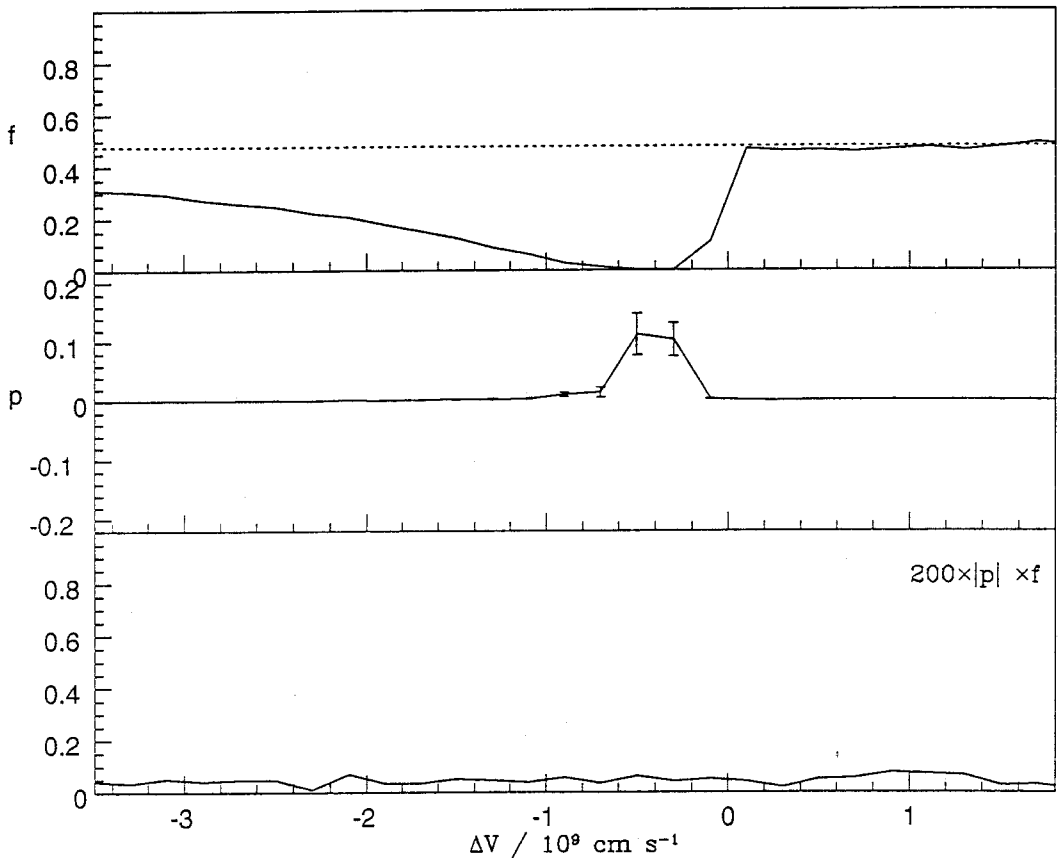

Figure 11b

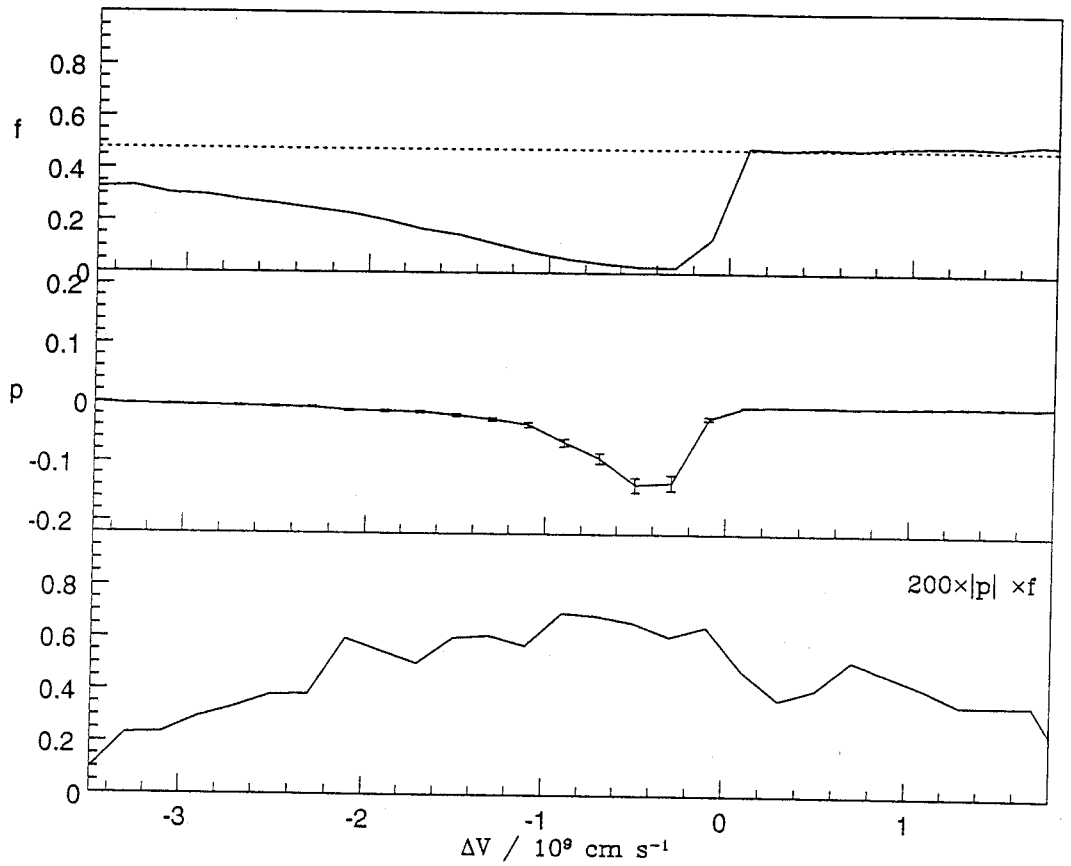

Figure 11c

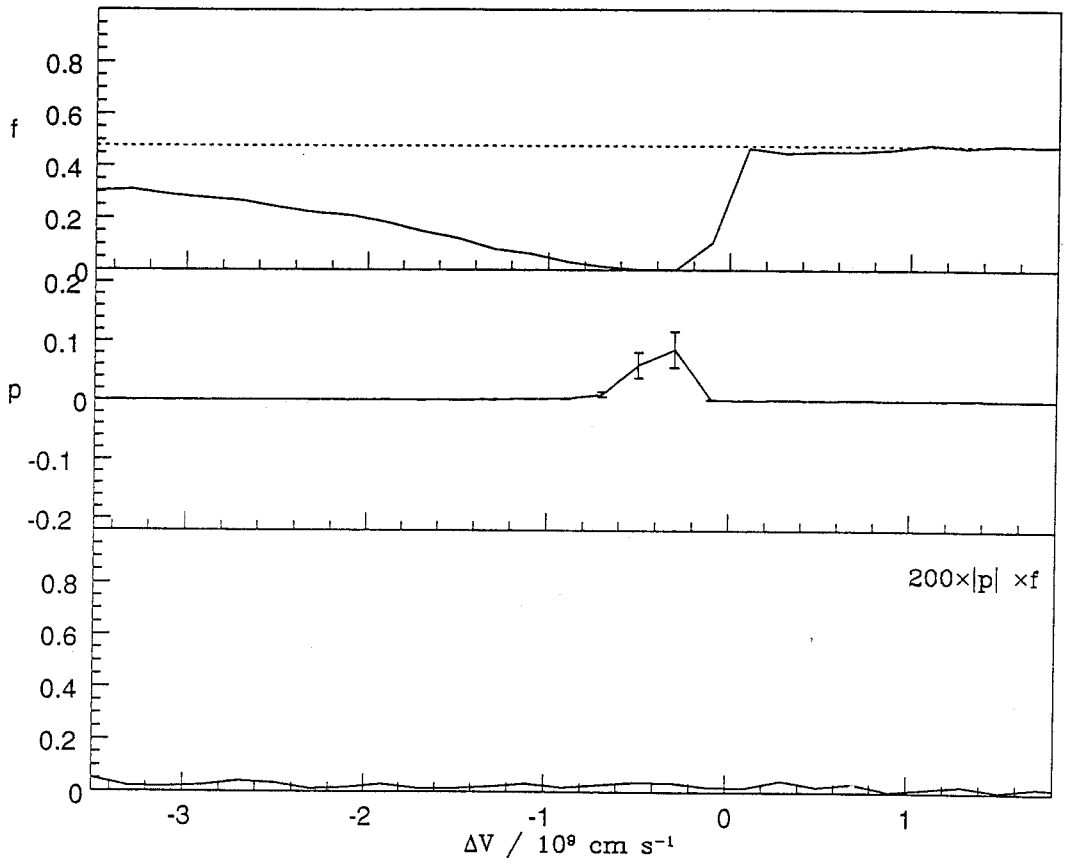

Figure 11d

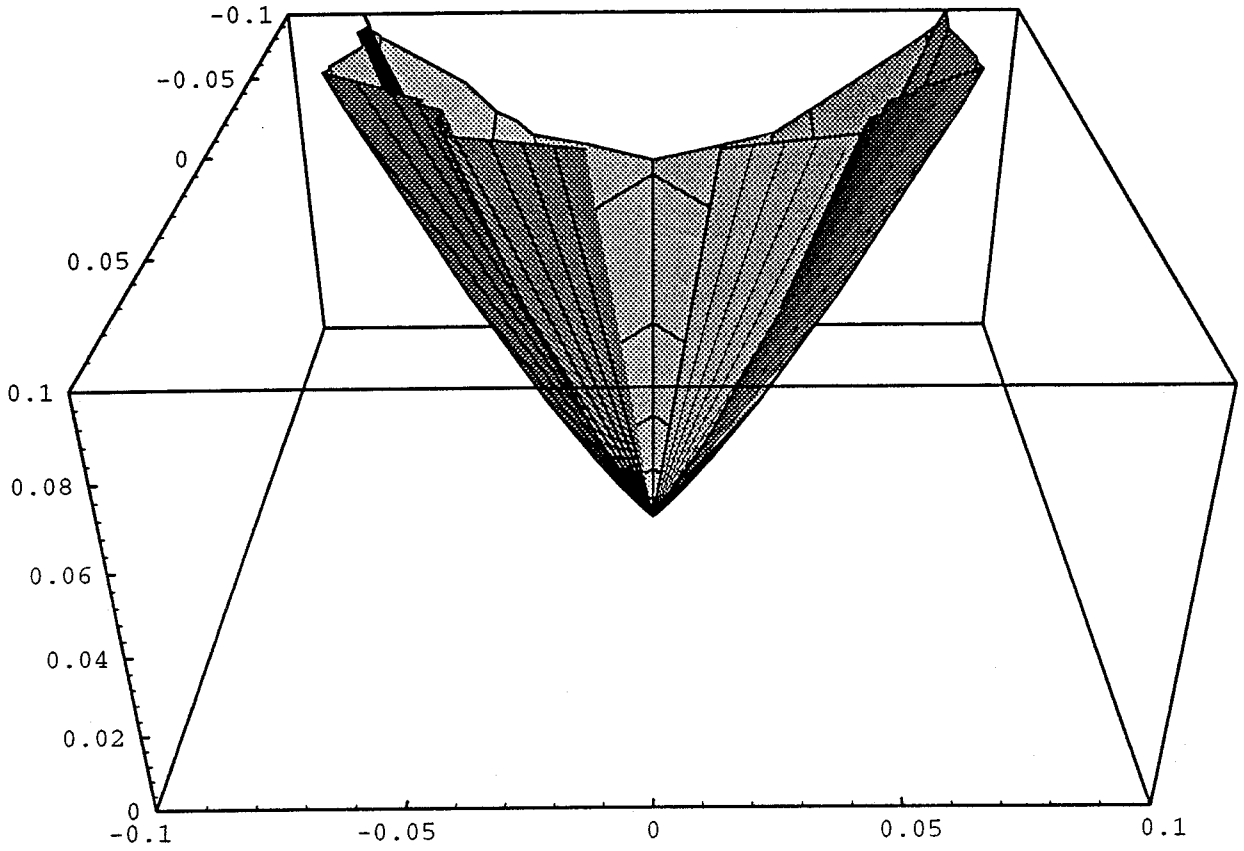

Figure 12

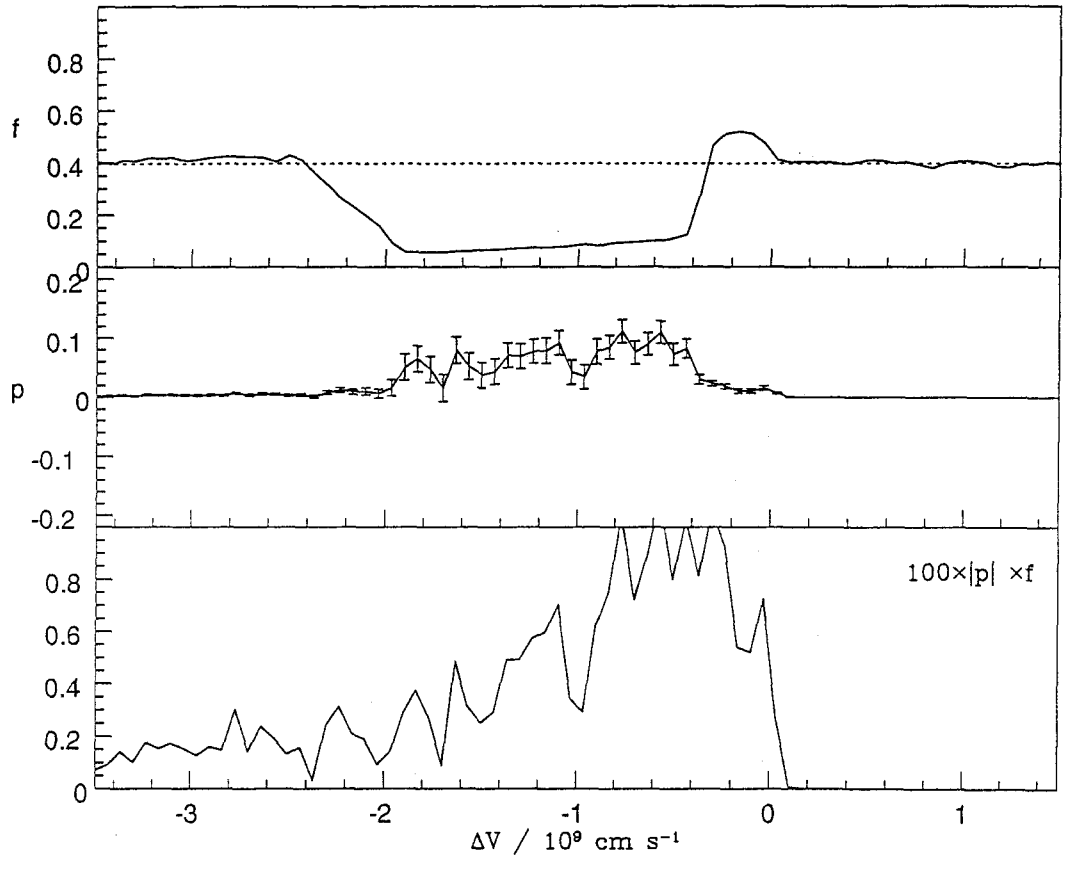

Figure 13a

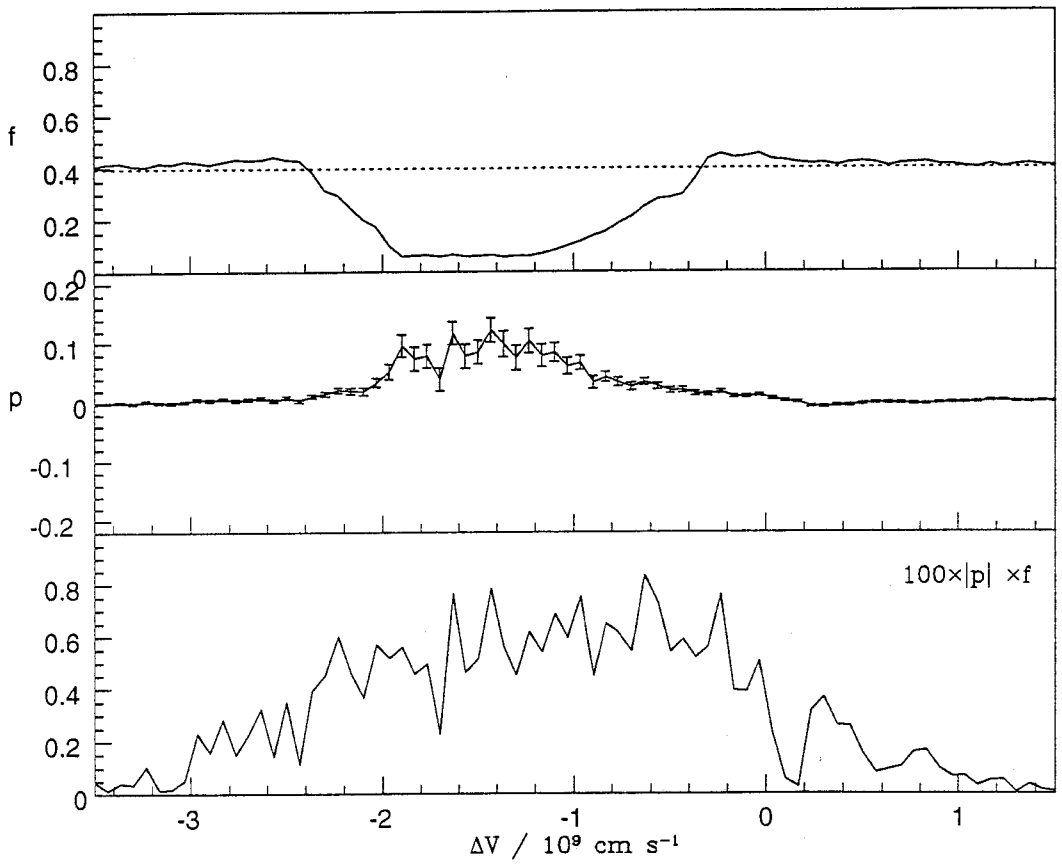

Figure 13b

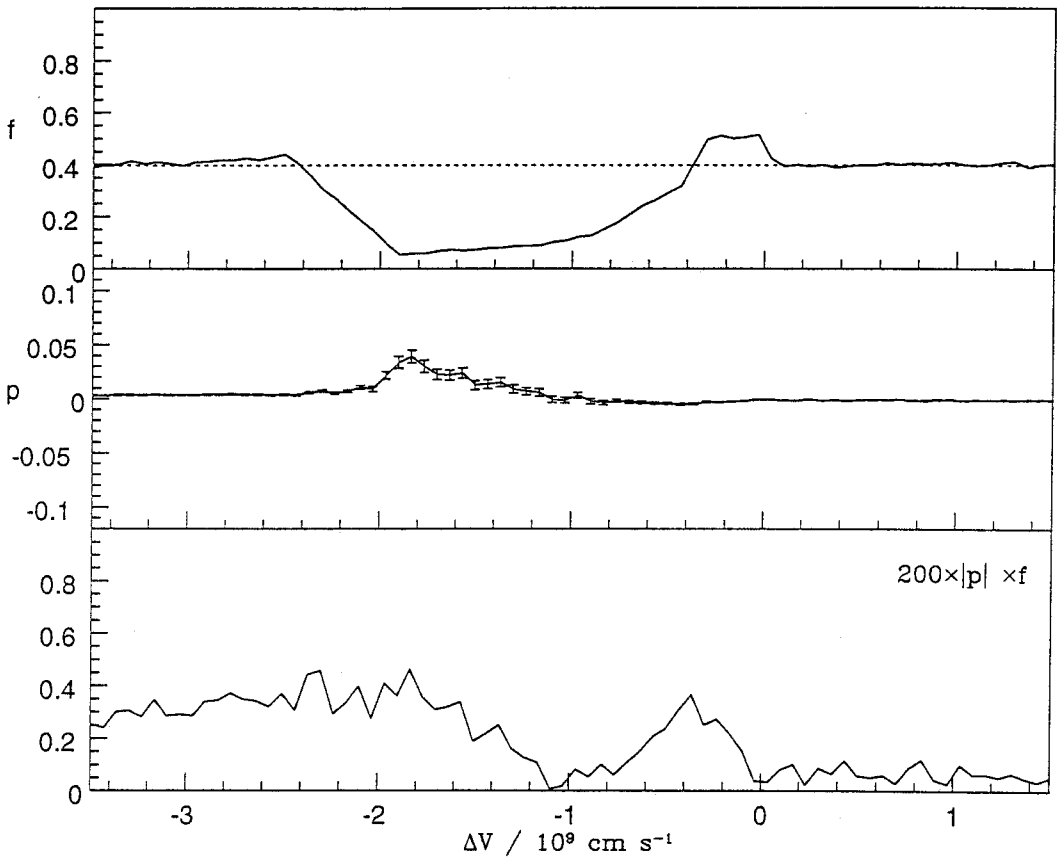
f
0.8
0.6
0.4
0.2
0
p
0.1
0.05
0
-0.05
-0.1
200×|p| ×f
0.8
0.6
0.4
0.2
0
-3
-2
-1
0
1
ΔV / 10⁹ cm s⁻¹

Figure 13c

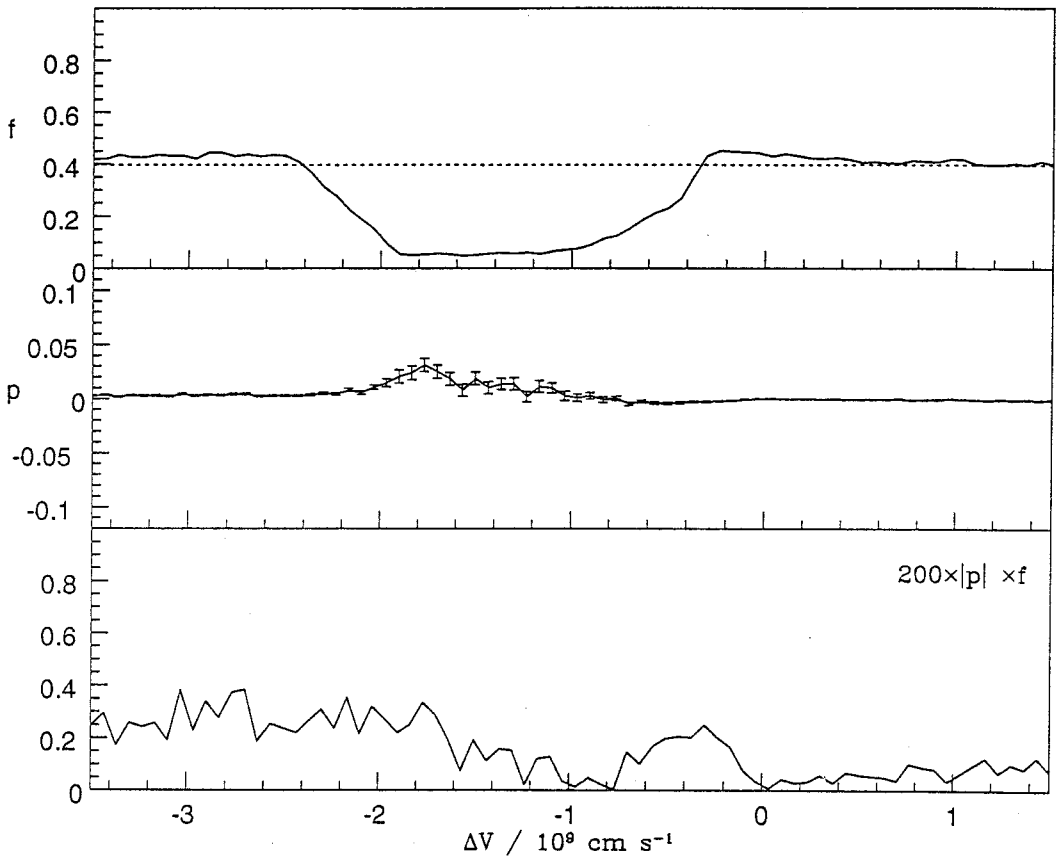
f
0.8
0.6
0.4
0.2
0
p
0.1
0.05
0
-0.05
-0.1
200×|p| ×f
0.8
0.6
0.4
0.2
0
-3
-2
-1
0
1
ΔV / 10⁹ cm s⁻¹

Figure 13d

5

On the Ultraviolet Polarization of Radio-Quiet Quasars

R. D. Blandford & H.-W. Lee

Caltech

Abstract

A summary is given of the conditions necessary to create measurable polarization by resonance scattering of photoionized gas outflowing from quasars. The aspects that are dictated by basic atomic physics are emphasized so that they may provide a clear signature for its identification. Singlet transitions associated with ions isoelectronic with the alkaline earths are most likely to exhibit strong polarization which may be spread over $\sim \pm 30,000$ km s^{-1} relative to the fiducial wavelengths. Recent reports of variable polarization of the troughs of broad absorption line quasars and strong continuum polarization shortward of ~ 800 Åin a few radio-quiet quasars are interepreted in terms of resonance scattering. Resonance scattering may provide a useful probe of quasar gas dynamics.

1. Introduction

It is widely believed that broad absorption line quasars, (henceforth BALQ), comprise a fraction $q \sim 10 - 15$ percent of normal radio-quiet quasars (henceforth RQQ) observed through an anisotropic wind (*e. g.* Weymann *et al.* 1991) that covers a proportion q of the sky seen from the continuum source. The outflowing gas is supposed to be accelerated roughly radially to speeds of up to $\sim 30,000$ km s^{-1} exterior to both the central UV continuum source and the broad emission line region so as to produce broad, blue-shifted absorption troughs, associated with

common resonance line transitions in BALQ. The precise location and physical conditions within the absorbing gas remains a matter of controversy (*e. g.* Arav & Begelman 1994, Scoville & Norman 1995, Murray *et al.* 1995).

Three recent developments promise to clarify the situation. Firstly, observations of high redshift RQQ using HST and ROSAT have revealed much of the underlying far UV-soft X-ray spectrum thereby defining directly the photoionizing radiation field and identifying the prominent lines (*e. g.* Korista *et al.* 1992, Wills *et al.* 1993, 1995). Secondly, detailed spectropolarimetry of BALQ using the Keck telescope (Cohen *et al.* 1995), has exhibited a uniformly polarized continuum, attributed to electron scattering, augmented by generally unpolarized emission lines and more highly and variably polarized absorption troughs. Thirdly, a few RQQ have been observed polarimetrically shortward of the Lyman edge using the HST/FOS spectropolarimeter and the polarization exhibits a dramatic rise with decreasing wavelength in the far UV $\lesssim$ 800 Å(Impey *et al.* 1995, Koratkar *et al.* 1995).

In this letter, we provide an analysis of resonance line polarization that we hope will be useful for interpreting spectropolarimetric observations of quasars. We suppose that radiation that is scattered out of the beam is polarized by the scattering and can be observed along other lines of sight. When the quasar is observed through the absorbing gas, this may contribute to the trough polarization observed in BALQ. When the observer's line of sight is unobscured, resonance line scattering may contribute to continuum polarization in RQQ.

2. Polarization of Resonance Scattering

Most of the prominent "absorption" line troughs observed in BALQ spectra are associated with resonance line transitions of common ions, in which photons are scattered out of the line of sight, not absorbed because the gas densities are low for collisional de-excitation (Lee, Blandford & Western 1994, henceforth LBW, Lee & Blandford 1995, henceforth LB). The state of the emitted photon therefore depends upon the state of the incident photon and anisotropy in the radiation field can

produce significant polarization in the scattered radiation. Five factors, the nature of the transition, the effect of multiple scattering, the velocity gradient tensor, the abundance of the ions, and the geometrical arrangement of the scattering sites combine to determine the observed degree of polarization in a line. We consider them in turn.

2.1 Multiplet Transitions

The simplest transitions are singlets ($^1S_0 - ^2P_1^o$) involving permitted ground state transitions of ions like C^{++}, N^{+++}, O^{4+}, and Si^{++} that are isoelectronic with alkaline earth metals, there are two s electrons in a state with $J = 0$, one of which can be promoted to a p state so that $J = 1$ (*e. g.* Condon & Shortley 1951). (We confine our attention to Russell-Sanders coupling of low Z ions.) The degree of polarization following a single scattering is given by

$$p(\theta) = \frac{p_\perp \sin^2\theta}{1 + p_\perp \cos^2\theta} \tag{1}$$

where $p_\perp = 1$ for a singlet transition (LBW). This is identical to the polarization from Thomson scattering.

The next simplest type of transition is a simple doublet ($^2S_{1/2} - ^2P^o_{1/2,3/2}$) found in ground state transitions involving alkali metal-like ions such as C^{+++}, N^{4+}, O^{5+} and Ne^{7+}. A single valence electron is excited from a s shell to one of two states in the p shell. The velocity difference between the two components of a doublet is $\sim 500 - 3000$ km s^{-1}, greatly in excess of the thermal velocity dispersion of the ions but much less than the velocity spread in the flow. The $J = 1/2$ state has two degenerate sublevels and the $J = 3/2$ state four sublevels. The cross section for excitation to the higher energy excited $J = 3/2$ state is therefore twice that for excitation to the $J = 1/2$ level. Now, when a continuum photon with frequency in excess of both components of a doublet transition propagates outward through a radially accelerating and expanding wind, it will first have the opportunity of exciting ions into the upper $J = 3/2$ excited state. Subsequent de-excitation into the ground state produces a polarization with distribution given by

Eq. (1) and $p_\perp = 3/7$. Subsequent scatterings involving the same transition can then occur. When a photon escapes from this resonance it will propagate some distance and then come into resonance with the second component of the doublet. However, now $p_\perp = 0$ and all scatterings in the $J = 1/2 \rightarrow 1/2$ transition are completely depolarizing.

Two special cases of doublet scattering are the $L\alpha$ transitions of H and He^+. Here the doublet separation is $\lesssim 1$ km s^{-1}, less than the thermal width and the two components scatter simultaneously. In this case, $p_\perp = 3/11$ for single scattering.

For ions isoelectronic with B (or F), like C^+, N^{++} and O^{+++}, the ground level is split into two, $(^2P^o_{1/2,3/2})$, which, although separated by more than the thermal width, can be simultaneously populated by de-excitation from excited states. When the excited state is $^2S_{1/2}$, both components of the resulting "inverted doublet" are completely depolarized. For excitations into $^2P_{1/2,3/2}$, a quadruplet is produced. Again, the ground levels will be mixed and scatterings into the higher energy excited state at the first resonance location will be followed by possible scattering through the lower excited state at a second location. For excitation into $^2D_{3/2,5/2}$, only a triplet is permitted. The next group involves ions isoelectronic with C (or O), where the ground state is triply split into transitions from $^3P^o_{0,1,2}$. For excitations into $^3S_1$ an "inverted triplet" is formed. For $^3P_{0,1,2}$ and $^3D_{1,2,3}$, two different types of hexaplet are formed (The $^3D_{1,2,3}$ transition we style "shifted"). However, the $J = 1, 2$ excited states are effectively degenerate and only four lines will be distinguished. Finally, there are ions isoelectronic with N like O^+, Ne^{++}, where the ground state is $^4S^o_{3/2}$ and there are three excited states $^4P_{1/2,3/2,5/2}$ which produce a "shifted triplet."

In order to compute the average polarization to be expected from a single scattering in a given multiplet in which the ground state $J \geq 1$, we must allow for the fact that the ground sublevels may not be statistically populated as the collision frequency will be less than the radiative excitation rate (LBW). This has the effect of increasing the net observed polarization over what would be observed under collisional mixing. We must therefore also consider the effect of

all common transitions involving the ground state if we wish to determine the sublevel distribution self-consistently and the relative importance of the different transitions will depend upon the spectral index of the incident radiation.

In summary, singlet transitions are the most strongly polarized. Doublets, whose polarization is $\sim 1/3$ that for singlets depolarizes rapidly for $\tau > 1$ (excepting $Ly\alpha$). Triplets are next and their polarization persists at large optical depth. Finally, hexaplets and quadruplets exhibit more modest polarization. Values of $p_\perp$ for the different multiplets are tabulated in Table 1.

2.2 Multiple Scattering

Multiple scatterings are generally depolarizing. However, as photons escape from a resonance by diffusion in velocity space, anisotropy in the radiation field is maintained and the emergent polarization decreases more slowly than when when there is spatial diffusion). However, if there are secondary, depolarising photons as happens with the doublets, (and to some extent with the hexaplets), then the polarization decreases rapidly with increasing optical depth. We have attempted to quantify the effect of multiple scattering by introducing a depolarization factor, $D(\tau) = \exp[-\tau/b]$ and estimating the constant b for the different types of transition by fittingto the Monte Carlo simulations. We find that $b \sim 2$ for singlet transitions, but that $b \sim 1$ for doublets which are completely depolarized by secondary $J = 1/2 \rightarrow 1/2$ scatterings.

Another important consequence of multiple scattering apparent in the Monte Carlo simulations is that back-scattered radiation is generally more highly polarized.

2.3 Optical Depth

If ultraviolet radiation of a given frequency from a central continuum source propagates radially outward through an expanding wind, photons will be scattered if they encounter sufficient ions whose Doppler-shifted ground state transition frequencies match the radiation frequency. After de-excitation, a photon may be subject to additional scattering until it emerges with a Doppler-shifted frequency

in the AGN frame appropriate to its final propagation direction. If scattering lines are sufficiently sparse then they may be considered in isolation. For a given Doppler shift Δ scattered radiation will be seen from the corresponding Sobolev surface where the flow velocity $\mathbf{V}(\mathbf{r})$ satisfies $\mathbf{V}(\mathbf{r}) \cdot \mathbf{n} = -c\Delta$, where $\mathbf{n}$ is a unit vector directed toward the observer.

The scattering rate depends upon the optical depth which, in turn, depends upon the velocity gradient. Here, we concentrate upon isotropically expanding flows illuminated by a beam of incident radiation. The optical depth is given by

$$\tau = n_i f \lambda \left(\frac{\pi e^2}{m_e c}\right) \left(\frac{dV}{ds}\right)^{-1}, \tag{2}$$

where n_i is the ionic abundance and f is the oscillator strength (LB). The optical depth varies inversely with the velocity gradient along the direction of photon propagation and in an expanding flow where the acceleration declines with radius, the effects of inverse square dilution in the density will be partially offset by the decline in the acceleration so that the optical depth will not diminish rapidly with increasing velocity (*e. g.* Arav & Begelman 1994).

The velocity gradient tensor is unlikely to be isotropic. If the expansion is mostly transverse, as is likely to be the case at large radius in a wind, it turns out that the observed degree of polarization is roughly doubled relative to isotropic expansion with the same radial optical depth. Conversely, when the expansion is mostly radial, the emergent polarization is reduced. We quantify the effects of velocity anisotropy by a factor A which typically lies in the range $[0.5, 2]$.

2.4 Ionization Balance

In order to determine which ions are likely to dominate the scattering at a particular wavelength, it is necessary to perform a photoionization calculation. We have used the CLOUDY code (kindly supplied by G. Ferland) to compute the relative fractions of common ions as a function of the ionization parameter, U, defined here as the ratio of the H-ionizing photon density to the total electron density. We have performed these calculations for a standard "Matthews-Ferland"

spectrum, although our results are relatively robust with respect to these assumptions, being most dependent upon the elemental abundance (which we take to be solar) and the ionization potentials. Overall, we characterize the line strength by the combination

$$S_i(U) = X_i \bar{f} \lambda \tag{3}$$

where X_i is the ionic abundance relative to HI+HII and $\bar{f}$ is the average oscillator strength for the multiplet under conditions of either collisional or radiative mixing. (This is also somewhat sensitive to the supposed spectrum. We suppose that the spectrum is not so hard that photoionization and recombination are competitive with excitation.) The wavelength λ is measured in Å. With this definition,

$$\tau \sim 3 S_i(U) \left(\frac{dN_{H20}}{dV_9} \right) \tag{4}$$

where N_{H20} is the hydrogen column density measured in cm^{-3} and V_9 is the velocity measured in 10000km s^{-1}.

It is not certain whether conditions of radiative equilibrium are satisfied. Using Eq. (2), the number of recombination per expansion time is given by

$$N_{rec} \sim 10^{10} \alpha_i X_i f^{-1} \lambda^{-1} \tau \tag{5}$$

where α_i is the radiative plus dielectronic recombination coefficient to state i in $\mathrm{cm}^3\mathrm{s}^{-1}$. For the common ions $\alpha_i \sim 0.4 - 5 \times 10^{-11}$, (Osterbrock 1989) and so for $X_i \sim 10^{-4}$, $f \sim 0.1$, $\lambda \sim 1000$, $\tau \sim 1$, $N_{rec} \sim 0.1 - 1$, it is possible that some ionic species might be created at smaller radii and not have had time to recombine.

2.5 Geometrical Dilution

So far, we have concentrated upon estimating the polarization that will emerge locally from a small region illuminated by a central continuum source. We now turn to the most model-dependent aspect of the problem and this is the dilution of the emergent polarization by averaging over all scattering sites and taking account of the fact that only a fraction $\sim q$ of the continuum photons are incident upon

them. The simplest case arises when the outflow is confined to a pair of narrow jets, only one of which is likely to be visible due to the obscuring effect of an intervening accretion disk. In this case (*e. g.* LB), the geometrical dilution factor, which we call G, will depend upon observer latitude, varying from $G \sim q$, the solid angle subtended by the jet, for a RQQ viewed equatorially to $G \sim 0$ for a BALQ viewed along the jet. In the former case, the high polarization will be limited to a narrow range of observed velocity. The polarization direction will be perpendicular to the projected symmetry axis, such as might be revealed by a weak radio source.

Conversely, and more popularly, if the outflow is equatorial, the net polarization will be parallel to the symmetry axis, but greatly reduced by the integration over azimuth. Here large blue- and redshifts are possible. Simple models outlined in LB lead to estimates $G \sim q/3$, when viewed equatorially to $G \sim 0$ when viewed along the symmetry axis.

The kinematics may be even more complicated. For example, the dominant lines may not be sparse relative to the typical outflow speeds, so that most continuum photons that are incident upon the absorbing gas are actually scattered and there is a competition between the different ions to provide the first scattering. This can have the effect of suppressing the continuum flux and thereby enhancing the observed degree of polarization. In addition, the velocity field may be significantly non-radial so that high polarization can be seen in combination with a large velocity shift (LB, Murray *et al.* 1995). (In the limiting case of circular motion, it is the approaching and receding gas that scatters in a perpendicular direction.) Finally, if the quasar continuum is beamed and the beamed radiation intercepts the scattering gas, then the polarization will be enhanced. Overall, though, ions that are prominent at a given ionization parameter U should be subject to similar geometrical dilution.

3. Interpretation of Polarization Observations

We define the degree of polarization p to be the quotient of the measured polarized flux and the total continuum flux interpolated by removing the emission

lines and the absorption troughs. Based on the foregoing considerations, this can be estimated by

$$p = p_{\perp} \tau D(\tau) A G. \tag{6}$$

In this equation, $p_{\perp}$ depends upon the atomic physics and τ given by Eq.(4) depends upon both the atomic physics and the ionization parameter U. A and G depend upon the overall dynamical conditions and the observer inclination but ought to be fairly constant in a given quasar.

Table 1 and Fig. 1 may be useful for interpreting the polarization to be expected from spectropolarimetric observations of RQQ and BALQ as they show, comparatively, which lines should be most highly polarized under a given set of ionization conditions and, if wavelength-dependent polarization is observed, may be used to infer the ionization parameter within the scattering region. (At a higher level of sophistication, it may be possible to infer the ionization parameter as a function of velocity along the line of sight which would be diagnostic of the physical conditions in the absorbing gas.) The constraints that they embody are quite strong, given a reasonable wavelength coverage. In particular, unless unusual abundances are posited, weakly polarizing transitions cannot be invoked in the absence of expected strongly polarized counterparts.

We illustrate this approach by interpreting observations presented in two recent observations. Firstly, in the $z = 1.47$ RQQ, PG 1630+377, the polarized spectral flux P_{λ}, is reported to rise roughly in proportion to λ^{-10} for $\lambda \lesssim$ 800Å(Koratkar et al 1995) and the maximum degree of polarization is measured as $p \sim 0.2$ at $\sim$ 700Å. Additional structure can be seen in the wavelength dependence with marginally significant lines, some of which can be associated with singlet transitions from Table 1; in particular $p \sim 0.07$ (as defined above) in the vicinity of $Ly\alpha$. It is possible to interpret the far ultraviolet rise in continuuum polarization as the superposition of several resonantly scattered lines. Prominent singlet transitions are located at $\lambda 630, 736, 765, 786$, and these should be the most highly polarizing. (Moderately polarizing O III,O IV lines are also found at $\lambda 789, 834$ and

these may also contribute to scattering.) In contrast to the absorption troughs, we expect that the scattered radiation will be both red- and blue-shifted, with perhaps a preference for redshift as backscattering is favored at large optical depth. In order to cover most of the continuum, outflow speeds of $\sim 30,000\text{km s}^{-1}$ must be invoked, comparable with largest trough widths seen in BALQ. However, the largest degree of polarization reported requires either a special geometry or strong suppression of the continuum perhaps through absorption along the line of sight. In favor of this second interpretation we note that the measured spectral index in PG 1630+377 is $\alpha \sim 4$ for $700 \gtrsim \lambda \lesssim 900$ much greater than the value $\alpha \sim 0.5 - 1$ associated with the reflected photoionizing spectra.

This interpretation makes two general predictions. Firstly, the observed ultraviolet polarization should not vary smoothly with wavelength but should be correlated with the location of the most prominent singlet lines. Secondly, although it is an accident of atomic physics that most of the prominent resonance lines in the more accessible region of the spectrum longward of ~ 1000Åare doublets and therefore not strongly polarizing at large optical depth, there are a few singlets, notably $AlIII1671$ and $SiIII1206$ and these may be more readily observable from the ground. It is an intriguing possibility that the polarization seen in PG 1630+377 around a rest wavelength of $\lambda 1230$, might be due to blueshifted $SiIII$ and neither $Ly\alpha 1216$ nor $NV1240$ as might at first have been supposed.

Turning to BALQ, Cohen *et al.* (1995) have observed PHL 5200 and find a variable polarization $p \sim 0.01 - 0.02$ in the trough of CIV, polarized along a similar direction to the continuum which exhibits $p \sim 0.05$ and is presumably caused by electron scattering. In this case, we suggest that we are located in the equatorial plane and are observing scattered photons from other lines of sight filling in our trough. The relatively small polarization measured is consistent with resonance scattering by a CIV doublet as long as the optical depth τ is not too large. What is surprising, though, is the failure to observe red-shifted resonance lines, in the red wing of the CIV emission line. It is obviously of interest to attempt to observe polarization in the troughs of other prominent resonance lines and to see if its

variation correlates with the ratios of the lines listed in Table 1 for the inferred conditions.

We have described some ways in which the emerging field of quasar spectropolarimetry can be used to untangle the puzzling kinematics of the absorbing gas in quasars. It is to be hoped that this information will then be useful for defining its spatial location and ultimately for deciding between competing models that describe its dynamical origin.

Acknowledgements

We thank Chris McKee and Lonny Western for early collaboration on this topic. More recent assistance has been generously provided by Ski Antonucci, Nahum Arav, Marshall Cohen, Bob Goodrich, Anuradha Koratkar, Ari Laor, Norm Murray, Patrick Ogle and Ray Weymann. Support under NSF grant AST 92-23370 is gratefully acknowledged.

References

Arav, N., Li, Z. Y., & Begelman, M. C. 1994. *Ap. J.*, **432**, 62.

Cohen, M. H. *et al.* 1995. *Ap. J. Lett.*, in press.

Condon,E.U., Shortley, G.H. 1951. The Theory of Atomic Physics.

Impey, C. D., Malkan, M. A., Webb, W., & Petry, C. E 1995. *Ap. J.*, **440**, 80.

Koratkar, A., Antonucci, R. R. J., Goodrich, R. W., Bushouse, H., & Kinney, A. 1995. *Ap. J.*, in press.

Korista, K. T. *et al.* 1992. *Ap. J.*, **401**, 529.

Lee, H.-W., Blandford, R.D. & Western L. 1994. *MNRAS*, **267**, 303. (LBW)

Lee, H.-W., & Blandford, R.D. 1995. In preparation (LB)

Murray, N., Grossman, S. A., & Chiang, J. 1995. *Ap. J.*, in press.

Osterbrock, D. E. 1989. Astrophysics of Gaseous Nebulae and Active Galactic Nuclei, University Science Books, Mill Valley.

Scoville, N.,& Norman, C. 1995. *Ap. J.*, in press.

Weymann, R. J., Morris, S. L., Foltz, C. B.,& Hewett, P. C. 1991. *Ap. J.*, **373**, 23.

Wills *et al.* 1993. *Ap. J.*, **410**, 534.

Wills *et al.* 1995. *Ap. J.*, in press.

Figure Captions

Figure 1 a – The relative line strengths of common ions from a photoionization calculation for ionization parameter $U = 10^{-3}$. The photoionization code 'CLOUDY' is used and the adopted input spectrum is a standard 'Mathews-Ferland' spectrum. The normalization is arbitrary in order to enhance the relative strengths among various ions.

Figure 1 b – The same quantities for ionization parameter $U = 10^{-1}$

Figure 1 c – The same quantities for ionization parameter $U = 10^{-1}$

Table 1

Ion	Wavelength (Å)	f[a]
Singlets $^1S_0$ - $^2P_{0,1}$, $p_\perp = 1.$ $b \sim 2$		
He I	584	0.28
C III	977	0.81
N IV	765	0.64
O V	660	0.53
Mg I	2852	1.81
Al III	1671	1.84
Si III	1206	1.70
P IV	951	1.60
S V	786	1.46
Cl VI	671	1.28
Ar VII	586	1.21
Doublets $^2S_{1/2}$ - $^2P^o_{1/2,\ 3/2}$, $p_\perp = 0.28$ $b \sim 1$		
H I	1216	0.420
C IV	1549	0.290
N V	1240	0.230
O VI	1034	0.200
Ne VIII	774	0.150
Mg II	2798	0.940
Al III	1857	0.875
Si IV	1396	0.800
S VI	937	0.640
Cl VI	805	0.630
Ar VIII	705	0.570
Inverted Doublets $^2P^o_{1/2,\ 3/2}$ - $^2S^o_{1/2}$, $p_\perp = 0.0$		
C II	1037	0.059
C II	858	0.046
N III	764	0.110

O IV	609	0.10
Si II	1308	0.09
S IV	553	0.094
Ca IV	661	0.37
Triplets $^2P^o_{1/2,\ 3/2}$ - $^2S^o_{3/2,\ 5/2}$, $p_\perp = 0.30 \quad b \sim 10$		
C II	1335	0.27
C II	687	0.26
N III	991	0.18
O IV	789	0.15
Ne VI	561	0.14
Quadruplets $^2P^o_{1/2,\ 3/2}$ - $^2P^o_{1/2,\ 3/2}$, $p_\perp = 0.01 \quad b \sim 10$		
C II	903	0.52
N III	686	0.45
O IV	554	0.38
Si II	1196	0.91
Inverted Triplet $^3P^o_{0,\ 1,\ 2}$ - $^3S^o_1$, $p_\perp = 0.01 \quad b \sim 1$		
N II	645	0.23
O III	508	0.19
S III	508	1.49
S III	724	0.352
Hexaplet $^3P^o_{0,\ 1,\ 2}$ - $^3P^o_{0,\ 1,\ 2}$, $p_\perp = 0.27 \quad b \sim 10$		
N II	916	0.22
O III	703	0.18
Shifted Hexaplet $^3P_{0,\ 1,\ 2}$ - $^3D^o_{1,\ 2,\ 3}$, $p_\perp = 0.01 \quad b \sim 10$		
N II	1085	0.17
O III	834	0.15
S III	1197	0.62
Shifted Triplet $^4S_{3/2}$ - $^4P^o_{1/2,\ 3/2,\ 5/2}$, $p_\perp = 0.25 \quad b \sim 2$		
O II	834	0.43
O II	539	0.43
S II	1256	0.028

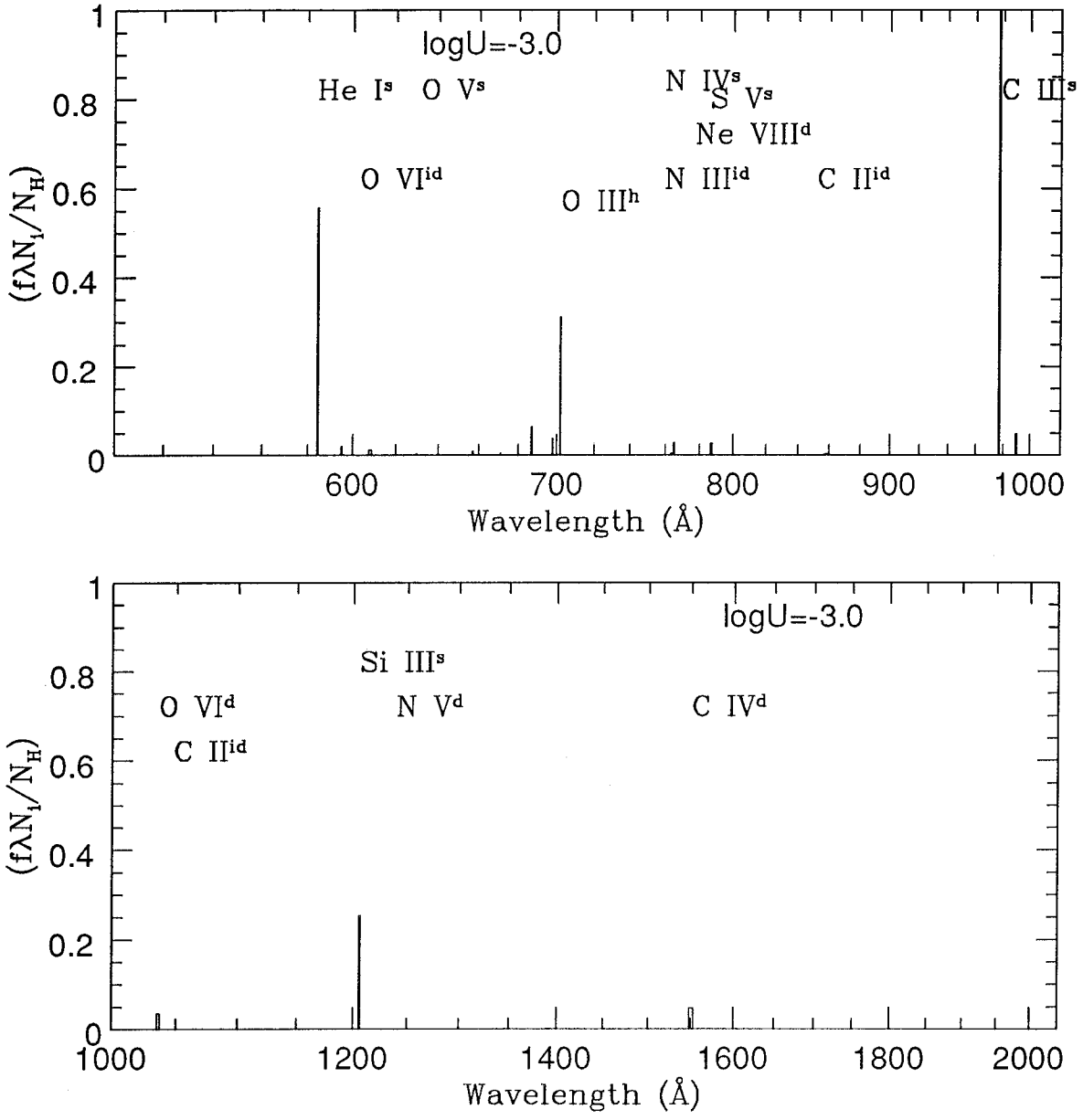
logU=-3.0
He I^s
O V^s
N IV^s
S V^s
C III^s
Ne VIII^d
O VI^id
N III^id
C II^id
O III^h
(fΛN_i/N_H)
Wavelength (Å)
logU=-3.0
Si III^s
O VI^d
N V^d
C IV^d
C II^id
(fΛN_i/N_H)
Wavelength (Å)

Figure 1a

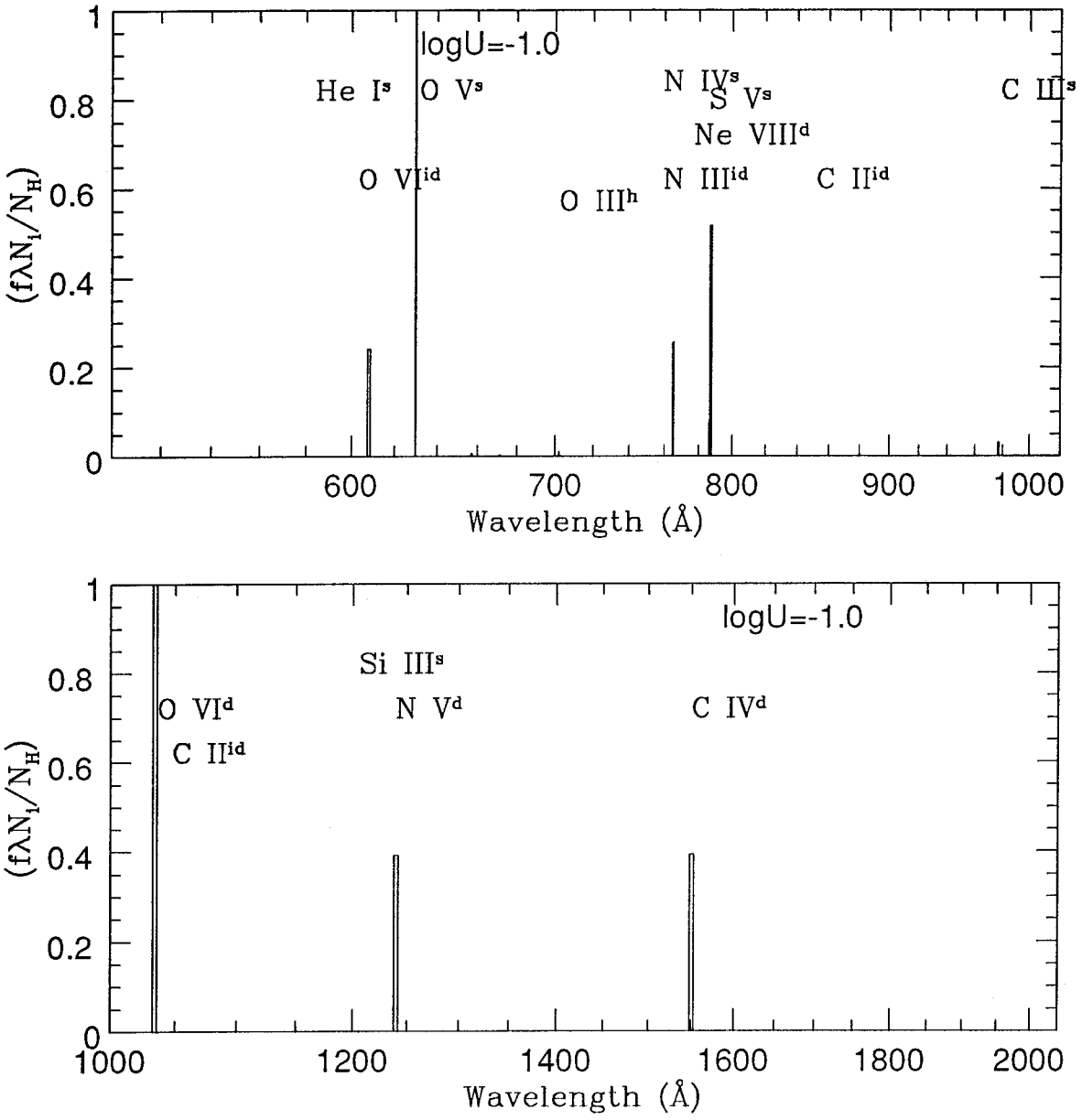
logU=-1.0
He I^s
O V^s
N IV^s
S V^s
C III^s
Ne VIII^d
O VI^id
N III^id
C II^id
O III^h
(fΔN_i/N_H)
Wavelength (Å)
logU=-1.0
Si III^s
O VI^d
C II^id
N V^d
C IV^d
(fΔN_i/N_H)
Wavelength (Å)

Figure 1b

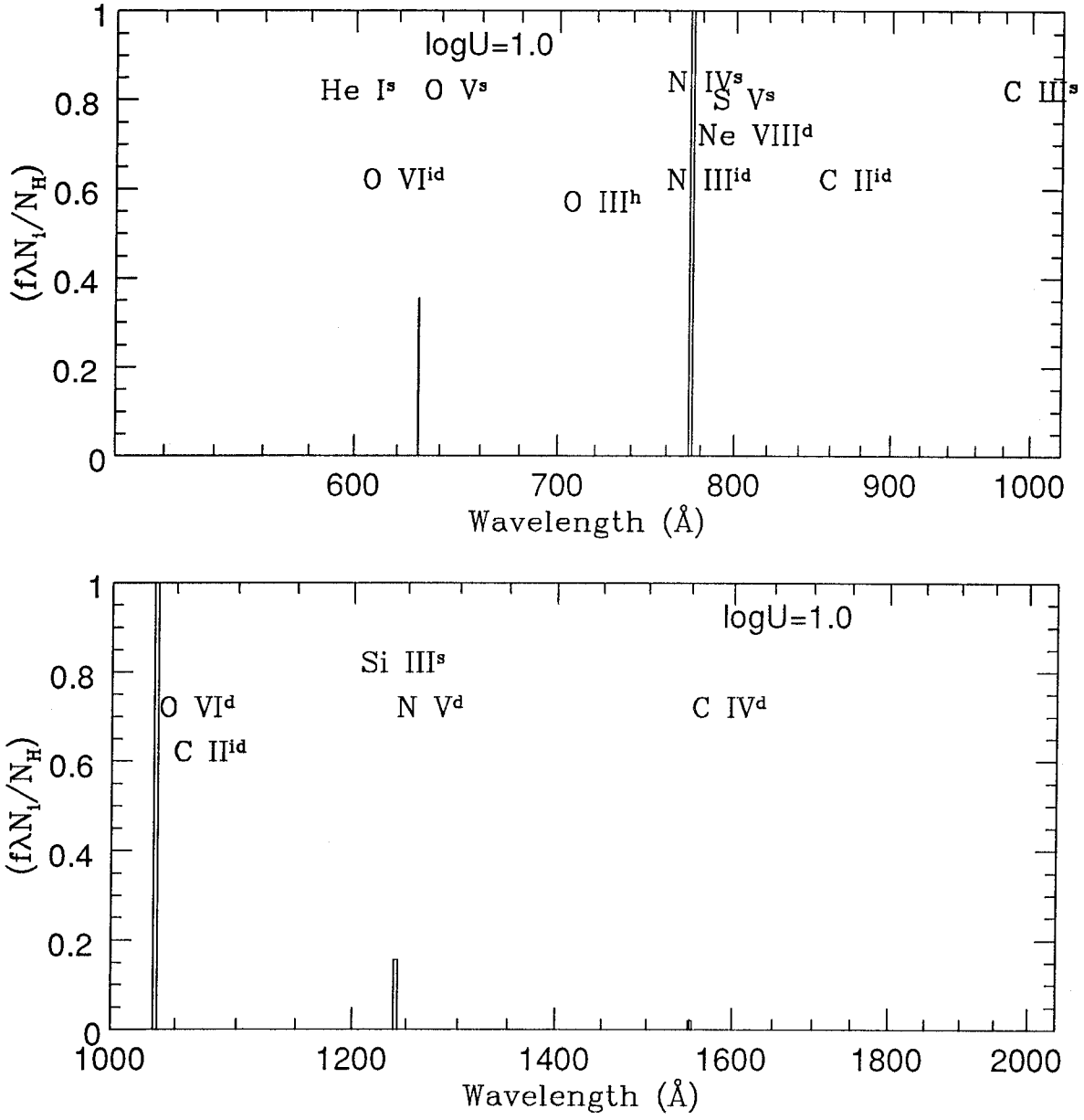
logU=1.0
He I^s
O V^s
N IV^s
S V^s
C III^s
Ne VIII^d
O VI^id
O III^h
N III^id
C II^id
(fλN_i/N_H)
Wavelength (Å)
logU=1.0
Si III^s
O VI^d
C II^id
N V^d
C IV^d
(fλN_i/N_H)
Wavelength (Å)

Figure 1c